

#### DEPARTMENT OF PHYSICS AND ASTRONOMY "A. RIGHI"

#### **SECOND CYCLE DEGREE**

#### **PHYSICS**

# Upgrade of the SND@LHC muon detectors with Drift Tubes

Supervisor Prof. Luigi Guiducci

Co-supervisor Giulia Paggi Defended by Licia Mozzina

Nunc age, res quoniam docui non posse creari de nilo neque item genitas ad nil revocari, ne qua forte tamen coeptes diffidere dictis, quod nequeunt oculis rerum primordia cerni, accipe praetera quae corpora tutte necessest confiteare esse in rebus nec posse videri.

Lucrezio, De Rerum Natura, Liber I

# Abstract

The Scattering and Neutrino Detector (SND@LHC) experiment at CERN can discriminate all neutrino flavors in a previously unexplored energy region. The signal events are interactions of neutrinos with energies between 100 GeV and 1 TeV, produced in the very forward direction from LHC pp collisions in the ATLAS interaction point.

Precise muon tracking in SND@LHC is important for a correct measurement of the muon flux, crucial for both the detector operation and the estimate of background in neutrino physics analysis, and for searches of rare events with muons in the final state, such as muon trident production or the dark Higgs dimuon decay. To improve muon identification, in March 2025 two Mini Drift Tubes (MiniDT) modules, miniature versions of CMS Drift Tubes, were added to the SND@LHC muon identification system to provide additional high resolution x-y position and direction measurements.

This thesis presents the integration of MiniDTs in the SND@LHC detector, DAQ and control systems, together with the developments of the offline software and results on their commissioning up to September 2025. The MiniDT installed reached a hit efficiency of approximately 97%, in agreement with the performance reported by CMS DT Detector Performance Group. In addition, the MiniDTs were also integrated into the SND@LHC offline software framework, sndsw, allowing common SND@LHC-MiniDT events to be built offline, while a preliminary tracking method based on the Hough Transform is under development to enable the standalone reconstruction of MiniDT tracks.

# Contents

Li	ist of Figures			$\mathbf{v}$	
In	Introduction				
1	The SND@LHC experiment				
	1.1	Physic	cs goals	4	
	1.2	The S	ND@LHC detector	4	
		1.2.1	The emulsion target	5	
		1.2.2	The electronic detector	7	
	1.3	Online	e system	9	
		1.3.1	Readout system	9	
		1.3.2	Readout electronics	12	
		1.3.3	Readout software	12	
		1.3.4	Detector Control System (DCS)	14	
		1.3.5	Data Quality Monitoring (DQM)	14	
		1.3.6	Experiment Control System (ECS)	14	
	1.4	Offline	e software: sndsw	15	
		1.4.1	sndsw structure	15	
	1.5	Event	reconstruction and background	17	
		1.5.1	Event reconstruction	17	
		1.5.2	Background sources	18	
	1.6	Motiv	ation for SND@LHC muon detectors upgrade	19	
2	The	Mini]	DT detectors	23	
	2.1	The D	Orift Tubes detectors in CMS	23	
	2.2	MiniD	OTs	27	
		2.2.1	Structure	27	

		2.2.2	Electronics	28
		2.2.3	Data	35
		2.2.4	MiniDT signal distribution	37
	2.3	MiniD	Ts repairs and tests	37
		2.3.1	Tests at INFN Legnaro Laboratory	38
		2.3.2	Tests at CERN	42
		2.3.3	MiniDTs-SND@LHC DAQ synchronisation tests	44
3	The	Mini]	DTs installation and integration in the SND@LHC experi-	ı
	men		•	49
	3.1	Install	lation preparation	49
		3.1.1	Mechanics design and production	49
		3.1.2	Experimental area (TI18 tunnel) preparation	50
		3.1.3	Gas system	53
		3.1.4	Electronics finalization	54
		3.1.5	Data storage	55
	3.2	Install	ation	55
		3.2.1	Mechanics assembly and placement	55
		3.2.2	Electronics	57
		3.2.3	Gas circuit	57
	3.3	Integra	ation in the SND@LHC DAQ system	63
		3.3.1	Integration in the SND@LHC ECS	63
		3.3.2	HV/LV control and Grafana online monitor	66
4	Min	niDTs (	commissioning and performance in SND@LHC	68
	4.1	Comm	nissioning with cosmic rays	68
		4.1.1	MiniDTs standalone runs	68
		4.1.2	MiniDTs-SND@LHC combined runs	72
		4.1.3	Preliminary tracking studies	76
	4.2	Comm	nissioning with LHC collisions	77
		4.2.1	First collisions and stable beams	78
		4.2.2	Gas issues	84
		4.2.3	MiniDTs efficiency	85
	4.3	MiniD	Ts offline integration in sndsw	93

	4.3.1	Classes for MiniDTs geometry and hits		93
	4.3.2	MiniDT-SND@LHC offline event matching		94
4.4	MiniD	$\Gamma$ s track reconstruction		94
	4.4.1	The Hough Transform for Drift Tubes detectors		96
	4.4.2	MiniDTs track reconstruction steps		98
Conclusions and future outlook		1	.02	
Aknowledgements		1	.04	
A MiniDTs LV and HV connections in TI18			1	.10
B Mir	niDTs n	oreliminary studies on tracking with cosmic rays	1	12

# List of Figures

1.1	SND@LHC detector (photo)	5
1.2	SND@LHC detector (scheme)	6
1.3	AND@LHC emulsion target wall	6
1.4	SND@LHC Veto system	8
1.5	SND@LHC US and DS structures	9
1.6	Online scheme	10
1.7	SND@LHC Front End board	12
1.8	SND@LHC DAQ board	12
1.9	Online event builder	13
1.10	SND@LHC ECS graphic user interface	16
1.11	SND@LHC computing model	17
1.12	SND@LHC neutrino event reconstruction	18
1.13	SND@LHC background energy spectrum	19
1.14	Residuals of tracks in simulation for SND@LHC muon detectors upgrade	20
1.15	Distribution of $\Delta R$ in simulation for SND@LHC muon detectors upgrade	21
1.16	Residuals of tracks in simulation for SND@LHC muon detectors upgrade	
	$(momentum)  \dots $	22
2.1	CMS Drift Tubes detector	24
2.2	CMS Drift Tubes cell (scheme)	25
2.3	$\label{eq:miniDTs} \mbox{MiniDTs endcaps (scheme)} \ . \ . \ . \ . \ . \ . \ . \ . \ . \ $	27
2.4	MiniDTs cathodes assembling	28
2.5	Tool for MiniDT anode wires tension	28
2.6	MiniDTs HV connectors (scheme)	29
2.7	MiniDTs LVFE board	30
2.8	MiniDTs LVFE board	31

2.9	CMS OBDT-Theta board (architecture)
2.10	CMS OBDT-Theta board (photo)
2.11	MiniDT Timebox
2.12	MiniDTs setup for tests at INFN-LNL
2.13	Timebox for MiniDT channel with dead FE or bad HV $\dots \dots 39$
2.14	Timebox for MiniDT channel with faulty FE or HV issues $\dots \dots 39$
2.15	Timebox for MiniDT channel with gas issues or disconnected strip $39$
2.16	Timebox for MiniDT inefficient channel
2.17	Timebox for MiniDT channel with disconnected cathode
2.18	$ {\it Timebox for MiniDT channel with disconnected cathode and gas issues} \ . \ \ 40 $
2.19	MiniDT without covers
2.20	MiniDT cathode pin with and without plastic cap
2.21	MiniDT cathode fixing
2.22	MiniDT gas tightness improvement
2.23	MiniDTs setup for tests at CERN
2.24	MinDT rate and efficiency during tests at CERN
2.25	Synchronisation test setup
2.26	Synchronisation tests results, runs 101153-101154
2.27	Synchronisation tests results, runs 101155-101156
3.1	Design layout of MiniDTs in SND@LHC
3.2	DS3-4 removal
3.3	LV patch panel for MiniDTs
3.4	HV power booster for MiniDTs
3.5	Gas bottle position
3.6	Electronics box
3.7	Material transport in LHC for the installation
3.8	Assembly of the mechanical support structure
3.9	MiniDTs placement in the mechanical structure
3.10	MiniDTs and DS3-4 in the mechanical support structure
3.11	SND@LHC with MiniDTs
3.12	Electronics box (installed and open)
3.13	Electronics box (installed and closed)
3.14	Gas bottle

3.15	MiniDTs gas link	61
3.16	Gas bubbler	62
3.17	Gas bottle flowmeter	62
3.18	MiniDT panel in SND@LHC ECS graphic user interface	63
3.19	MiniDT online monitoring during LHC beam adjust	65
3.20	MiniDT online monitoring during LHC stable beams	66
3.21	MiniDTs Grafana web monitor	67
4.1	Cosmic runs layers rate	69
4.2	Cosmic runs cells rate	70
4.3	Timeboxes with cosmic rays	71
4.4	Cosmic rays event display	72
4.5	Timing difference between MiniDT-SND@LHC shared events	73
4.6	Distribution of MiniDTs-SND@LHC shared events during a run $\ \ldots \ \ldots$	74
4.7	MiniDT wire values distribution in MiniDT events with at leasth one	
	H-TPG in both chambers	75
4.8	$\operatorname{MiniDT}$ wire values distribution in $\operatorname{MiniDT-SND@LHC}$ shared events	75
4.9	Coarse MiniDT-SND@LHC spatial matching	76
4.10	MiniDT preliminary tracking with cosmic rays	77
4.11	MiniDT hits as function of BX number in the first 2025 collisions $\ \ . \ \ . \ \ .$	78
4.12	MiniDT firmware register and TPGs rates monitoring	80
4.13	MiniDT hit rates	81
4.14	MiniDT cathodes currents	81
4.15	Instantaneous luminosity in ATLAS IP1	82
4.16	MiniDT hits and TPGs rates vs IP1 integrated luminosity	82
4.17	MiniDT hits cross section	83
4.18	MiniDT TPG rates with gas leak	85
4.19	$CO_2$ detector	86
4.20	MiniDT system during MiniDT Y substitution	86
4.21	Occupancy of DS tracks extrapolated to a MiniDT midplane	88
4.22	Timeboxes of MiniDT-SND@LHC event matching for efficiency measure-	
	ments	89
4.23	MiniDT layers efficiency trend	90
4 24	MiniDTs efficiency before Technical Stop	91

4.25	MiniDTs efficiency after Technical Stop	92
4.26	MiniDT-SND@LHC offline event matching with sndsw	95
4.27	Local frame of reference for MiniDT tracking with Hough Transform-based	
	method	97
4.28	Parameters definition of Hough Transform-based method	98
4.29	Macro-cell definition for the Hough Transform-based MiniDT tracking	99
4.30	Accumulation region of Hough Transform histogram	100
4.31	$\label{thm:minimum} \mbox{MiniDT reconstructed track with Hough Transform-based method} \ . \ . \ . \ .$	100
A.1	SND@LHC CAEN Mainframe	110
A.2	MiniDT HV power booster	111
A.3	MiniDT LV patch panel	111
B.1	Hits multiplicity in reconstructed tracks with MiniDT hits from cosmic rays	112
B.2	Distribution of track slopes in reconstructed tracks with MiniDT hits from	
	cosmic rays (3-hits)	113
В.3	Distribution of track slopes in reconstructed tracks with MiniDT hits from	
	cosmic rays (4-hits)	113
B.4	Distribution of track slopes in reconstructed tracks with MiniDT hits from	
	cosmic rays (all tracks)	113
B.5	Distribution of track horizontal intercepts in reconstructed tracks with	
	MiniDT hits from cosmic rays (3-hits)	114
B.6	Distribution of track horizontal intercepts in reconstructed tracks with	
	MiniDT hits from cosmic rays (4-hits)	114
B.7	Distribution of track horizontal intercepts in reconstructed tracks with	
	MiniDT hits from cosmic rays (all tracks)	115
B.8	Distribution of track Chi-Square in reconstructed tracks with MiniDT hits	
	from cosmic rays (3-hits)	115
B.9	Distribution of track Chi-Square in reconstructed tracks with MiniDT hits	
	from cosmic rays (4-hits)	116
B.10	Distribution of track Chi-Square in reconstructed tracks with MiniDT hits	
	from cosmic rays (all tracks)	116

# Introduction

This thesis describes the upgrade of the SND@LHC muon detectors with MiniDTs, small size replicas of CMS Drift Tubes (DT) chambers.

SND@LHC is a compact and standalone experiment, based on nuclear emulsions and electronic detectors, located at the Large Hadron Collider at CERN. The main goal of the experiment is the detection of neutrinos produced by proton-proton collisions at the Interaction Point 1 of LHC, located at a distance of 480 m. SND@LHC has been running successfully since 2022, achieving the first observation of neutrinos from a collider, and it will continue to take data until the LHC Long Shutdown 3, that will start in the second half of 2026. The main parts of the detector are a veto system, to reject ingoing charged particles; a target region, where walls of tungsten plates and nuclear emulsions are interleaved with a Scintillating Fiber tracker; and a hadron calorimeter and muon identification system.

Muon identification and tracking are essential for the selection of interesting events including a muon in the final state, such as muon neutrino charged current interactions, muon Deep Inelastic Scattering, and Beyond the Standard Model processes. In addition, the measurement of the total muon flux is needed for a correct background estimation and for calculating emulsion exposure time. The SND@LHC muon identification system was solely based on three x-y detection planes, built with 1 cm wide scintillator bars and interleaved with iron blocks. The relatively poor spatial resolution limits the capability to perform a tight matching between muon tracks and showers reconstructed in the detector target region, signature of a candidate neutrino interaction.

Preliminary simulations showed a significant improvement in high momentum muon tracking if several x and y points with sub-millimetric resolution are added at the end of the existing muon identification system. Due to their size ( $\sim 70 \times 80 \times 7 \text{ cm}^3$ ), spatial resolution ( $\sim 250 \,\mu\text{m}$ ) and 4-layers architecture, MiniDTs were considered well suited for a non-destructive upgrade, and the proposal of their installation during the Year End

Technical Stop 2024/25 was accepted by the collaboration.

The thesis is structured as follows. Chapter 1 provides an overview on the SND@LHC experiment, its physics goals and its structure before the MiniDTs installation, together with the preliminary simulations confirming the potential gain enabled by the installation of MiniDTs. Chapter 2 describes the MiniDT detectors, the repairs and tests that were performed in preparation of the installation, and the electronics system that was built to control, monitor and read out the chambers in the SND@LHC online environment. Chapter 3 shows all the stages of the MiniDTs installation and online integration in SND@LHC. Finally, Chapter 4 presents the commissioning of MiniDTs in SND@LHC, from March 2025 up to September 2025, with cosmic ray muons and first LHC beams, and the development of offline software for event building, efficiency measurements and tracking.

# 1 The SND@LHC experiment

Proton-proton (pp) collisions at LHC produce a high intensity beam of neutrinos, with energies up to a TeV, in the far forward direction. The Scattering and Neutrino Detector at LHC (SND@LHC) is a compact, standalone experiment located in the TI18 tunnel, 480 m downstream of the ATLAS Interaction Point (IP) to shield the detector from most of the charged particles produced in the LHC collisions. SND@LHC can identify all three flavors of neutrino interactions in the pseudorapidity region  $7.2 < \eta < 8.4$ . In this range, a large fraction of neutrinos originate from charmed-hadrons decays [1] - thus allowing to probe heavy flavour production physics at the LHC in the very forward region. SND@LHC is also sensitive to Feebly Interacting Particles (FIPs) through scattering off nuclei and electrons in the detector target. The SND@LHC detector consists of a hybrid system with a  $\sim 830$  kg target made of tungsten plates interleaved with nuclear emulsion and electronic trackers, followed by a hadronic calorimeter and a muon identification system.

The detector was installed in TI18 in 2021 during the Long Shutdown 2 and it has started to collect data since the beginning of the LHC Run 3 in April 2022. It will run throughout the whole Run 3.

SND@LHC has reported the observation of both  $\nu_{\mu}$  interactions [2], and neutrino interactions without muons in the final state [3].

The following paragraphs describe the SND@LHC detector before the MiniDTs installation and integration in the online system: Section 1.1 summarizes the Physics goals of the experiment; Section 1.2 explains the structure of SND@LHC and the role of its subdetectors; Section 1.3 gives a brief overview of the SND@LHC online system; Section 1.4 illustrates the SND@LHC official software framework, sndsw; Section 1.5 explains how neutrino interactions of different flavours are identified and lists the main sources of background for SND@LHC; finally, Section 1.6 explains the motivations for the SND@LHC muon detectors upgrade.

# 1.1 Physics goals

The main physics goals of the SND@LHC experiment are briefly described in the following:

- The neutrino-nucleon cross section is currently unexplored in the region between 350 GeV and 10 TeV [1] SND@LHC can cover the energy range between 100 GeV and 1 TeV detecting neutrinos from LHC pp collisions.
- Electron neutrinos can be used as a probe of the production of charmed hadrons [4], whose measurement can be translated into the corresponding open charm production measurement in fact, the rapidity window is the same, given the linear correlation between the parent charm quark and the hadron. The dominant partonic process for associated charm production at the LHC is the scattering of two gluons producing a  $c\bar{c}$  pair [5]. The average lowest momentum fraction of interacting gluons probed by SND@LHC is  $\sim 10^{-6}$ . The gluon parton distribution, at such low x values, is completely unknown, and its extraction could constrain and lower the uncertainty of QCD predictions. This would be particularly relevant for experiments at future hadron colliders.
- Tests on the lepton flavour universality can be performed, by measuring the ratio of  $\nu_e/\nu_\tau$  and  $\nu_e/\nu_\mu$  interactions, thanks to neutrino flavour identification.
- Direct search of Feebly-Interacting Particles (FIPs) such as dark scalars, Heavy Neutral Leptons (HNLs) and dark photons [6] can be carried out. It will be possible to disentangle the scattering of massive FIPs and neutrinos, with a significance that depends on the mass of the particle.

### 1.2 The SND@LHC detector

The SND@LHC apparatus structure consists of a target region preceded by a Veto system and followed downstream by a hadronic calorimeter and muon identification system. The experiment is visible in Figure 1.1, and a schematic view is depicted in Figure 1.2. The target region, with a mass of about 830 kg, is equipped with five walls of Emulsion Cloud Chambers (ECC), each followed by a Scintillating Fibre (SciFi) plane [1]. In the ECC technology, alternating emulsion films and tungsten planes act as tracking devices with

micrometric accuracy and as passive material, respectively, constituting the neutrino target. The SciFi planes provide the timestamp for the reconstructed events and have an appropriate time resolution for time-of-flight measurements. The emulsion target and the target tracker act together as an electromagnetic calorimeter, with a total of 85 radiation lengths  $X_0$  and 2.5 interaction lengths  $\lambda_{\rm int}$ . A 30% borated polyethylene and acrylic box contains Veto, emulsion target and target tracker, to shield from low energy neutrons and to mantain controlled temperature and humidity levels for the emulsion films. Placed downstream of the target, the hadronic calorimeter and muon identification system consist of eight 20 cm-thick iron slabs,  $\sim 9.5$  interaction lengths  $\lambda_{\rm int}$  in total, each followed by Upstream stations or Downstream stations planes of 1 cm-thick scintillating bars.



Figure 1.1: Global view of the SND@LHC detector in TI18, with the neutron shield box surrounding the target section [7].

# 1.2.1 The emulsion target

The emulsion target is made of five walls with a sensitive transverse size of  $384 \times 384$  mm<sup>2</sup> [1], consisting of four ECC bricks, as illustrated in Figure 1.3.

Each brick is made of 60 emulsion films with a transverse size of  $192 \times 192 \text{ mm}^2$ , interleaved with 59 tungsten plates, 1 mm-thick. Tungsten was selected as target material to maximise the interaction rate per unit volume. Moreover, its low intrinsic radioactivity

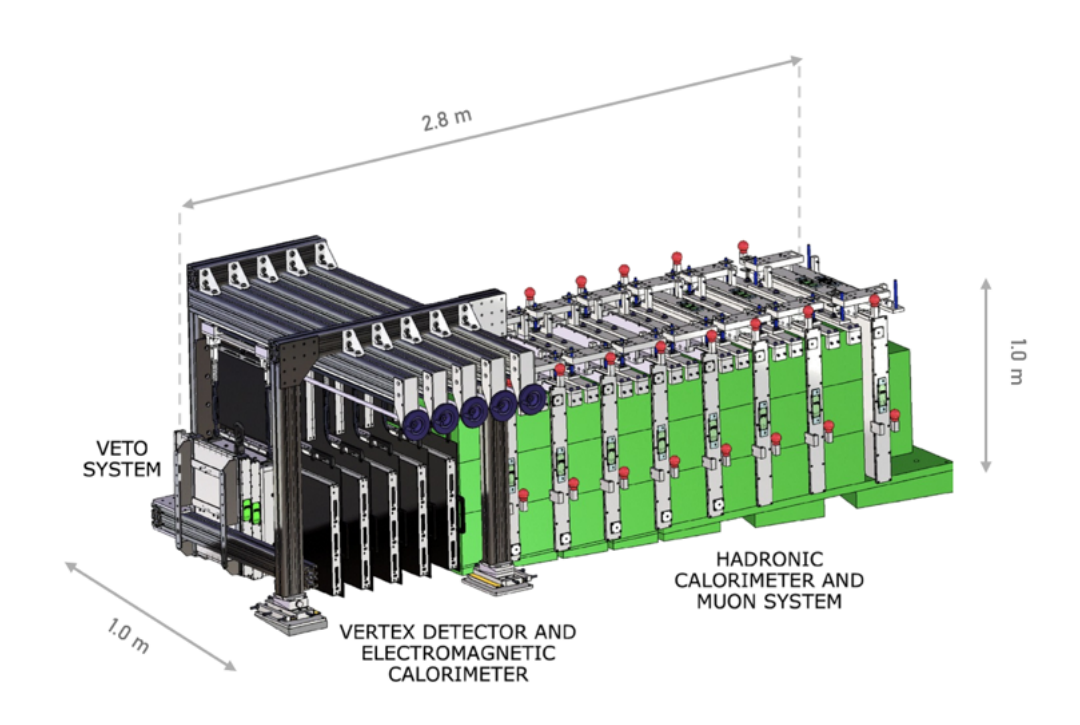
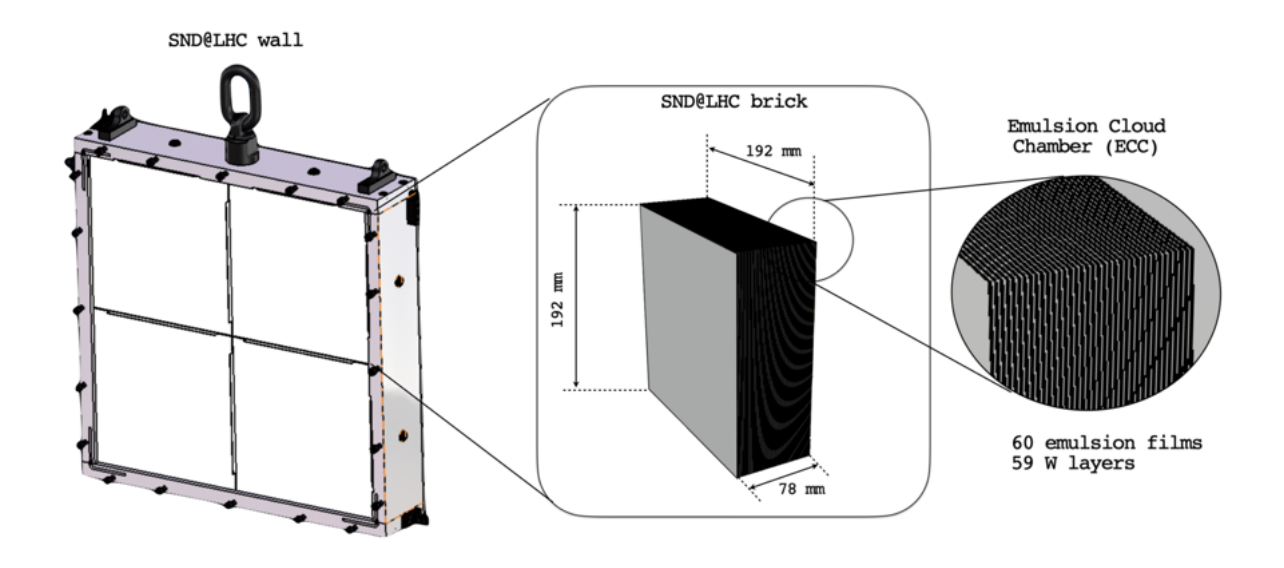


Figure 1.2: The SND@LHC detector structure, in a schematic view.



**Figure 1.3:** An emulsion wall is composed of four ECC bricks, each consisting of 60 emulsion films interleaved with 59 tungsten sheets [1].

makes it a suitable choice for an emulsion detector. The vertex reconstruction that results from track segments reconstruction has an accuracy at the micron level. A nuclear emulsion film has two 70  $\mu$ m-thick sensitive layers on both sides of a 170  $\mu$ m-thick

transparent plastic base. A charged particle passing through the emulsion film leaves trails of hits on both sensitive layers, providing two track segments. By connecting the two segments, the track slope measurement can reach milliradian accuracy. The emulsion target is replaced every  $\sim 20 \text{ fb}^{-1}$ , as to avoid an unmanageable combinatorial amount during the track reconstruction phase [8]. Then, dedicated and fully automated optical microscopes analyse emulsion films.

#### 1.2.2 The electronic detector

#### Veto system

The Veto system is the first part of the electronic detector. Its role is to reject all charged particles entering in the fiducial volume of SND@LHC. The Veto comprises 3 parallel planes of seven  $1 \times 6 \times 42$  cm<sup>3</sup> stacked scintillating bars: the first two planes are made of horizontal bars, which are singularly read out by 8 SiPMs on both ends, while the third plane is made of vertical bars, read out at the top edge by 56 Hamamatsu Photonics MPPC S14160-6050HS SiPMs ( $6 \times 6 \text{ mm}^2$ ,  $50 \mu \text{m}$  pitch) [1]. The scintillator bars are wrapped in aluminized Mylar foil, to ensure opacity and to isolate them from the light shining through adjacent bars. In 2022 and 2023, the number of Veto planes was two, and a third Veto plane was added in 2024 [9]. This upgrade is reported in Figure 1.4.

#### Target tracker and electromagnetic calorimeter

Following the Veto system, the next component of the electronic detector is SciFi. SciFi trackers assign a timestamp to neutrino interactions reconstructed in the ECC walls and provide an energy measurement of electromagnetic showers. Moreover, the combination of SciFi and scintillating bars of the US detector act as a non-homogeneous hadronic calorimeter jets energy measurement. Each SciFi station consists of two  $40 \times 40 \text{ cm}^2$  planes, alternating X and Y orientated mats. In each mat, six densely packed staggered layers of 250  $\mu$ m diameter polystyrene-based scintillating fibres are read out by SiPM arrays. The single particle spatial resolution in one view is  $\sim 150 \mu$ m, while the time resolution for a particle crossing both X and Y mats in one plane is  $\sim 250 \text{ ps}$  [2].

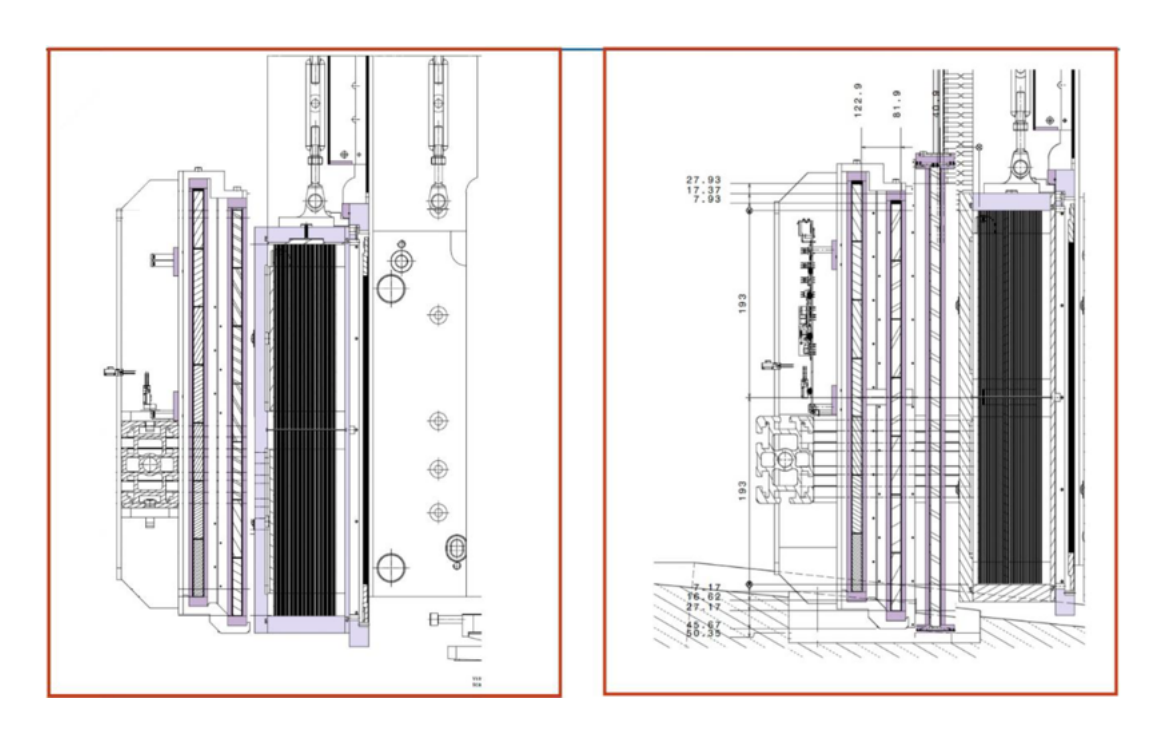


**Figure 1.4:** Old Veto system layout with two planes with horizontal bars (left). The upgraded Veto system with a third plane with vertical bars (right) [9].

#### Hadronic calorimeter and muon system

The last modules of the electronic detector are the muon system and hadronic calorimeter, structured in two parts: five UpStream (US) stations, followed by three DownStream (DS) stations. A schematic view of US and DS stations is visible in Figure 1.5. Each US station consists of 10 stacked horizontal scintillator bars of  $1 \times 6 \times 82.5$  cm<sup>3</sup>, similar to the ones in the Veto detector. This configuration results in a coarse Y view. At each US bar end, eight SiPMs are placed for readout, divided in six "large" (6  $\times$  6 mm<sup>2</sup>, 50  $\mu$ m pitch) SiPMs and two "small" (3  $\times$  3 mm<sup>2</sup>, 10  $\mu$ m pitch) ones [1]. On the other hand, a DS station consists of two layers of thinner bars - a plane of 60 horizontal bars (1  $\times$  $1 \times 82.5 \text{ cm}^3$ ) and one of 60 vertical bars  $(1 \times 1 \times 63.5 \text{ cm}^3)$  in alternating X and Y directions, that allow for a spatial resolution of less than 1 cm. The third station has an additional plane of vertical bars, which will be called DS4 in the following. Every horizontal DS bar end is viewed by one "large" SiPM, while the vertical ones are viewed only from one side. The time resolution for a single DS detector bar is  $\sim 120$  ps. The eight scintillator planes are interleaved with 20 cm thick iron blocks. Both US and DS bars are covered in aluminized Mylar foil to ensure opacity. The finer spatial resolution of the DS detector allows for the identification of muon tracks exiting the detector.

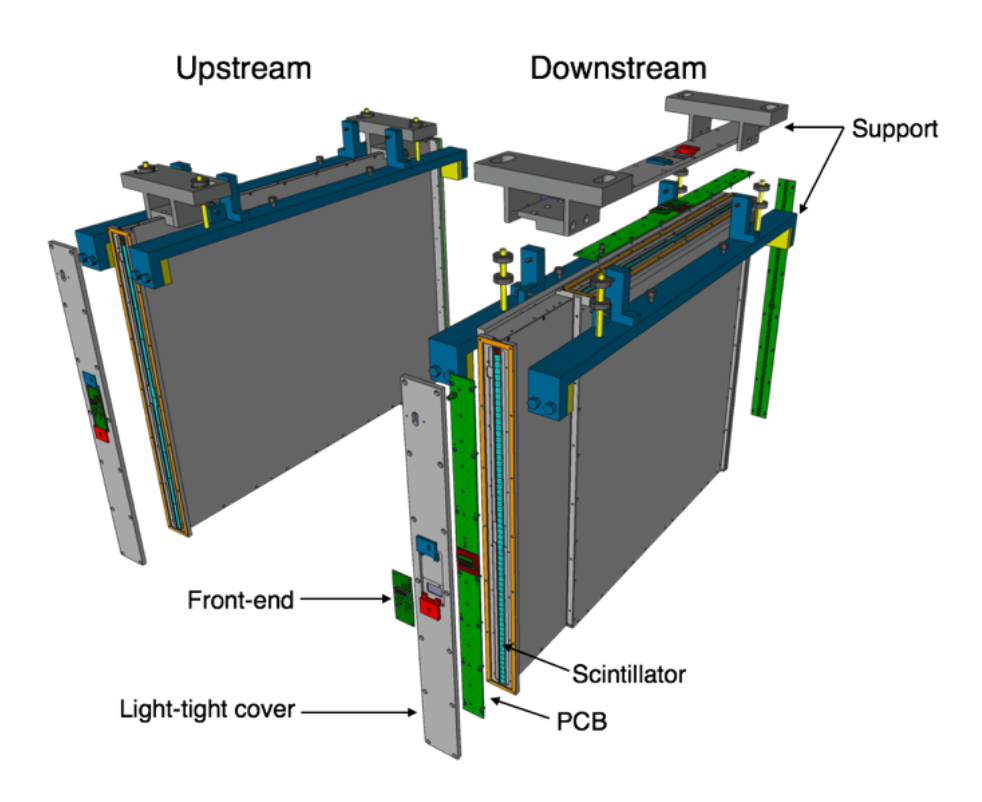


Figure 1.5: Illustration of an upstream and a downstream planes [1].

# 1.3 Online system

The SND@LHC online system includes all components involved in operating the experiment, *i.e.* the timing and the data acquisition hardware and software that realise the data flow from the detector to the storage, the Detector Control System (DCS) that controls and monitors the detector services, such as power supplies, cooling system, and the Data Quality Monitoring (DQM) and Real-Time Analysis (RTA) system, necessary to ensure a good quality of the collected data [1]. Globally, the top-level software, the Experiment Control System (ECS), encompasses all the sub-components above, together with the system of logs and databases in order to store information about the state, configuration and conditions of the data taking. The ECS is constructed to allow full automation of the data taking. The different components are shown in the scheme in Figure 1.6.

# 1.3.1 Readout system

As discussed in Section 1.2, the SND@LHC experiment features two types of electronic detector systems: scintillator bars read out by SiPMs in the Veto, the hadronic calorimeter and muon system, and scintillating fibres read out by SiPMs in the Target Tracker [1].

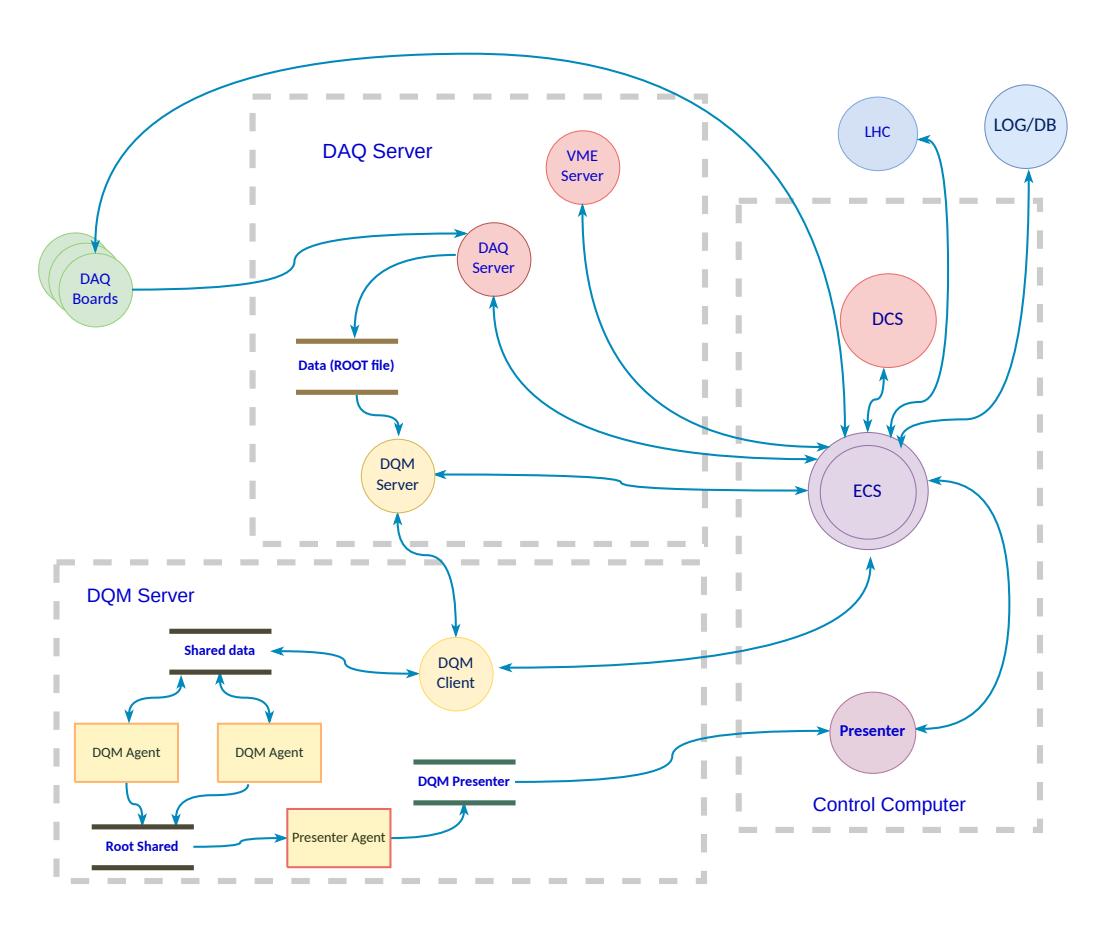


Figure 1.6: Simplified scheme of the SND@LHC online system [1].

These sub-systems are read out with the same data acquisition (DAQ) electronics, consisting of Front End (FE) boards, and DAQ readout boards, described in Section 1.3.2. They read out the signals from the SiPMs, digitize them and send the recorded data (timestamp and integrated signal charge) to a DAQ server.

Each DAQ board is connected to four FE boards. Noise reduction is performed at the FE level by setting an appropriate threshold for each channel, and in the DAQ server after the event building procedure of Section 1.3.3. The system runs synchronously with the LHC bunch crossing clock, and operates in a trigger-less fashion, *i.e.* all hits recorded by each board are transmitted to the DAQ server. A Trigger Timing Control (TTC) crate [10] is responsible for receiving the LHC clock and the orbit signals from the LHC Beam Synchronous Timing (BST) system and distribute them to the DAQ boards. A custom, synchronous B-Go command is broadcast by the TTC at the start of the run, and it is interpreted by the DAQ boards as a reset of the internal timestamping counters. It is important to note that due to the longitudinal structure of the LHC beams, shaped by the radio frequency (RF) cavities and nominally composed of  $\sim 3564$  circulating bunches with a bunch separation of 25 ns, the LHC orbit frequency is the single bunch revolution frequency, equal to 11 kHz.

The detector is powered using CAEN A2519 modules for the DAQ readout boards power, requiring 12 V and 2 A each, and A1539B modules for the bias voltage of the SiPMs, requiring up to 60 V and up to 300 μA per channel. These modules are hosted in two SY5527 mainframes.

The control of power supplies is performed by the detector control system (DCS, in the control computer in Figure 1.6) discussed in Section 1.3.4, which also monitors the voltages and currents drawn on both the LV and HV channels and monitors the presence of alarms.

The online system (DAQ Server, DQM server and Control computer shown in Figure 1.6) includes two servers located on the surface. One of them receives data from the DAQ readout boards, combines the data into events, and performs the online processing of the detector data, as described in Section 1.3.3, before saving the data to disk. The other one runs the ECS and the other elements of the online system.

#### 1.3.2 Readout electronics

The FE boards, visible in Figure 1.7, are based on the TOFPET2 ASIC by PETsys. The TOFPET2 is a 64-channels readout and digitization ASIC which incorporates signal amplification circuitry, discriminators, charge integrators, charge-to-digital converters (QDC) and Time-to-Digital Converters (TDC). A combination of up to three discriminators with configurable thresholds can be used.

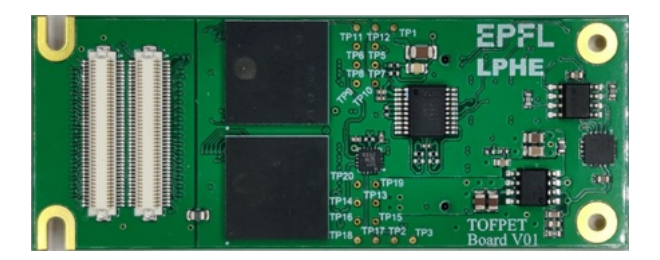


**Figure 1.7:** The SND@LHC FE board. The two TOFPET2 ASICS (centre) and the SiPM connectors (left) are visible [1].

The DAQ readout boards, in Figure 1.8, feature an Altera Cyclone V FPGA. Each DAQ board is equipped with four high-speed connectors for the FE boards, an optical fibre receiver to receive the clock and synchronous signals from the TTC system and a 1 Gb Ethernet port used for data and command transmission.



**Figure 1.8:** The SND@LHC DAQ board. The four FE board connectors are visible on the left, the TTCrx and optical receiver on the bottom-right [1].

#### 1.3.3 Readout software

Each DAQ board transmits all the recorded hits to the DAQ computer server, where event building is performed. The hits are grouped into events based on their timestamp,

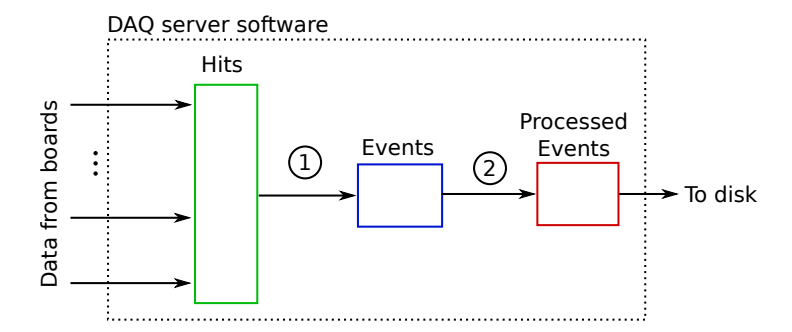


Figure 1.9: Schematic view of the event builder process. The colored rectangles represent queues of data being processed and the numbers identify the steps of event building, discussed in the text [1].

and saved to disk as a ROOT file [1]. The DAQ boards also transmit periodic triggers received from the TTC system. These heartbeat triggers are used by the event building software in the DAQ server to verify that all the boards are running synchronously, and operating properly even when there is no data. The readout process from starting servers to starting the data taking, sending periodic triggers, monitoring the status of each element, etc, is fully controlled by the ECS, described in Section 1.3.6. The event building process is structured in two main steps, shown in Figure 1.9. In the first step, hits collected by all boards and belonging to the same event, i.e. with time stamps within 25 ns, are grouped into "events". The event timestamp corresponds to the timestamp of the earliest hit within the event. The events are then filtered and processed online, before being written to disk. The details of the processing depend on the chosen settings, but it always contains an online noise filter, performed in two steps. In the first one, events are required to have a minimum number of DAQ boards that have detected a certain number of hits. This is fast and eliminates all the events generated by single noise hits. In the second step, the hits are grouped by the plane that generated them. This allows more advanced requirements on the topology of the events to be imposed. The system includes a number of additional configurable data processors, such as the FE calibration that may be applied during the data acquisition. The DAQ server writes the recorded data to a local disk. At the end of each run the data is transferred to a permanent storage and converted to the format used by the reconstruction software.

# 1.3.4 Detector Control System (DCS)

The Detector Control System (DCS) controls and monitors the status of all the detector services, *i.e.* the detector and electronics power supplies, the cooling system and the environmental sensors within the neutron-shielded box surrounding the target system, as well as the safety system. The voltage, currents and channel status of the power supplies are continuously monitored and transmitted to the ECS. The ECS then acts accordingly, logging the events or raising an alarm in case of problems.

The neutron-shielded box surrounding the target system is equipped with sensors for temperature, humidity and smoke. The Safety and environment Monitoring System (SMS) monitors these environmental parameters inside the box, detects the presence of smoke and monitors the status of the cooling system. The SMS also acts as an interlock for the CAEN power supplies. If an alarm condition is detected, it can turn them off without relying on the DCS being functional.

### 1.3.5 Data Quality Monitoring (DQM)

The Data Quality Monitoring (DQM) is fundamental to ensure that useful data is recorded and to verify that all the sub-systems of the experiment operate correctly. The DQM process runs on the second computer server located at the surface and reads in real-time the data file that is being written by the DAQ server. The process performs the conversion to the offline data format and makes this data available to the DQM agents, which process it and displays the results in the ECS.

# 1.3.6 Experiment Control System (ECS)

The Experiment Control System (ECS) is the top-level control of the experiment online system, providing a unified framework to control the hardware and software components, and to sequence all data taking operations [1]. A hierarchical architecture has been implemented in which the ECS is a layer above the other online systems, preserving their autonomy to operate independently. With this architecture, the various online components do not strictly require the ECS to operate, e.g. detector calibration and data taking are stand-alone processes. The ECS also performs the logging of the relevant detector information, either in ELOG or in databases depending on the type of information. The ECS consists of two main software components: the ECS Process Manager

(EPM) and the ECS Graphical User Interface (GUI). The software is written in C++ and the inter-communication with the DAQ and the DCS system is done with Python scripts. The EPM is a process which runs on the main server and acts as the communication link between the different online system components. It takes care of starting them and continuously monitoring their status. The ECS GUI has been designed to ensure a simple and compact view of the run control, status of the sub-detector and of the peripheral systems. The main windows of the ECS GUI is shown in Figure 1.10. The ECS is designed to operate the online system automatically, controlled by a global finite state machine that receives the status of the LHC and of the detector to perform predefined actions in order to run the data taking and recover from errors. The LHC machine states are received from the LHC Data Interchange Protocol system, the power supply and environment conditions from the DCS, and the data acquisition status from the DAQ boards and the DAQ server. SND@LHC takes data non-stop: the run starts at flat top (the state declared by LHC after the proton beams are accelerated, just before the beginning of collisions) and, as soon as a new LHC fill starts, the ECS automatically stops the current run and starts a new one. Furthermore, the ECS can reboot a board that has become unresponsive, stop the DAQ and cut the power to the boards in the neutron-shielded box if the temperatures rises above the thresholds, try to restore a tripped SiPM bias channel, etc.

#### 1.4 Offline software: sndsw

sndsw is the SND@LHC offline software framework. Its public GitHub repository can be found in [11]. It is based on the FairShip framework developed by the SHiP collaboration which in turn is based on FairRoot software [12] for detector geometry modelling, making use of the automatic Python bindings provided by PyROOT. sndsw uses both Python, for managers, and C++, for classes and time-consuming tasks.

#### 1.4.1 sndsw structure

The main parts of the sndsw structure are:

• /shiplhc: class definitions for detector, points, hits, clusters, reconstructed tracks, event header. Moreover, it contains applications and managers used when transforming detector signals to hits, from DAQ format to offline software format, and



Figure 1.10: The main window of the ECS graphical interface. [1].

some Python scripts for 2D event display, data monitoring, alignment;

- /shipdata: class definitions for Monte Carlo simulations;
- /python: macros for units definition and tracking;
- /sndFairTasks: class definitions and macros for digitization and raw data conversion;
- /geometry: macros for the detector geometry;
- /macro: macros for Monte Carlo simulations and some Physics analyses.

#### SND@LHC computing model

The computing model of the SND@LHC experiment is depicted in Figure 1.11. The raw data come from the DAQ boards, already subdivided in events by the event building procedure in Section 1.3. The raw data conversion, that includes the application of calibration constants, is run centrally by the SND@LHC computing team, with macros contained in /sndFairTasks. The converted data can be eploited by the SND@LHC users to reconstruct events and perform Physics analysis.

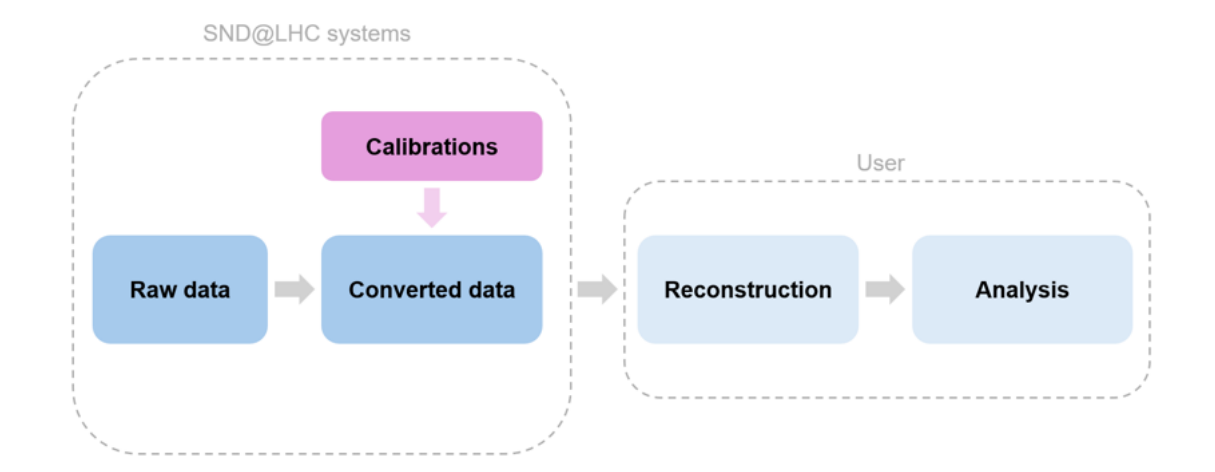


**Figure 1.11:** Scheme of the SND@LHC computing model. The conversion from raw to converted SND@LHC data is run centrally by the SND@LHC computing team, to supply the users with data that can be exploited for events reconstruction and Physics analysis.

# 1.5 Event reconstruction and background

#### 1.5.1 Event reconstruction

The identification of the neutrino flavour in charged current interactions proceeds through the charged lepton identification, that is produced at the primary vertex, see Figure 1.12.  $e/\pi$  separation is achieved thanks to the ECCs, characterized by micrometric accuracy and fine sampling - in this way, the photon conversions downstream of the neutrino interaction vertex can be potentially identified. Muons, instead, are identified by the presence of a track penetrating the whole muon system. Finally, the tau leptons signature lies in the ECC event topology, where the tau decay can be inspected. FIPs will be identified through their scattering off electrons and nuclei of the emulsion target material. In the case of a FIP elastic scattering off atomic electrons, the experimental signature consists of an isolated recoil electron that can be identified through the development of an electromagnetic shower in the target region. For FIPs interacting elastically with a proton, instead, an isolated proton will produce a hadronic shower in the detector.

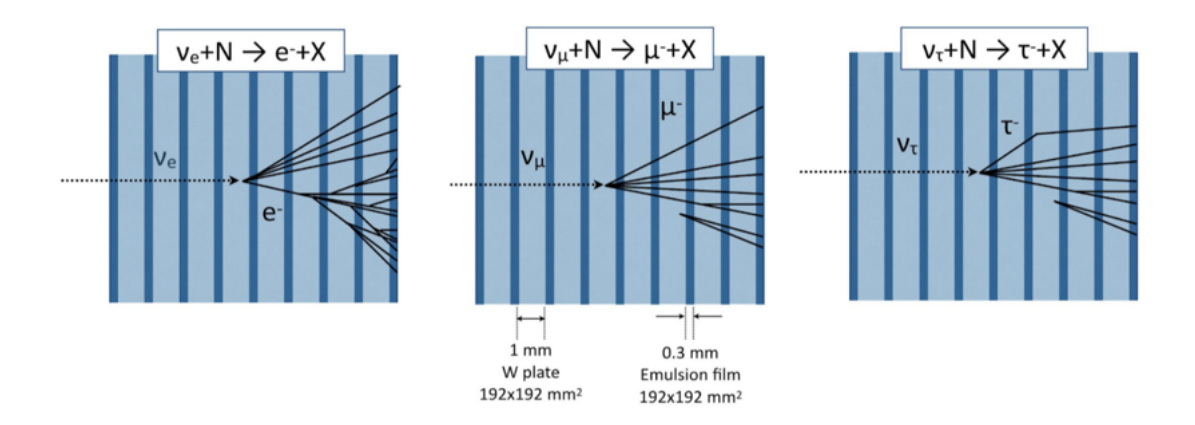


Figure 1.12: Event signatures for different neutrino flavors, identified by the lepton produced at the primary vertex:  $\nu_e$  produces an electromagnetic shower;  $\nu_{\mu}$  originates a muon detected by the muon system;  $\nu_{\tau}$  results in a tau decay in the ECCs.

#### 1.5.2 Background sources

At the detector location, muons constitute the primary source of background. In neutrino searches, backgrounds from machine-induced sources generally decrease both with increasing distance from the interaction point and with greater separation from the beam line [1].

Muons, originating from upstream interaction in the rock separating IP and the detector, can mimic neutrino signals through two distinct mechanisms: they can either arrive with such an angle that they enter directly into the target, undetected by the Veto system and then generate showers in the target both via bremsstrahlung or deep inelastic scattering, or they can make secondary interactions with the surrounding materials producing neutral particles that can enter in the target region and mimic neutrino events [8].

The background from muons is estimated using both the muon flux expected within the fiducial volume and the inefficiency rate of the detector's Veto planes. In 2022-2023 the inefficiency of the Veto system, composed of just two scintillator planes, was dependent on the data taking condition but the optimal value was measured to be  $(7.8\pm2.8)\times10^{-8}$  on a fiducial area of  $35\times35$  cm<sup>2</sup>, corresponding to a target coverage of  $\sim64\%$  [9]. The third Veto plane allowed the reduction of the inneficiency to  $(4.9\pm1.9)\times10^{-9}$  on the full area in 2024. The predicted muon flux, based on Monte Carlo simulations, is approximately  $1.69\times10^4$  fb/cm<sup>2</sup>. Data collected during 2022 shows a good agreement

with these predictions [13].

Neutral particles, such as neutrons and  $K_L^0$  mesons, pose an additional background. These particles can be produced when primary muons interact with the surrounding rock and concrete and may create showers in the target if they enter undetected by the electronic detectors. However, such events are largely mitigated by the Veto system, which detects accompanying charged particles generated during the primary muon interaction. Simulations of the energy spectrum of neutral hadrons within the fiducial volume further validate this mitigation, demonstrating the effectiveness of the Veto system in the exclusion of such particles from the neutrino signal, as shown in Figure 1.13.

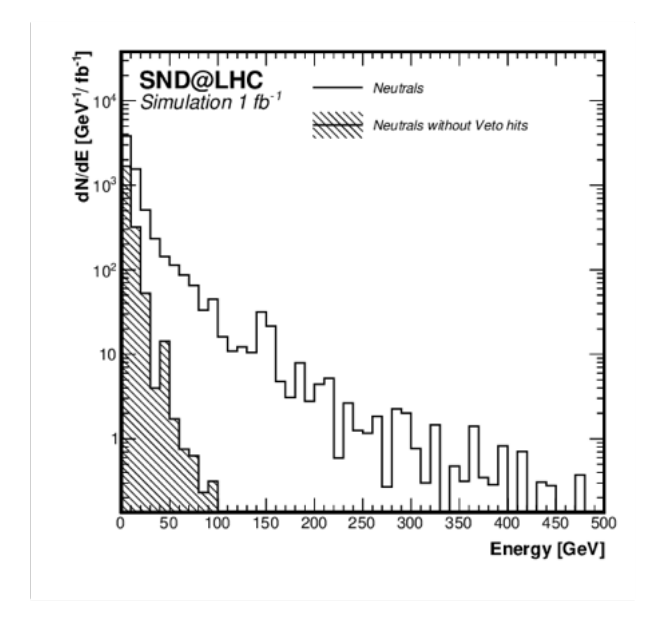


**Figure 1.13:** Energy spectrum of neutral hadrons produced by muon interactions in the rock and concrete entering the SND@LHC acceptance. The dashed line shows the spectrum after rejecting events with hits in the Veto detector [14].

# 1.6 Motivation for SND@LHC muon detectors upgrade

The SND@LHC muon detectors upgrade was supported by a strong motivation: the limited bar thickness (1 cm) of the DS scintillating modules results in a non-optimal determination of the points where reconstructed muon tracks cross the target region.

This directly affects the achievable performance, e.g. the requirement for matching the reconstructed track and the shower centroid. Acknowledging the limit imposed by multiple scattering, which strongly depends on the crossing particle energy, many Physics analyses would benefit from more precise tracking.

A preliminary study showed that, adding 4 points in the x and y coordinates, with  $250\,\mu\text{m}$  resolution, could not only improve the resolution of reconstructed tracks by a factor of two, but also smooth out the multi-peak structure observed in DS bar tracking. The detectors that can provide this type of measurements are the MiniDT modules, described in Chapter 2.

This study was carried out on a MonteCarlo sample of a muon particle gun with energy ranging from 100 GeV to 1 TeV. Figure 1.14 shows the position difference between the track reconstructed with the sndsw algorithm using SciFi information (considered as the true position) and the extrapolation of the track reconstructed with the same algorithm but from the muon system points, with (red line) and without (black line) the inclusion of the MiniDTs. The additional information from the MiniDTs not only improves precision but also mitigates the multi-peak structure observed in DS bar tracking.

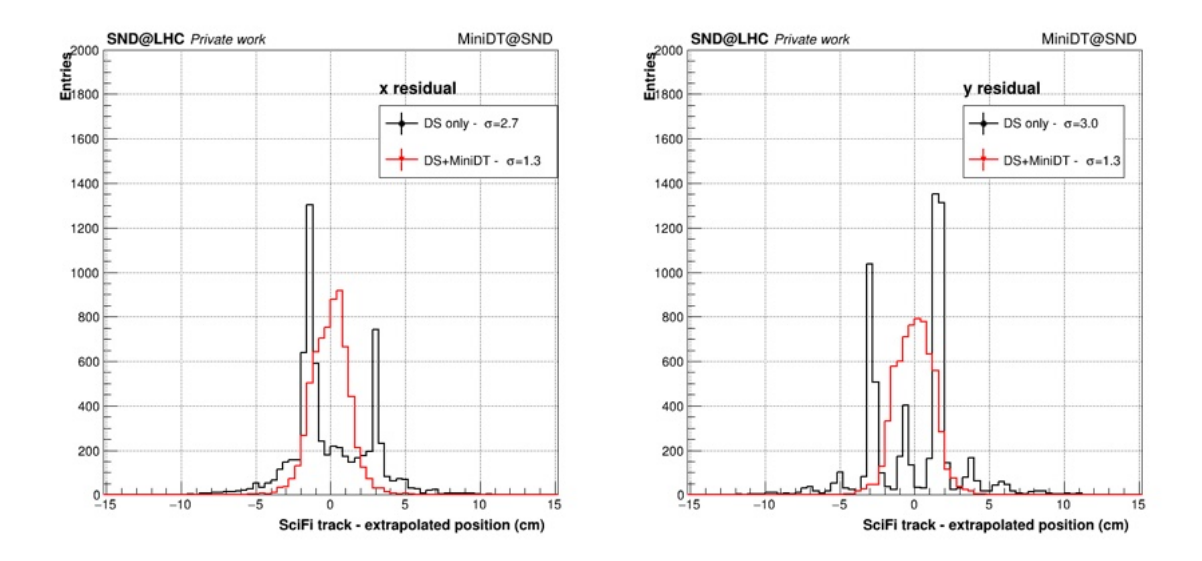


**Figure 1.14:** Distribution of residuals for DS-only tracks (black) or DS+MiniDT tracks (red). The difference is computed between the reconstructed SciFi track and the track extrapolated from the muon system to the target region.

Figure 1.15 summarises the overall improvement, showing in the two cases the dis-

tribution of  $\Delta R = \sqrt{(\Delta x)^2 + (\Delta y)^2}$  where  $\Delta x$  and  $\Delta y$  are the event-by-event residuals computed as described above.

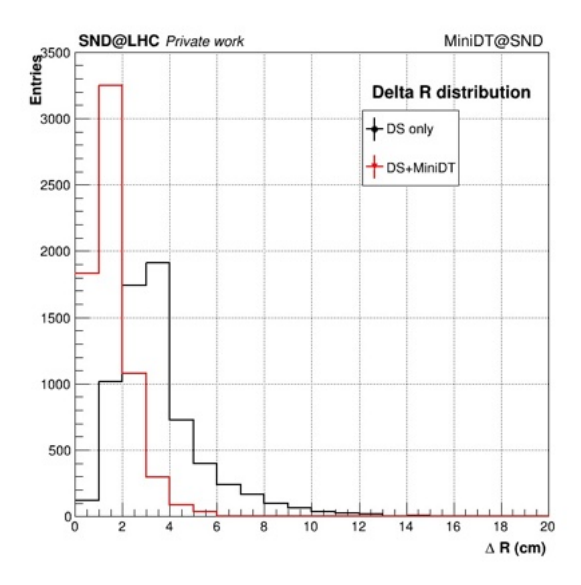


**Figure 1.15:** Distribution of  $\Delta R = \sqrt{(\Delta x)^2 + (\Delta y)^2}$  for DS-only tracks (black) or DS+MiniDT tracks (red).

Finally, Figure 1.16 shows the average of the residual distribution as a function of the incoming particle momentum. It is worth noting that the MiniDT information also reduces the momentum dependence, as the distribution remains stable in both coordinates, while the DS-only tracks show a worsening of the resolution approaching 1 TeV.

In this simple simulation, the MiniDTs are included as a total of 8 additional points: four horizontal and four vertical. Even if the simulation does not account for detector inefficiencies, it is evident that this redundancy will positively affect the tracking efficiency, considering the current requirement of 3 points per coordinate. Moreover, each chamber would provide enough information to produce a stand-alone track segment.

The MiniDTs track segments could be exploited to provide seeds for the tracking algorithm, or to enable matching between DS and MiniDTs at the track level rather than at the level of measured points. A study is currently underway to identify the optimal strategy for fully leveraging the new subdetector capabilities.

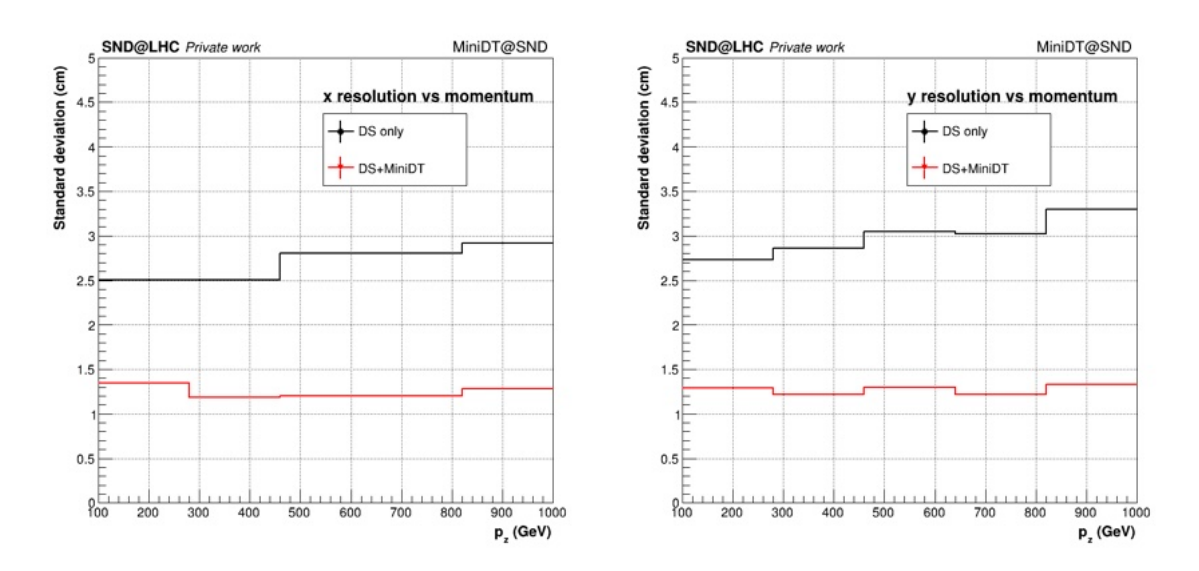


**Figure 1.16:** Distribution of resolution for DS-only tracks (black) or DS+MiniDT tracks (red) as a function of momentum.

# 2 | The MiniDT detectors

This chapter gives an overview on the Mini Drift Tubes (MiniDT) detectors, from their construction to the tests that were performed on them before their installation in the SND@LHC experiment. Since the MiniDTs are miniature versions of the CMS Drift Tubes, Section 2.1 presents briefly the original detector; Section 2.2 shows the MiniDTs structure, electronics and the type of data they provide; finally, Section 2.3 gives an overview on the tests on the MiniDTs before their installation in SND@LHC.

## 2.1 The Drift Tubes detectors in CMS

The Compact Muon Solenoid (CMS) is a general-purpose experiment that studies protonproton and heavy-ion collisions at the Large Hadron Collider (LHC) [15]. Muons are the signature of most new physics phenomena currently under study, and a valuable probe for precision measurement in high-energy physics. Thus, the CMS detector was conceived and realized with dedicated subdetectors to identify muons, trigger on them, and provide robust and redundant measurements of their momentum over a vast range of kinematic parameters. Drift Tubes (DT) chambers are a crucial part of the CMS muon system, covering the barrel region, as shown in Figure 2.1. The CMS barrel muon detector, in each of the five wheels that make up the detector, is made of four concentric cylinder stations around the beamline called MB1, MB2, MB3, and MB4 from inside out. The first three consist of 60 drift chambers each, while the outer one has 70. Each wheel is further segmented into 12 sectors covering about 30° in the azimuthal view. The DTs are integrated into the return yoke of the magnetic field generated by the CMS superconducting solenoid, allowing the measurement charged particles' momenta. The cylindrical shape of the experiment allows using a coordinate system centered on the nominal collision point. The DT detection technology relies on the fact that, when crossing the instrumented volume, a charged particle ionizes the gas contained in the

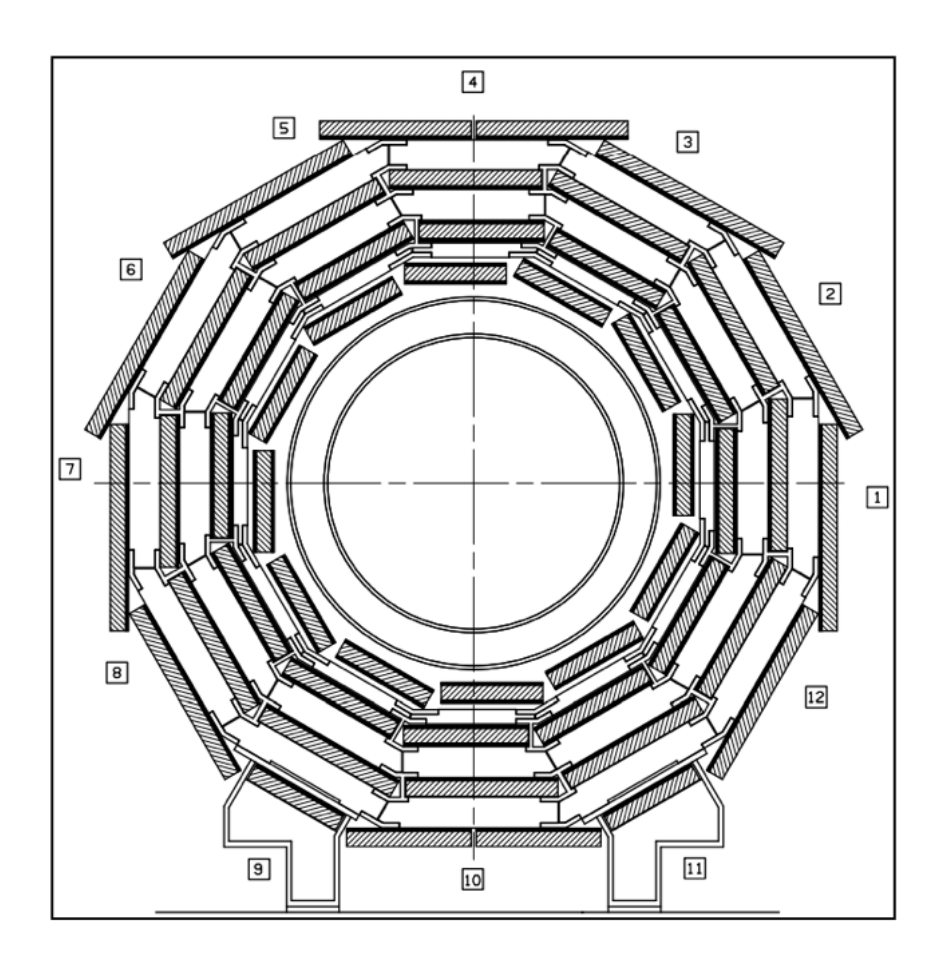


Figure 2.1: Layout of CMS barrel wheels depicting the muon DT chambers [16].

chambers and electrons drift towards an anodic wire, thus generating a signal. In the region close to the wire, the electric field is intense enough to induce secondary ionization, and thus an avalanche multiplication. If the electron drift velocity in the gas mixture is known, the distance between the wire and the charged particle that crossed the tube can be inferred from the measurement of the drift time. This distance has an intrinsic laterality ambiguity, since it may correspond to two possible positions, either left or right of the anode wire. Only during the reconstruction stage, the presence of hits on multiple layers of DTs allows to solve the ambiguity. The distance from the wire can be computed using:

$$x = \int_{t_c}^{t_s} v_d \, dt \,, \tag{2.1.1}$$

where  $t_c$  is the particle crossing time,  $t_s$  is time corresponding to signal collection on the anode wire and  $v_d$  is the drift velocity of electrons inside the cell. For most reconstruction models,  $v_d$  is assumed constant. Therefore, Equation 2.1.1 becomes:

$$x = (t_s - t_c) \times v_d. \tag{2.1.2}$$

A CMS DT chamber is composed of three independent units, called SuperLayers (SL). Each SL contains four layers of rectangular drift cells, staggered by half a cell to allow correlation of drift times across layers for the determination of track coordinates and angles.

The mechanical structure of a SuperLayer is formed by five 2 mm thick aluminium sheets, separated by insulated aluminium I-beams that also define the cell boundaries. The fundamental building block of the DT chamber is the drift tube, shown schematically in Figure 2.2. The number of cells per layer, as well as the tube length, depends on its position in the CMS Barrel, more specifically on how far it is from the interaction point. The largest chambers have up to 96 cells per layer and are up to  $\sim 2.5$  m long.

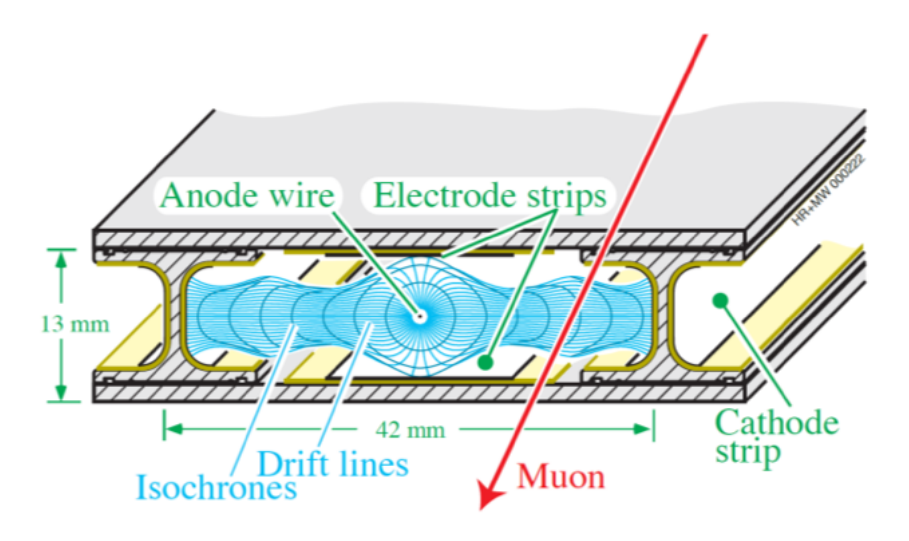


**Figure 2.2:** Schematic view of a single drift tube, constitued by aluminium sheets (top, bottom) and I-beams (left, right). The nominal electric field lines are depicted as well.

Each cell has a pitch of 42 mm and a thickness of 13 mm [16]. Inside each cell, there are five electrodes:

- one anode wire ( $V_{wire} = +3600 \text{ V}$ ): a 50  $\mu$ m diameter stainless steel wire, gold-plated to avoid oxidation. Its role is to collect the signal;
- two strips ( $V_{strip} = +1800 \text{ V}$ ): 14 mm wide and 70  $\mu$ m thick aluminum strip glued onto Mylar tape strips 0.1 mm thick and 20 mm wide. They shape the drift field to achieve a good linearity in the time-space relationship, resulting in a good cell resolution;
- two cathodes ( $V_{cathode} = -1200$  V): 50  $\mu \mathrm{m}$  thick, 11.50 mm wide aluminum tape,

placed on both sides of the I-beams that separate adjacent cells. They electrically insulated from the I-beam by a 100  $\mu$ m thick, 19 mm wide Mylar tape.

This design is optimised to achieve a good performance even if stray magnetic fields are present in some regions of the chambers, necessary in the CMS application. The wires are tensioned at 3.2 N and crimped on solid copper-tellurium blocks of 4 mm side, positioned at the chamber ends. The blocks have a 0.1 mm wide, 0.3 mm deep groove in which the wire is placed. The blocks are inserted into plastic end-plugs, glued to the aluminum plates to define the wire position with respect to each other and in the chamber.

The gas mixture is made of 85% Ar and 15% CO<sub>2</sub>. Argon, being a noble gas, has no electronegativity: this property is crucial to allow electrons to drift through the chamber without being captured. Carbon dioxide, on the other hand, acts as a quencher by absorbing most of the photons produced during the avalanche process. Its presence increases the stability of the detector, extending the efficiency plateau before discharges occur. The chosen ratio between Ar and CO<sub>2</sub> allows for good quenching while saturating the drift velocity of electrons to preserve the space-time relationship linearity. Gas tightness of the SLs is crucial because contamination by the nitrogen or molecular oxygen present in the air can strongly alter the electron drift velocity.

Given the voltages of the electrodes in a cell, the saturated drift velocity is about  $54 \,\mu\text{m/ns}$ , resulting in a maximum drift time of about 400 ns. A single DT cell has a detection efficiency of  $\sim 98\%$  and an intrinsic spatial resolution of  $\sim 200 \,\mu\text{m}$ .

The high voltage (HV) and the front end (FE) electronics are located at opposite ends of the wires. The choice of including electronics inside the gas enclosure stems from the need to reduce connection complexity, dead space, noise, and crosstalk. The FE electronics are separated from the HV distribution circuitry both for insulation problems, and to better employ the space inside the aluminum enclosure and reduce dead space. Moreover, with this design, the chamber provides a unique ground reference for high voltage and signals. The CMS DT electronics that is exploited by the MiniDTs is described in Section 2.2.2.

# 2.2 MiniDTs

MiniDTs are smaller size SL, constructed at INFN Legnaro Laboratory by INFN groups of Bologna, Padova and Torino, using spare material from the original CMS DT chambers [17]. The MiniDT detectors were used in several test beams and in cosmic stands for the development of readout and trigger electronics for CMS DT Phase-2 Upgrade.

#### 2.2.1 Structure

Like the standard CMS SLs, each MiniDT consists of four layers of 16 parallel Drift Tubes cells, for a total of 64 drift tubes per SL. The wire length of the MiniDTs is  $\sim 0.6$  m.

The differences between CMS DTs and MiniDTs are minimal and related to the manual assembly operations. Some of the chamber elements were redesigned to facilitate detector construction while ensuring precise alignment of the cathodes, wires and strips with external positioning tools.

MiniDTs have a custom version of the cells' endcap holding the crimping block (Figure 2.3) designed to exploit the preprocessing of aluminium sheets to have precisely located holes. This allows for better alignment of the cathodes in the chamber and between each other. Figure 2.4 shows how the endcaps are positioned onto the aluminium layer.

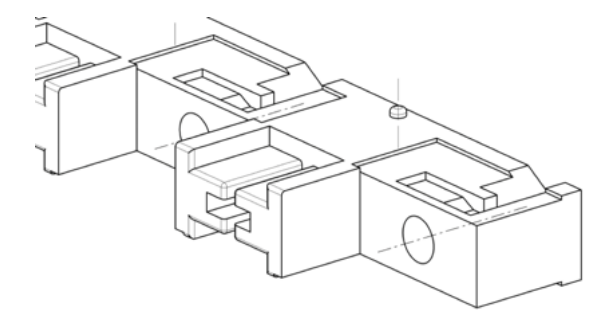


Figure 2.3: Schematic representation of the MiniDTs' endcaps [17].

In the MiniDT case, the wire plugs are truncated cones developed to fit the new endcap design. These are made of insulating material, namely Noryl resin reinforced with glass fibers, and have a small hole to insert the metallic pipe onto which the wire is crimped. This part has a wider section to maintain the correct position with respect to each wire plug. In this way, the crimping pipe also serves as the pin to connect the FE circuitry.

The crimping of the wire is done manually after positioning the wire and tensioning it with a dedicated tool shown in Figure 2.5.



**Figure 2.4:** Positioning of a group of four cathodes onto the aluminium sheet [17].



**Figure 2.5:** Tool used to tension the wires during the MiniDTs' assembly [17].

#### 2.2.2 Electronics

The electronics of the MiniDTs on both the HV and FE sides are the same used in the original CMS chambers. Their description can be found below.

### High Voltage

The HV is distributed using the same six-layers Printed Circuit Boards (PCB) as the CMS DT. Each layer provides the HV to one type of electrode of 8 cells in the same plane. Thus, in total, one PCB provides the HV to 16 cells, 8 per layer in 2 adjacent layers. The voltages are distributed using 50 M $\Omega$  resistors: one per wire and one for every pair of two strips or cathodes. A distributed ground surrounds all connections in the different layers, which are also staggered to avoid crosstalk among the various electrode connections. The connections are made with short wires. The PCB is secured to the aluminum plate between layers by three spring connections that serve as both mechanical

support and a ground connection. HV inputs of the PCBs can be daisy-chained so the number of cells powered by a single primary line will depend on the segmentation in the HV distribution tree.

Differently from DTs, the MiniDTs have a custom HV connector, shown in Figure 2.6, for connecting to various HV boards. This connector allows for the partitioning of a chamber so that if a cell experiences issues that make it unsuitable for data taking, the corresponding section of the MiniDT may be easily turned off. In particular, in a MiniDT, each layer of strips and cathodes could be powered independently. For the wires, an even finer segmentation was implemented: each half layer could be operated separately.

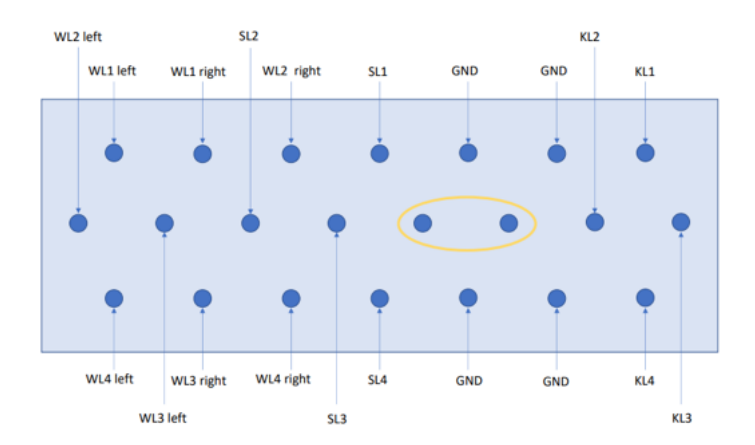


Figure 2.6: Scheme of the internal view of the HV connector. Each pin is connected to either the wires (W), the strips (S) or the cathodes (K) of one of the four layers (L1-L4). The wires input is segmented in order to divide the left and right halfs of the chamber. The pins in the yellow circle are connected together inside the chamber and can be used as an interlock. [17].

An HV splitter box for each MiniDT was built, to interface standard HV power supplies with the on-chamber HV connector. Such boxes feature three standard coaxial HV connectors, corresponding to anodes, cathodes and strips, and a multiconductor HV cable to plug into the MiniDT. Within the box, HV is distributed to all partitions mapped onto the MiniDT HV connector, as long as no problems require disconnecting any of them.

#### Front End boards

The MiniDT FE boards are the same as the one used for the CMS DTs. The first step of the FE circuitry consists of PCBs, one for 4 channels on the 4 layers, that have HV decoupling capacitors, connected to the anodes via a short wire. As for the HV side, the PCBs are fixed to the central aluminum plate with spring contacts that provide mechanical support as well as a ground connection. The decoupling boards are connected to the FE Boards (FEB) via strips of contacts. The FEBs are multilayer PCBs to have the input and output lines on different layers, separated by a ground plane. FEBs also have a temperature sensor and a trimming circuit for the thresholds. A common threshold line connects all of the FE PCBs in a MiniDT.

The frontend electronics amplify the signals from the detector, compare them to a threshold and send the output logic signal to the following part of the readout chain. The amplifier must have low noise to allow operating the DT at low gain, which is essential for the chambers' lifetime. Moreover, it must have a fast shaping time not to worsen the spatial resolution. The comparator has to be fast and precise so that the time response is independent of the signal amplitude.

Figure 2.7 shows the FE circuitry in a MiniDT: one of the HV decoupling boards can be seen, while the other three are hidden by the FEBs.

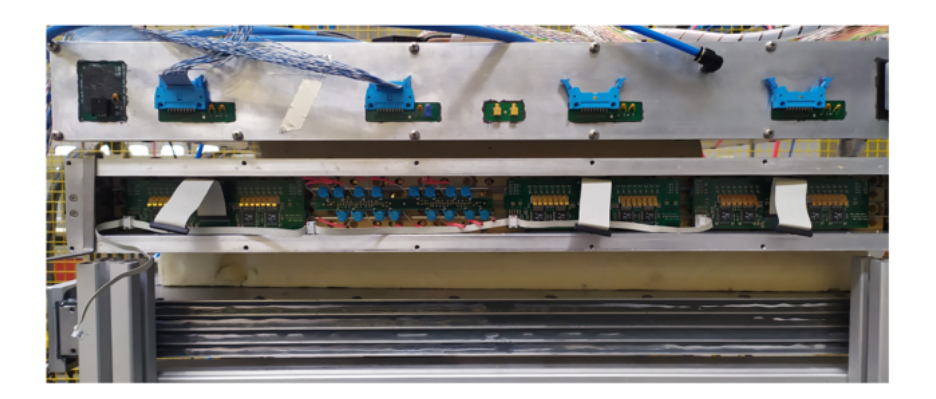


**Figure 2.7:** MiniDT FE circuitry. Only three out of the four FEBs were applied at the moment of the photo, showing the HV decoupling capacitor boards [17].

#### Low Voltage Front End control board

The low voltage powering and control of the Front End electronics in CMS Drift Tubes chamber is based on a system of so-called Splitter Boards, developed to implement the complex, distributed powering of multiple, large chambers in CMS. To simplify the operation of the MiniDTs, a custom board was designed in Legnaro and developed and implemented by the electronics service of INFN Bologna. This board, called Low Voltage Front End (LVFE) and shown in Figure 2.8, is powered with 12 V and provides all needed voltage levels to the FEBs. It handles the configuration and monitoring through the chamber I2C bus and can generate the voltage levels for the FE discriminator using Digital to Analog Converters (DAC). The LVFE board is also controlled by an I2C bus.



Figure 2.8: LVFE board for MiniDTs [17].

# Time to Digital Conversion: On Board electronics for Drift Tubes (OBDT-Theta)

A new readout board for the digitization of the CMS (Compact Muon Solenoid) Muon Drift Tube (DT) chambers has been designed in order to cope with the increase of occupancy and trigger rates expected during operation under the foreseen luminosity in the HL-LHC (High Luminosity Large Hadron Collider) [18], for the CMS DT Phase-2 Upgrade. The board OBDT-theta (On-detector Board for Drift Tubes) can perform the time digitization and readout of the DT chamber signals, produced by SuperLayers, measuring the  $\theta$ -coordinate (z-coordinate along the beam axis) of CMS. The OBDT-Phi board, measuring the  $\phi$  coordinate (x-y transverse plane to the beam axis) [19]

exists as well, but the OBDT-Theta was the chosen one for the MiniDT setup. In the OBDT-Theta, a total of 228 channels can be digitized with a time bin of 0.78 ns and full streaming of all the DT chamber signals can be made through optical links into the CMS counting room. There, the full detector information can be available to perform the trigger and event building logic. Given that the MiniDTs have only 64 channels each, only 128 OBDT channels are used.

The OBDT receives the discriminated signals from the FE electronics and performs the time to digital conversion. The multi-channel TDC is implemented on a radiation-hard FPGA, a Microchip Polarfire FPGA MPF300T-1FCG1152E.

The OBDT-theta board needs to be synchronized with the LHC 40.078 MHz clock and thus, it uses the lpGBT [20] ASIC from CERN that provides the clock and fast timing signals reception as well as a communication link for configuration and monitoring.

The FPGA, after performing the time digitization, needs to funnel the information into one or several high speed links for transmission to the backend. Up to 6 high-speed links, which use the lpGBT protocol at 10.24 Gpbs, are output from the FPGA and sent through optical fibers using two VTRX+ [21] optical transceivers from CERN.

The overall architecture of the OBDT-theta board is shown in Figure 2.9 and an image of the OBDT-theta board is shown Figure 2.10.

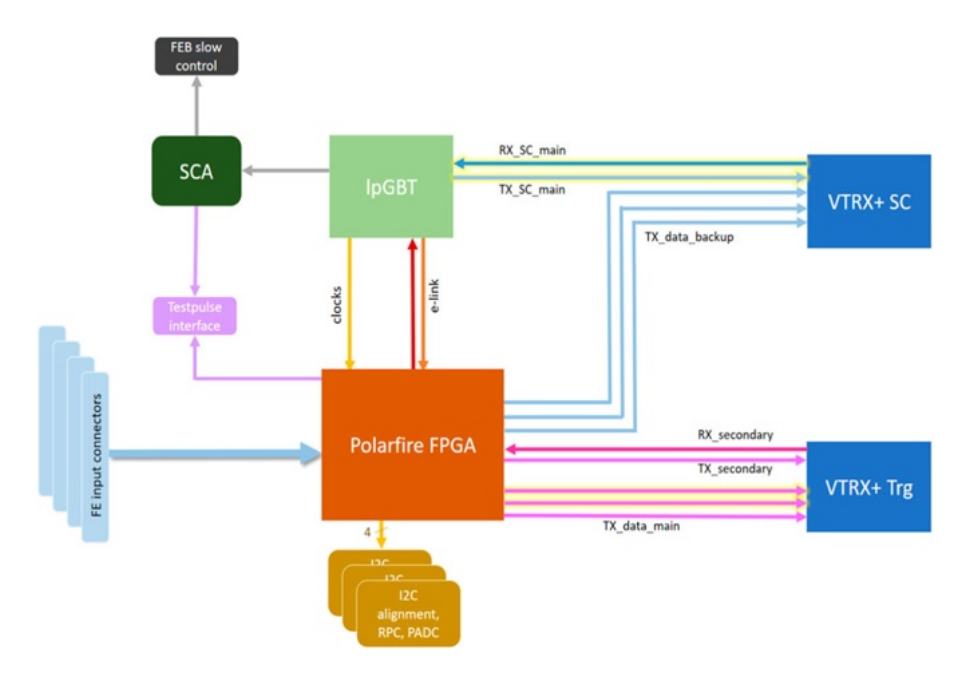


Figure 2.9: Architecture of the OBDT-theta board with its main components [18].

As mentioned, the time digitization of the input signals is performed inside the FPGA,



**Figure 2.10:** Image of the final OBDT-theta board assembled in its mechanical structure together with the OBDT-theta testpulse board [18].

and both a coarse and a fine time measurement are performed. The coarse measurement is performed with a 12-bit counter driven with a 40 MHz clock, *i.e.*, the counting unit is 25 ns. Its dynamic range is reduced from 4096 to 3564, in order to stay synchronized with the LHC orbit.

The fine measurement of the signal within the 25 ns interval is performed using a descrialization method inside the FPGA. A descrializer module is implemented on each of the 228 differential input channels and is operated at 640 MHz in DDR (Double Data Rate) mode, that is effectively 1.28 GHz, which provides a time bin of 0.78 ns. Therefore, up to 5 bits are used to code the fine time measurement.

Both the coarse and fine time measurements of each signal are combined with the information of the channel number to provide a 25-bit digital word. All the time measurements are referred to a periodic signal called BC0 (Bunch Crossing 0), which can be received externally or generated internally. For operation under LHC, this signal is expected to arrive synchronously through the TCDS (Timing and Control Detector System) [22] and mark the start of a new LHC orbit, which is repeated after 3564 clock cycles of 25 ns (i.e., bunch crossings).

The lpGBT ASIC has been designed to interface through the VTRX+ and it is in charge of recovering the operation clock and distributing it to the Polarfire FPGA.

#### Backend: VCU118 Xilinx Evaluation Board

The OBDT is controlled and readout by a Xilinx evaluation board, that implements the backend functionalities. A bidirectional optical lpGBT connection enables clocking, slow control and monitoring of the OBDT, and a further optical link is used for streaming of the TDC data from the OBDT to the backend. A firmware developed by CIEMAT

(Madrid, Spain) CMS group for a VCU118 Xilinx evaluation board [23], based on a AMD Virtex UltraScale+ FPGA [24], was adapted to implement the needed control, monitoring and readout features in the MiniDT setup. Such firmware includes the gigabit transceivers for the communication with the OBDT, IPBus blocks for read/write operations to configuration and status registers, and a Gigabit Ethernet interfaced with the IPBus system.

#### BeagleBone Black

The BeagleBone Black (BBB) is a popular, low-cost, and high-expansion open-source Single-Board Computer (SBC) [25]. Amongst its interfaces, the MiniDTs setup exploits the Ethernet and the USB ports. Its Ethernet port is used for connection from the outside, while one USB port hosts a Digilent JTAG HS3 cable [26] to program and verify the FPGA of the VCU118. User I/O pins are used with a voltage level shifter to interface to the LVFE I2C port, in order to control the MiniDT FEBs.

On the BBB, two Python scripts are essential for the MiniDTs electronics functioning: one is based on the OpenFPGAloader software [27], loads the firmware on the FPGA of the VCU118; the other script controls the MiniDT FE thresholds configuration using built-in I2C command-line tools.

#### TTCrx and QPLL Mezzanine Card: TTCrq

The TTCrq is mezzzanine card hosting the TTC Receiver (TTCrx) ASIC and a Quartz crystal based Phase-Lock Loop (QPLL) [28]. The TTCrx ASIC implements an interface between the front end electronics and the TTC system [29]. The receiver delivers the LHC timing reference signal, the first level trigger decisions and its associated bunch and event numbers. It can be programmed to compensate for the propagation delays associated with the detectors and their electronics. The ASIC supports the transmission of data and of synchronised broadcast commands.

The TTCrq mezzanine is plugged into a custom-built board that provides power and receives the 40 MHz clock and the decoded B-Go commands. The 40 MHz clock is converted to LVPECL and output on two 50  $\Omega$  coaxial cables. The B-Go command bits are connected to user pins on the VCU118 backend by means of jumper wires.

#### **High-Precision Timing Clock board**

The High-Precision Timing Clock (HPTC) generator board for timing characterization is a specialized electronic module developed at CERN that provides a high-quality, low-jitter clock reference for precision timing measurements within experimental setups [30]. The HPTC acts as a high-performance, low-cost frequency synthesizer and clock source.

In the MiniDT readout setup, the HPTC is configured to act as a jitter filter and clock frequency multiplier. It receives the 40 MHz clock from the TTCrx and generates two phase-aligned clocks, at 40 MHz and 320 MHz, routed to the VCU118 by coaxial cables.

#### **SNDPULSE**

The SNDPULSE transformer board was designed and realized by the Bologna group to convert MiniDTs LVDS signals into SiPM-like signals, that can be read out by the SND@LHC TOFPET ASIC. This board is used to monitor the synchronisation between MiniDT and SND@LHC electronics systems, as described in Section 2.3.3.

#### 2.2.3 Data

The MiniDT readout provides two types of data streams, that are stored in output binary files: hits and Trigger Primitive Generators (TPG), which are firmware-reconstructed tracks. The hits stream (and output file) is the same for both MiniDTs, while the TPGs stream are specific for each chamber, resulting in two separate output files.

#### Hits

The MiniDT hits have a 0.78 ns timing resolution. The hit data stream is common for both MiniDTs. Their data format includes the following fields:

- st: the MiniDT identification, to distinguish whether the hit was produced in MiniDT X or MiniDT Y;
- ly: the hit layer;
- wi: the hit wire;
- bctr: the bunch counter, which provides the bunch crossing (BX) number of the hit production time;

• tdc: a fine TDC value (25/32 ns).

#### **TPGs**

TPGs are firmware-reconstructed tracks, that are computed by the VCU118 board, starting from single hits, according to the Analythical Method algorithm in [31]. These trigger primitives contain the information at chamber level about the muon candidates position, direction, and collision time  $(t_0)$ , and are used as input in the L1 CMS trigger. These quantities can be analytically determined from only three hits in different layers belonging to the muon track. Each MiniDT has its own TPG data stream.

Their data format includes the following fields:

• t0: the track collision time;

• position: the track intercept in a reference plane;

• slope: the track slope;

• chi2: the chi-square of the track fit;

• hits: the list of hits the TPG was built with. The hits contain the layer and wire values, and a time value ti, whose origin is the same as the TPG's t<sub>0</sub>. Moreover, two additional fields, valid and lat, provide information about the hit validity (whether it belong to the track or not) and about the hit laterality (whether the hit is left or right of the anode wire, solved with track fitting), respectively.

TPGs can be subdivided into high-quality (H-quality) and low-quality (L-quality) TPGs, if they contain 4 or 3 hits, respectively. L-quality TPGs have poor timing identification, can easily be wrong up to [-50, +50] ns.

TPGs are, de facto, tracks reconstructed at the single MiniDT level, but it was chosen not to use them for offline tracking in SND@LHC, due to the impossibility to calibrate and adapt the firmware algorithm that generates them, which is designed for large CMS Drift Tubes, to the specifics of MiniDT geometry. Nevertheless, they are an important tool in monitoring chamber rates, average hit efficiency and synchronisation, as it will be shown in Section 4.1 and Section 4.2.

## 2.2.4 MiniDT signal distribution

The typical time distribution of hits in a MiniDT, called a "timebox", is reported in Figure 2.11. The timebox shows the time difference between a reference signal and the hits recorded in the chambers: ideally, the distribution should be in the interval between 0 ns for particles crossing a cell next to the anodic wire, and  $\sim 400$  ns if the particle crosses the cell near its edge, but it is shifted by a factor called  $T_{ped}$ , which takes into account the propagation time of the signal along the anode wire and delays due to cable length, readout electronics and trigger latency [17]. The peak at the beginning of the time distribution is due to nonlinear effects in the avalanche region close to the anodic wire and the delta-ray electrons that pass closer to the wire than the muons. The tail of the distribution is affected by the feedback electrons. These particles are extracted from the I-beams or the aluminium sheets delimiting the cell by photons emitted during the avalanche process.

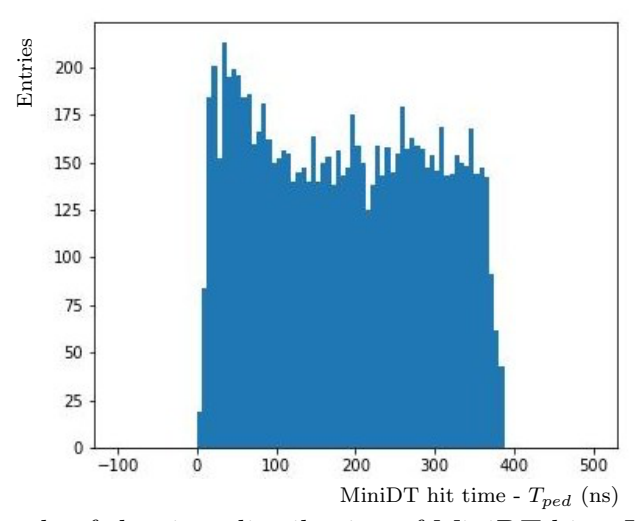


**Figure 2.11:** Example of the time distribution of MiniDT hits. Its characteristic shape is the so-called "timebox".

# 2.3 MiniDTs repairs and tests

Before the installation on the SND@LHC experiment, the MiniDT detectors underwent some tests, to assess their correct behaviour and to perform fixes, where necessary. These tests were carried out both at INFN Legnaro Laboratory (LNL) and at CERN. During these operations, different readout systems were used, and not the final one, which is described in Section 2.2.2.

## 2.3.1 Tests at INFN Legnaro Laboratory

Between October and November 2025, four MiniDTs were tested to identify existing issues that needed to be fixed at LNL. The MiniDTs were arranged in a cosmic rays telescope, visible in Figure 2.12, placed above two reference scintillators (equipped with PMTs) to provided a trigger signal each time a muon crossed either of the two. The chambers were fluxed with  $Ar/CO_2$  85/15 gas mixture. The description of the temporary readout electronics for these tests is beyond the scope of this chapter.

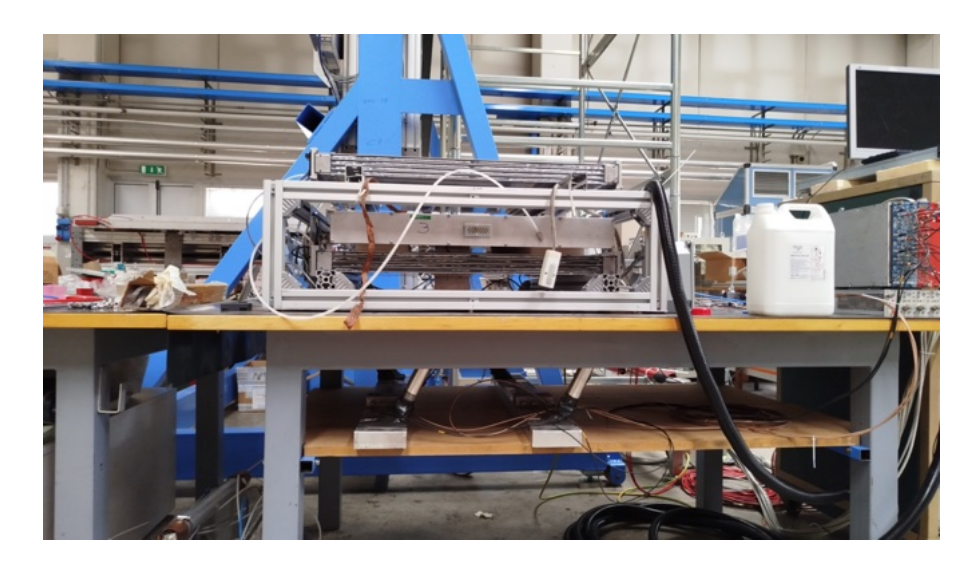


**Figure 2.12:** The MiniDTs cosmic rays telescope setup at INFN-LNL. The MiniDTs are visible in the metallic grid above the table, while two scintillators are placed below the table to provide a trigger signal.

The aim of this test was to inspect the MiniDTs channel by channel, looking for potential issues with gas provision, HVs, LVs. Timeboxes were used as a probe for each MiniDT cell: any deviation from the expected shape of Figure 2.11 can be appointed to a specific problem, as described in the following paragraph.

#### MiniDT issues

The MiniDTs cells may suffer of different types of issues, summarised by the list and figures below:

• Front end issues: a MiniDT FEB board, described might be faulty or broken. The corresponding MiniDT channels timeboxes are empty or with a few random hits (in Figure 2.13, Figure 2.14 and Figure 2.16).

- HV issues: in a MiniDT cell, the anode, cathode or strips might not be correctly powered by the HV, due to unplugged connectors, or there might be HV capacitors in the PCB resulting in timeboxes as the ones in Figure 2.14, Figure 2.15, Figure 2.16, Figure 2.17 and Figure 2.18.
- Gas issues: the presence of air inside a MiniDT cell suppresses the signal, due to the O<sub>2</sub> electronic capture, resulting in the distorted timeboxes of Figure 2.15 and Figure 2.18.

As visible in the timeboxes, issues of different nature might affect the same cell.

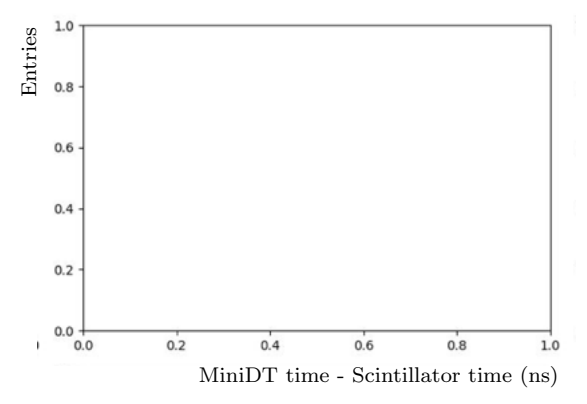


**Figure 2.13:** Timebox for a MiniDT channel with a faulty FEB or a bad anode wire HV connection.

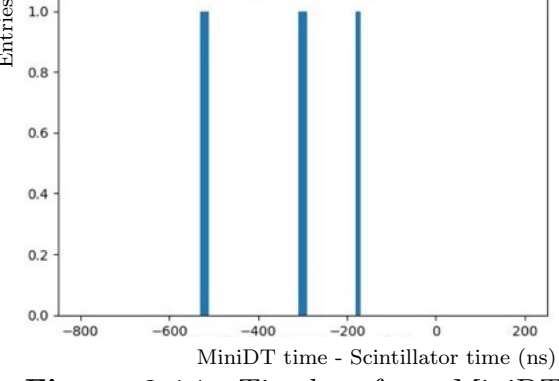


**Figure 2.14:** Timebox for a MiniDT channel with a faulty FEB, or a bad anode wire HV connection but a working FEB.

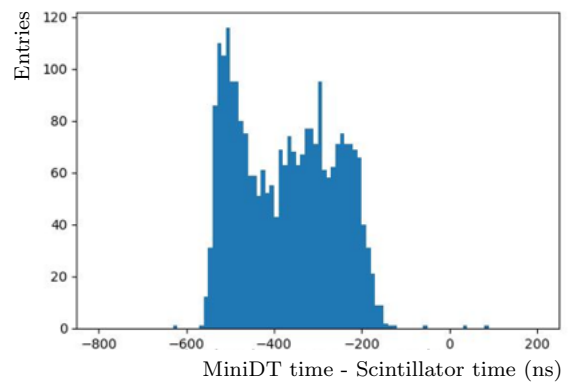


Figure 2.15: Timebox for a MiniDT channel whose cell contains some air, that causes signal suppression, or a bad strip HV connection.

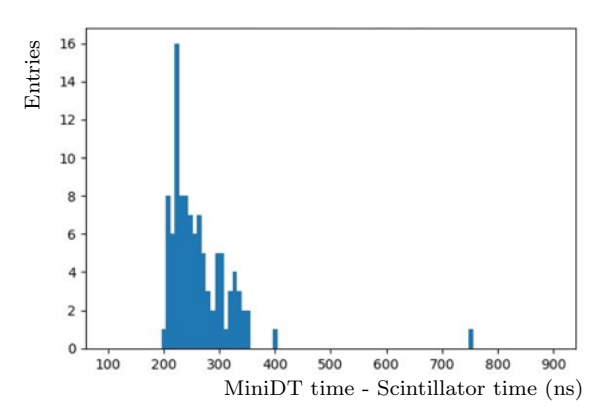


Figure 2.16: Timebox for a MiniDT inefficient channel, that might be affected by either a faulty FEB or a faulty HV capacitor.

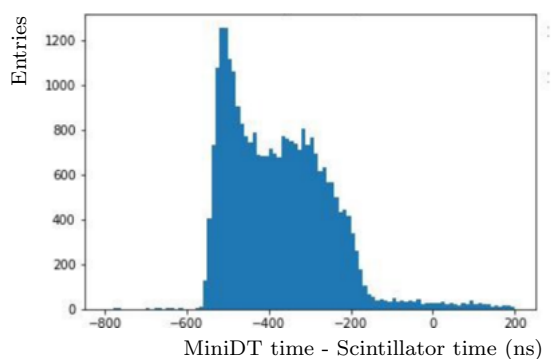


Figure 2.17: Timebox for a MiniDT channel with a bad cathode HV connection, that causes some electrons to drift for a longer time than expected.

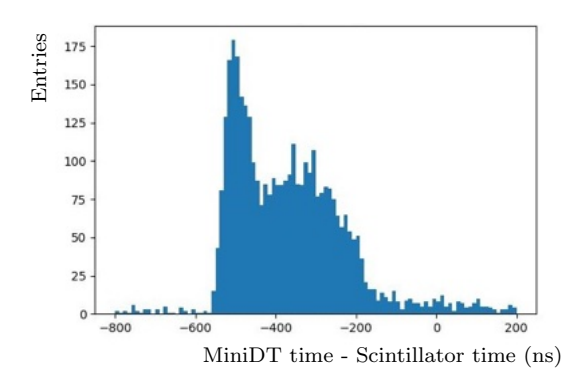


Figure 2.18: Timebox for a MiniDT channel with a bad cathode HV connection and some air present in the cell, that causes signal suppression.

#### **Fixes**

To perform the necessary fixes, the MiniDTs were opened, taking out their covers as in Figure 2.19, where the HV connectors side is visible.



Figure 2.19: An open MiniDT whose cover was taken out on the HV connectors side to perform fixes.

In presence of faulty FEB, they were replaced with working ones.

Concerning bad HV connections, some anode wires were taken out and substituted with new ones; strip pins were reconnected; plastic caps, designed for these fixes, were added to keep cathode pins in place, as visible in Figure 2.20 and Figure 2.21.

Regarding gas issues, some additional Araldite glue was added to the cover frame



(a) Wrong position

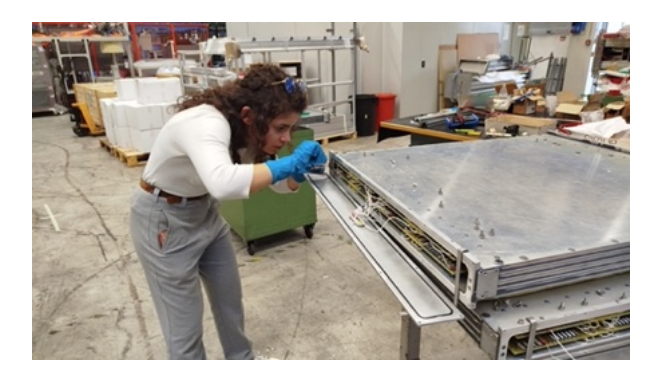
(b) Correct position with cap

Figure 2.20: Cathode pin in wrong position (above) and with the plastic cap designed to keep it in place (below). The pin is positioned in a spare endcap for clarity purpose.



Figure 2.21: The MiniDT cathode fixing procedure.

screws, which were suspected of producing small gas leaks.



**Figure 2.22:** MiniDT gas tightness improvement, by adding extra Araldite glue on the cover frame screws.

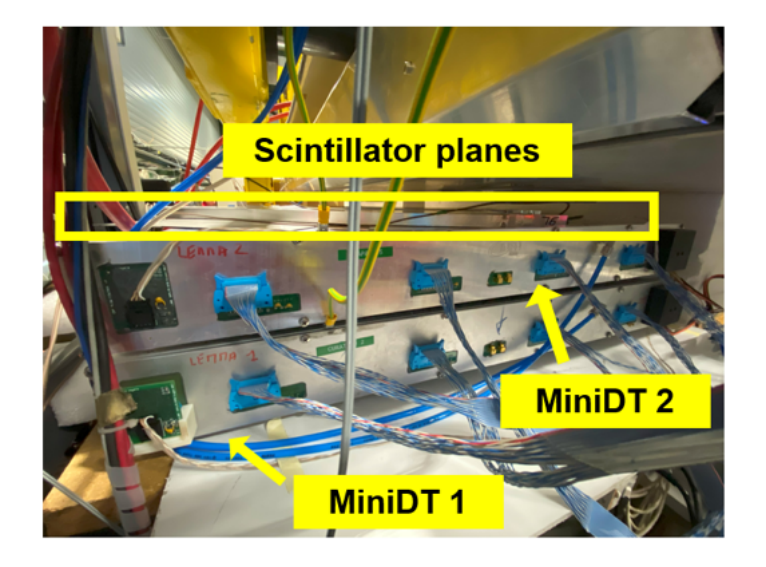
The correct behaviour of MiniDTs was, again, checked with timeboxes, that must resemble the one in Figure 2.11. In total, four MiniDTs were tested and fixed, and two were selected to be installed on the SND@LHC experiment.

## 2.3.2 Tests at CERN

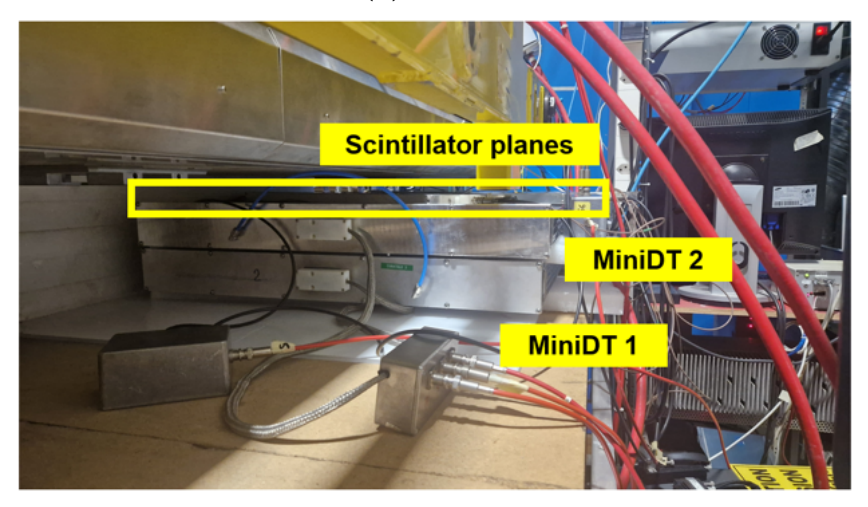
In November 2025, two selected MiniDTs were transported from LNL to CERN and placed inside a CMS surface building, where spare DT chambers are operated. There, the MiniDTs were placed on top of each other, connected to the same gas system as the spare DTs (Ar/CO<sub>2</sub> 85/15 gas mixture) and powered with the HV. In these tests, two reference scintillators, set on top of the MiniDTs, provided a reference signal each time a muon crossed either of them. The setup, front and back, is visible in Figure 2.23. In this paragraph, the MiniDTs are temporarily labeled as MiniDT 1 (the one on the bottom in Figure 2.23) and MiniDT 2 (the one on top). The readout electronics was based on the OBDT-Phi boards [19], developed for the CMS DT Phase-2 upgrade, and on a HiTech HTG-940 evaluation board [19]. Even though this setup was different from the final one in SND@LHC, presented in Section 2.2.2, the electronics allowed to test the MiniDTs with a very similar triggerless system, that was suited to verify the chambers performance.

The scintillator hits were injected into the OBDT together with the MiniDT hits. Timeboxes for each MiniDT channel were obtained by plotting the time difference between MiniDT hit and scintillator hit, confirming that all 128 channels were working as expected.

A combined anode HV and FEB thresholds scan was performed with 1 hour-long cosmic rays runs. Respectively, the anode HV were +3600 V, +3550 V, +3500 V, and in each of them the FEB thresholds were varied and set to 100 mV, 75 mV, 50 mV. For each working point, the whole chamber hits rate rate was computed for both MiniDTs, by counting the total number of hits, dividing by the elapsed number of orbits (1 orbit  $\sim 88.9\,\mu\text{s}$ ) provided by the readout data itself. The MiniDT efficiency was defined as the ratio of events with both a hit in the bottom layer of the MiniDT placed below (in Figure 2.23) and a scintillator signal over the total number of events with a scintillator signal. Due to logistics the scintillator planes could only be placed on top of the two chambers, hence the requirement to the presence of a hit in the bottom layer, to ensure that the muon crossed all layers of the two MiniDTs. As a consequence, the scan only provided information on the efficiency of 7 out of 8 layers of the two MiniDTs. Plotted in Figure 2.24, the trends for the rate and efficiency values can be seen. Considering the working point where *i.e.* the anode wire was HV equal to +3600 V and the FEB thresholds were equal to 100 mV, MiniDT 1 rate was  $\sim 520 \text{ Hz}$  and its efficiency was  $\sim$ 



(a) FE side



(b) HV side

**Figure 2.23:** The MiniDTs cosmic rays telescope setup at CERN. The MiniDTs and scintillators are pointed out by the yellow labels.

97 %, while MiniDT 2 rate was 5 kHz and its efficiency was  $\sim$  97 %. The large noise rate in MiniDT 2 was interpreted as due to the fact that, unlike MiniDT 1, it was never operated for long periods of time, and thus needed more time under gas and with the HVs powered on to reach a stable behaviour. This expectation was later confirmed when operating the chambers in SND@LHC.

Since the last days of December 2025, due to works in CMS surface buildings, the MiniDT HV were turned off. Nevertheless, the chambers were constantly fluxed with gas.

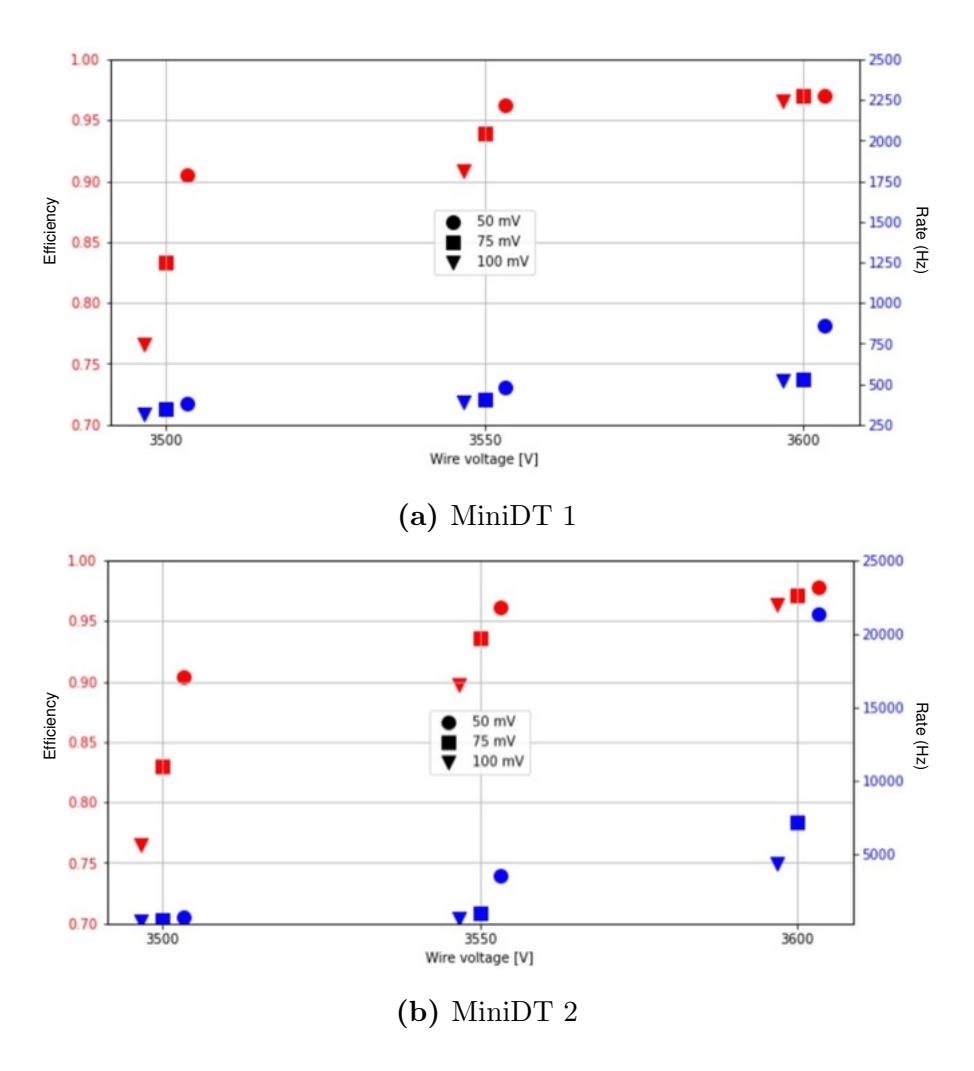


**Figure 2.24:** The trends for the MiniDTs rate and efficiency values in a combined scan of anode wire HVs and FEB thresholds.

# 2.3.3 MiniDTs-SND@LHC DAQ synchronisation tests

The synchronisation test were carried out at CERN, during February 2025, prior to the MiniDTs installation. The goal was to prove synchronisation between the MiniDT DAQ and the SND@LHC DAQ under a common TTC signal.

#### Synchronisation layout

As mentioned in Section 1.3.3, the SND@LHC online event builder packs events in a 25 ns-wide time window. This implies it is not possible to assign MiniDTs hits to a specific SND@LHC event, due to the long drift time that spans the whole [0, 400] ns range (see Section 2.2.4). Therefore, it was chosen to keep separate SND@LHC and MiniDT data streams. To achieve synchronisation between the two streams and

alignement to the LHC machine, at the start of each run the SND@LHC DAQ asserts a TTC command, called Start of Run (SoR) signal, configured to be synchronous to the orbit. This signal generates a MiniDT internal Bunch Crossing zero (BC0) signal that, together with internal orbit and bunch crossing counters, is used by the electronics to achieve synchronisation to the LHC machine.

On top of that, each time the MiniDT backend FPGA (VCU118) firmware finds a muon track in any of the MiniDTs, it asserts a Technical Trigger (TT) bit on an output line, with a fixed latency with respect to the muon track time, having a few nanoseconds precision. This bit is sent to the SNDPULSE board, that converts LVDS signals to SiPM-like signals. The signal is collected and digitised by the TOFPET board, which is connected to a SND@LHC DAQ board allowing to verify the synchronisation between the two readout systems.

#### Synchronisation tests setup

The setup for the MiniDT-SND@LHC DAQ synchronisation tests can be seen in Figure 2.25. These tests were performed in a CERN laboratory, without any MiniDT chamber connected to the setup and without the real LHC and SND@LHC clocks to synch to. In order to carry on the synchronisation verification without real detectors, the VCU118 was set to generate TT bits at a fixed BX in each orbit with a prescale, if needed. The TTC command for synchronisation was instead generated via a VME setup on the TTCvi, a TTC-VME interface. The LHC clock was simulated via a 40.0789 MHz clock generator.

The setup was composed of:

- SND@LHC DAQ server: USB connection to a VME controller and Ethernet connection to a DAQ board;
- TTC crate: equipped with a VME controller (connected via USB to the DAQ server), one TTCvi module (for TTC-VME interface [32]), one TTCex module (for TTC laser encoding and transmission [32]) and a 40.0789 MHz clock generator, to simulate the LHC clock. This setup is a replica of the TTC distribution setup installed for SND@LHC, with the only exception of the interface to the LHC Radio Frequency, which is here replaced by the clock generator;
- Splitter for the TTC signal;

- MiniDTs electronics, described in Section 2.2.2;
- FE board;
- TOFPET board;
- SND@LHC DAQ board;
- MiniDT DAQ server: Ethernet connection to the MiniDTs backend FPGA (VCU118).

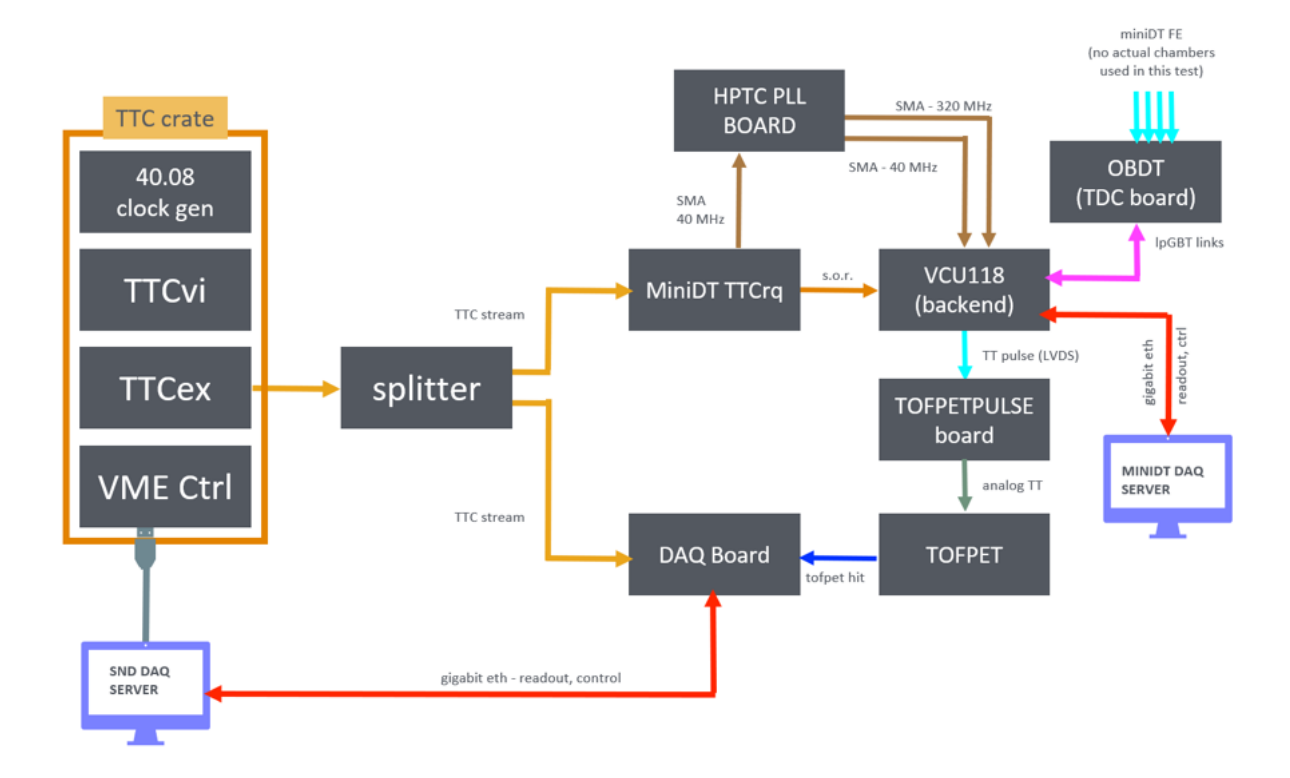


**Figure 2.25:** The setup for the MiniDTs-SND@LHC DAQ synchronisation tests. The arrows are differentiated in colours, accordingly to the type of signal they represent.

#### Synchronisation tests results

This paragraph presents the results of the MiniDT-SND@LHC DAQ synchronisation tests in four different runs. Shown in Figure 2.26 are the BX values of the TOFPET hit as assigned by the SND@LHC DAQ in run 101153 and run 101154, where the TT signal was configured to be timed at the MiniDT-backend BX 1. It can be clearly seen that the SND@LHC DAQ receives the TT bit with a negative timing offset of 2 BX, as measured

by the TOFPET board timestamp. This offset is the same in both runs, proving that synchronisation is consistent in different runs. No prescale was set, with a resulting rate of 11 kHz, *i.e.* the same frequence as LHC orbits, yet the SND@LHC DAQ board measured a rate of 9.5 kHz. This difference is due to the TOFPET board parameters, that were not perfectly calibrated, resulting in some inefficiency in the digitisation.

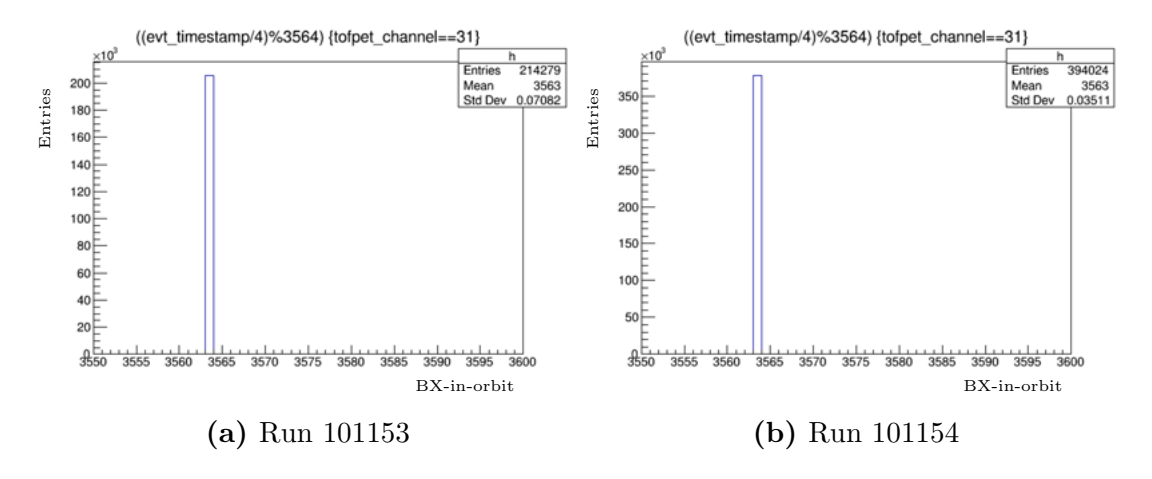


**Figure 2.26:** Results of the MiniDTs-SND@LHC DAQ synchronisation tests (run 101153-101154). The TT signal was set to be 25 ns wide and timed at MiniDT-backend BX 1. The TOFPET registered this signal with a 2-BX offset, at BX 3563.

In run 101155 and run 101156 the TT signal was moved at MiniDT BX 100. In Figure 2.27 most of the TOFPET hits are in BX 98, as expected, but there is a small population in the following BX, probably due to non ideal fine synchronisation between the MiniDT clock and the DAQ board clock.

In conclusion, these tests proved that the MiniDT and SND@LHC DAQ systems are synchronised in several aspects: pulses generated at constant position within the LHC orbit in the MiniDT DAQ are received at constant times in the SND@LHC DAQ; the timing offset between the two systems is constant across multiple runs, and it is consistent for different BXs along the LHC orbit.

In addition, the efficiency for the TOFPET reading of SNDPULSE adapter signals was  $\sim 85-90\%$ , acceptable but not really high. The causes of this inefficiency are to be searched in two facts: firstly, the SNDPULSE board was quickly modified during the tests to make it working, but it was still not optimised, e.g. regarding pulse polarity and coupling capacitance parameters; secondly, the TOFPET discrimination parameters that could be suited for the setup were hastly searched during the same tests. Nevertheless, the observed TT bit digitization efficiency is sufficient to enable a continuous and

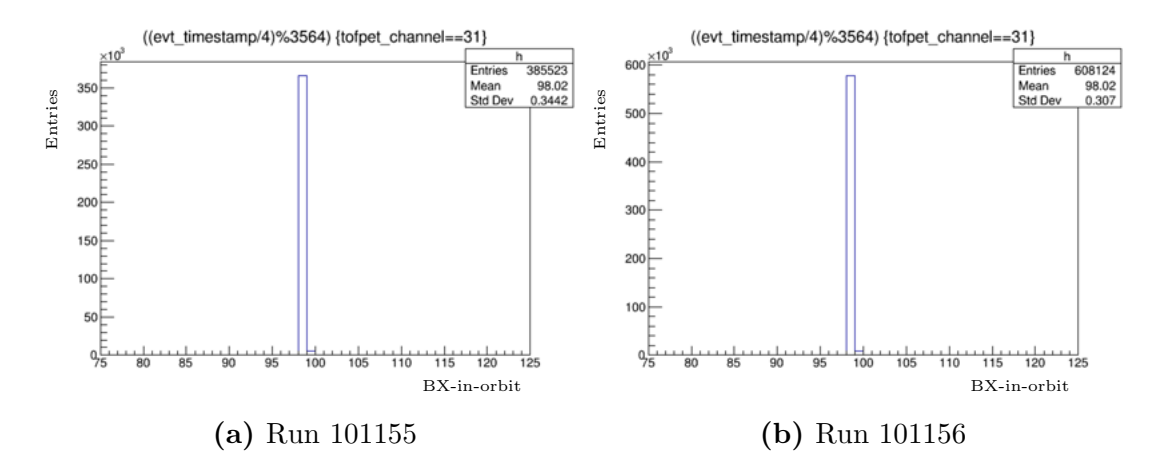


**Figure 2.27:** Results of the MiniDTs-SND@LHC DAQ synchronisation tests (run 101155-101156). The TT signal was set to be 25 ns wide and timed at MiniDT-backend BX 100. The TOFPET registered this signal with a 2-BX offset, at BX 98, with a small population in the following BX, probably due to fine synchronization.

consistent monitoring of the synchronisation between the two DAQ systems.

# The MiniDTs installation and integration in the SND@LHC experiment

This chapter presents the stages of the installation and integration of two MiniDT detectors in the SND@LHC experiment. The installation was carried out during the end of the 2024 Year End Technical Stop (YETS), from March 3rd 2025 up to March 6th 2025.

It is divided as follows: Section 3.1 shows the procedure that was necessary before the installation; Section 3.2 documents the steps and outcome of the installation itself; Section 3.3 illustrates the MiniDTs integration into the SND@LHC DAQ system.

# 3.1 Installation preparation

The preparation for the installation comprised several steps, that can be summarized in:

- Mechanics design and production
- Experimental area (TI18 tunnel) preparation
- Gas provision
- Electronics finalization
- Data storage

# 3.1.1 Mechanics design and production

To install the two MiniDTs at the end of the SND@LHC experiment, several designs for their placement were investigated. The staggered position of SND@LHC in TI18, near the curved wall of the tunnel, and the overall limited space imposed rigid constraints on the chambers placement in the detector muon system.

The final design can be seen in Figure 3.1. The MiniDTs are placed at the end of the SND@LHC detector, in between DS3 and DS4. The MiniDT module closer to the SND@LHC target section is meant for y-position measurements, followed by the one for x-position measurements. From now on, MiniDTs will be referred to as MiniDT X and MiniDT Y. This order was chosen to maximise the overlap beetween the DS system and the two MiniDTs. Due to frontend and HV distribution electronics installed within the gas volume, the chamber footprint extends beyond the active volume on the two sides of the Drift Tubes: this implies that MiniDT Y, positioned with horizontal tubes, needs more space on its sides than MiniDT X, which has vertical tubes. The available lateral space decreases moving away from the target, due to the angle between the SND@LHC detector and the tunnel walls, hence the installation choice. In this configuration, MiniDTs and DS3-4 stations have a 85% overlap.

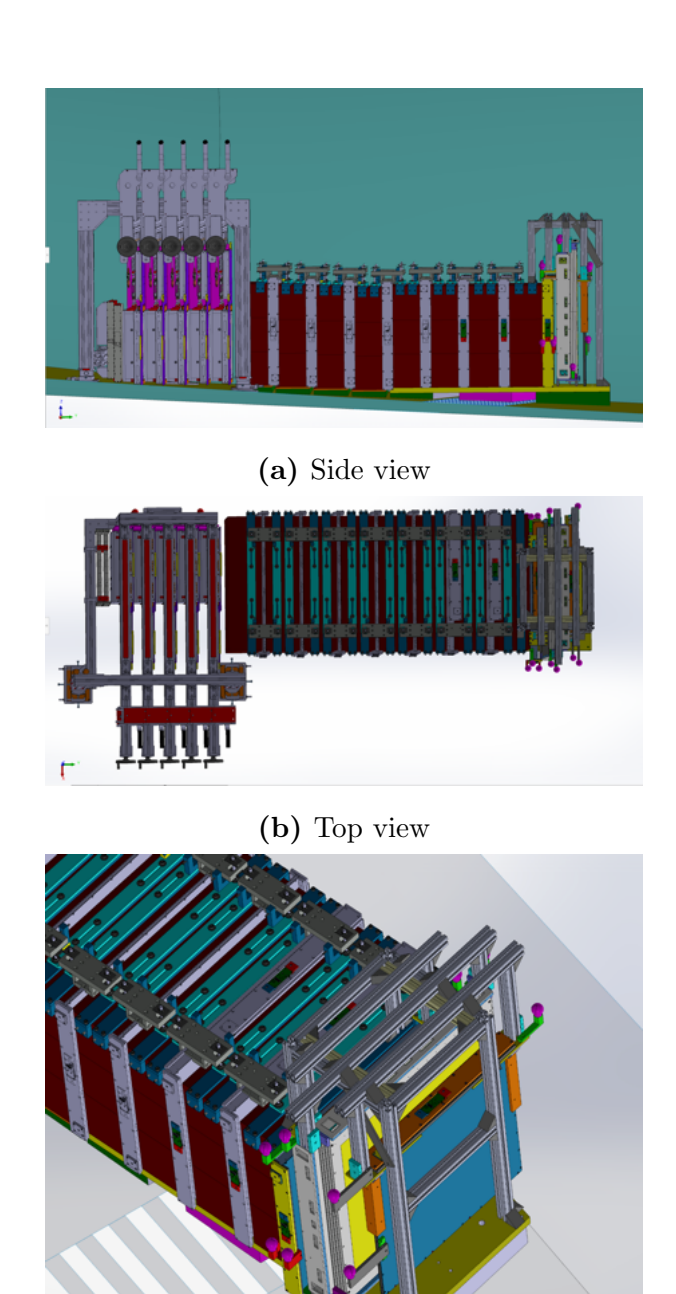
The MiniDTs are fixed to each other, therefore each spatial translation or rotation affects both in the same way. The MiniDTs are placed in and supported by a mechanical frame made of aluminium Bosch profiles and custom parts that connect to the anchor points of MiniDTs. Custom parts of the frame were manufactured at INFN Bologna laboratories, while the whole structure was later assembled with MiniDTs at CERN, in a surface building, for testing; then it was transported, partially assembled, into the TI18 tunnel for the final installation. The frame not only supports the two MiniDTs, but DS 3 and 4 as well.

Compared to the layout in Figure 1.2, DS4 is displaced downstream of the MiniDTs. Moreover, this design foresees the removal of the last iron block in the muon system.

# 3.1.2 Experimental area (TI18 tunnel) preparation

The experimental area had to be prepared to host the new structure: DS3 and DS4 were extracted, to allow the iron block removal (which took place on February 19th 2025), see Figure 3.2.

Concerning the powering for the MiniDTs, it was established to use free channels on an existing LV patch panel (in Figure 3.3), of the SND@LHC electrical frame, for the MiniDT SND@LHC DAQ board and for the 6 LV channels of the MiniDT electronics. On the HV side, a power booster, rented from CERN electronics pool, was installed in the SND@LHC CAEN mainframe to cope with increased power demand. The modules CAEN A7030DN for cathodes (needed two connectors at -1200 V) and CAEN A1833P



(c) Zoom on MiniDTs and DS4

**Figure 3.1:** Final layout of the MiniDTs placement in the SND@LHC experiment, with the two MiniDTs (in gray and yellow) at the end of the detector, between DS 3 and DS 4 (last blue plane).

for both strips and anodes (two connectors for each chamber at +1800 V and at +3600 V, respectively), were installed as in Figure 3.4.



(a) Before



(b) After DS3-4 removal



(c) The removed DS3-4

Figure 3.2: The stages of the DS 3-4 removal, to make space for the MiniDTs mechanical support structure. In 3.2b, the iron block that was later removed.

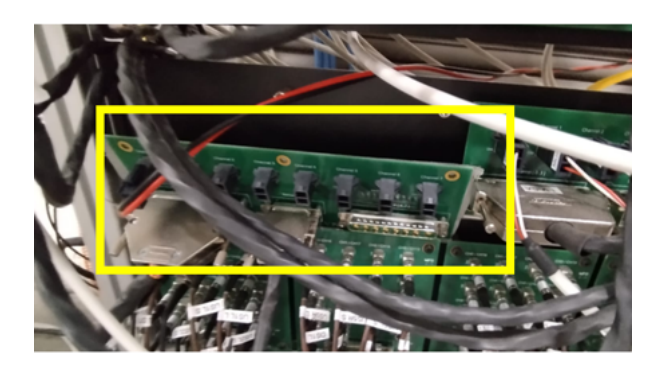


**Figure 3.3:** One of the SND@LHC LV patch panels, with free connectors (highlighted by the yellow rectangle) that can power the MiniDTs DAQ board and up to 6 LV channels for the MiniDTs electronics.



**Figure 3.4:** The HV boards for MiniDTs cathodes (CAEN A7030DN module) and strips and anodes (CAEN A1833P module) powering at -1200 V, +1800 V and +3600 V, respectively.

# 3.1.3 Gas system

The MiniDTs detector, as described in Section 2.2, need to be constantly fluxed with gas, even when they are not powered up, to keep them clean and without air. Since in the TI18 tunnel there was no  $\rm Ar/CO_2$  plant, it was decided to install a gas bottle, with a volume of 50 L and internal pressure of 200 Bar, full of  $\rm Ar/CO_2$  gas mixture in 85/15 percentage. A flux of 2 L/h ensures about two full MiniDT volumes of fresh gas is supplied each day, which is considered the appropriate gas replacement rate to ensure stable performance. One gas bottle should be enough to cover, approximately, six months of activity. The change of the gas bottle can be planned in advance so not to interfere with the LHC activity.

The gas bottle had to be installed in an area where the constant release of  $Ar/CO_2$  or even the sudden emptying of all its contents would not represent a threat to the air

quality, *i.e.* no decrease in the  $O_2$  percentage. Therefore, the position for the gas bottle is outside of the TI18. More precisely, the gas bottle was fixed to pre-existing holes in the tunnel wall, in the (PM15) UJ18 cavern, visible in Figure 3.5. A metallic rail on the wall serves as a guide for the gas pipes, about 15 m long, that link the bottle to the MiniDT detectors.

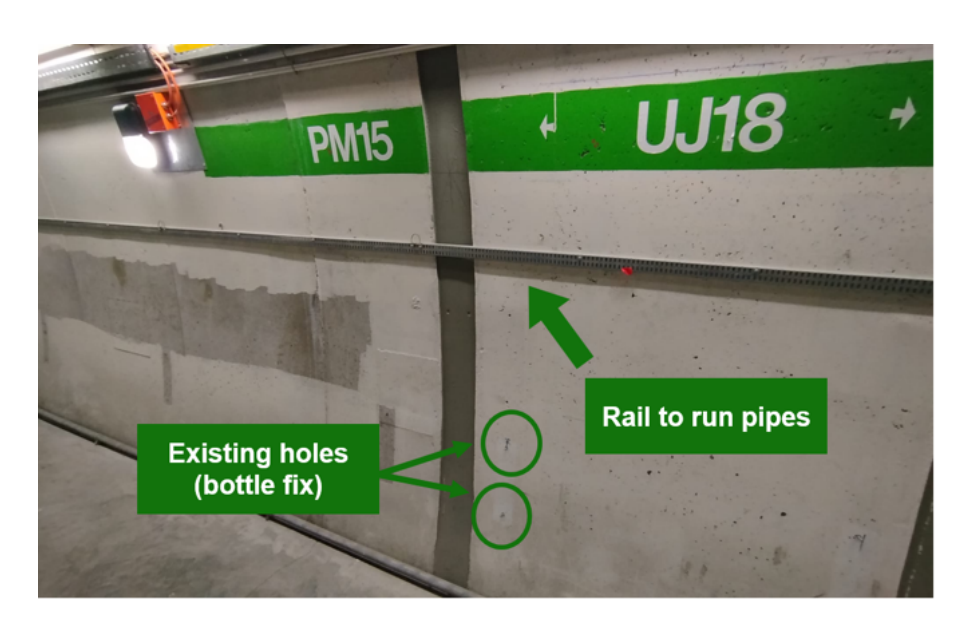


**Figure 3.5:** The UJ18 tunnel wall position for the MiniDTs gas bottle. Highlited in green, the two pre-existing holes to fix the gas bottle and a metallic rail to run the gas pipes that connect the bottle to the MiniDTs.

#### 3.1.4 Electronics finalization

All the MiniDTs electronics boards, described in Section 2.2.2, with the exception of the FE and the SNDPULSE boards, were arranged in a "box" made out of  $50 \times 50 \text{cm}^2$  aluminium grid plates, see Figure 3.6. This box is meant to be fixed to the downstream of the MiniDTs, on their mechanical support. The electronics box is connected to the MiniDTs system, the SND@LHC experiment and the external world by FE, LV and slow control cables; one TTC fiber to deliver the LHC clock; 1 cable that connects to the SNDPULSE; 2 Ethernet cables, one for readout, connected to the VCU118 card, and the other for slow control, connected to the BBB PC. The MiniDTs HV distribution boxes are not part of the electronics box.

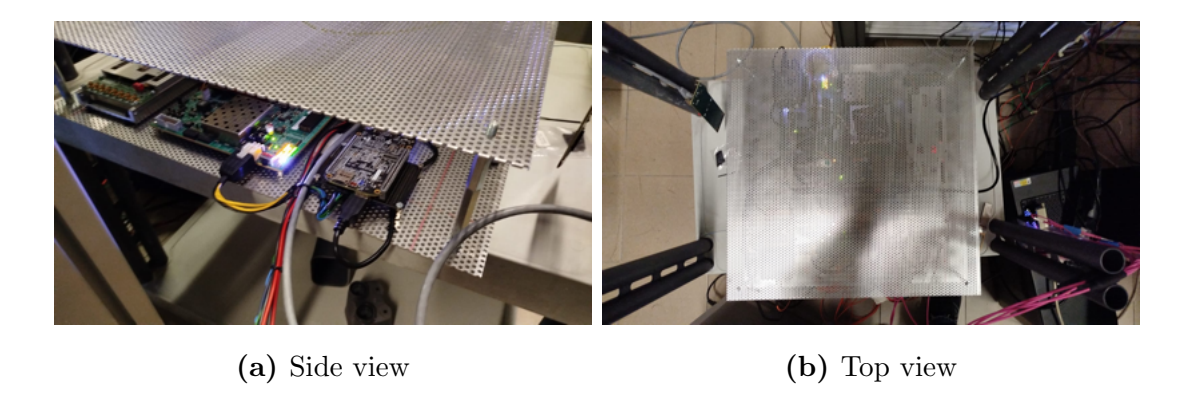


**Figure 3.6:** The MiniDTs electronics box, made out of two  $50 \times 50 \,\mathrm{cm^2}$  aluminium grid plates.

## 3.1.5 Data storage

Since the MiniDT data stream was set to be separate from the SND@LHC data stream, the MiniDT system required the installation of a rack server of its own. The server was installed in a surface building at LHC Point 1. It provides two network interfaces:

- DAQ network to access MiniDT electronics and readout;
- GPN network for remote access.

## 3.2 Installation

This section shows the steps of the MiniDTs installation in the SND@LHC experiment. The installation took place at the beginning of March 2025, at the end of the 2024-2025 Year End Technical Stop (YETS) and just before the start of the 2025 LHC data taking. The installation comprised the mechanical structure assembly, the electronics powering and the gas system finalization.

# 3.2.1 Mechanics assembly and placement

The mechanical structure and the MiniDTs were brought in the TI18 tunnel on a trolley, to trasport them along the LHC and make them cross the tunnel below the beam pipe (Figure 3.7).

The mechanical structure that serves as a support for the MiniDTs and DS3-4 was assembled at the end of the SND@LHC detector, as can be seen in Figure 3.8. Then,



Figure 3.7: The material for the installation, including the MiniDTs and their (disassembled) mechanical support structure, were transported with trolleys low enough to cross the LHC beam pipe from below.

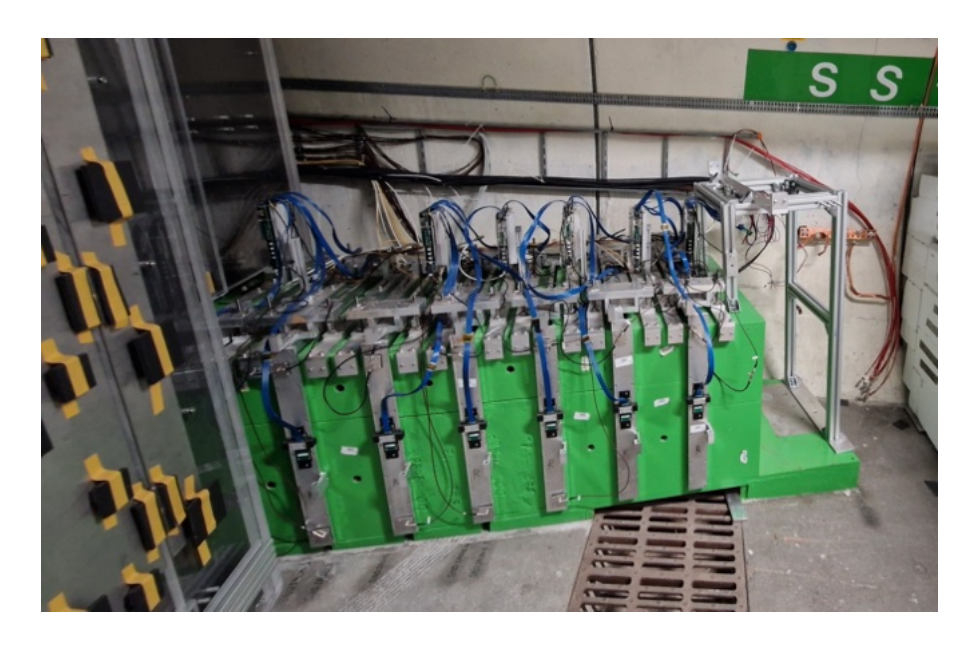


Figure 3.8: The mechanical support structure for MiniDTs and DS3-4, during the assembly.

the detectors were placed in the following order, proceeding from the closest to the SND@LHC target region to the farthest, as established in the designed layout of Figure 3.1: DS3, MiniDT Y, MiniDT X, DS4. Figure 3.9 shows the insertion of the

MiniDTs, while Figure 3.10 shows the final result.



Figure 3.9: Placement of MiniDTs in the mechanical support structure.

The complete SND@LHC detector can be seen in Figure 3.11.

## 3.2.2 Electronics

The electronics box, mentioned in Section 3.1.4, was fixed downstream of the MiniDTs mechanical structure. Figure 3.12 depicts the electronics box without the cover grid.

Visible in Figure 3.13 are the electronics box, with the cover grid on, and, not included in the box, the HV distribution boxes, the SNDPULSE, the FE board and the MiniDT DAQ board.

More details on the LV and HV connections can be found in Appendix A.

#### 3.2.3 Gas circuit

Following what was described in Section 3.1.3, the  $Ar/CO_2$  gas bottle for the MiniDT was transported and fixed in the UJ18 cavern, as can be seen in Figure 3.14. The circulation of the gas mixture in and out of the MiniDTs was achieved by means of copper and plastic pipes ( $\varnothing 8$  mm), that connect the bottles with the detectors and provide the gas link between the two chambers. The gas mixture flows out of the bottle, passes into

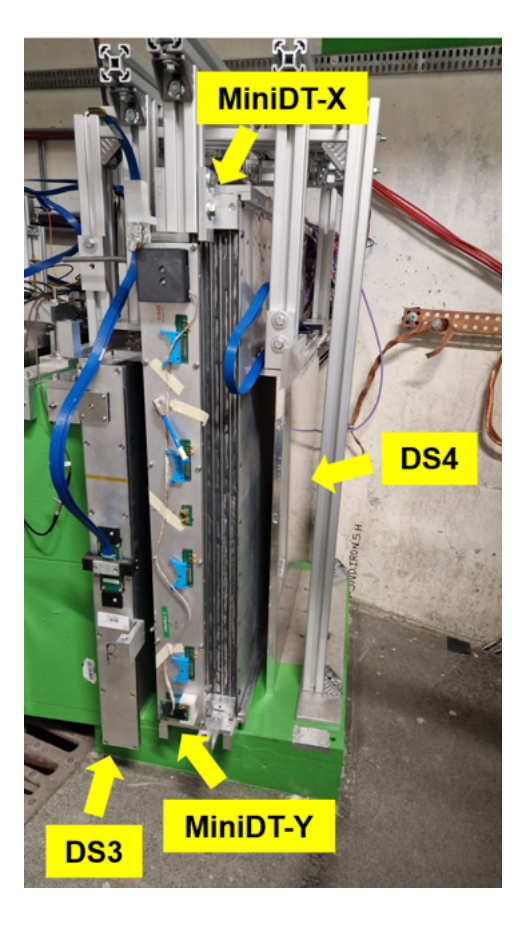


Figure 3.10: The MiniDTs and DS3-4 installed in the new mechanical support structure, as pointed by the yellow labels.

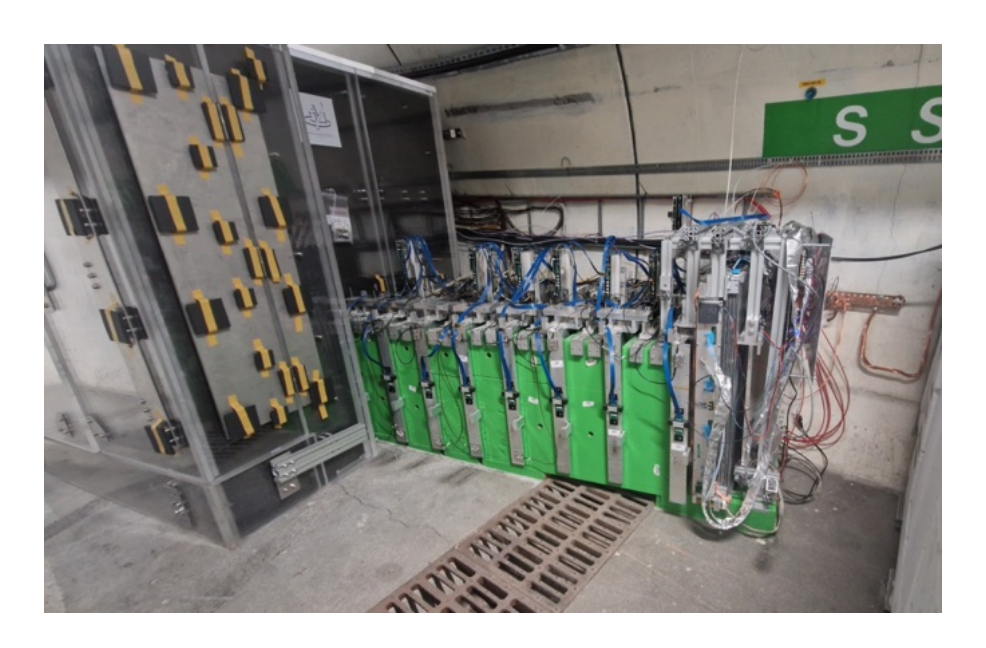


Figure 3.11: The SND@LHC experiment, with the installed MiniDTs system.

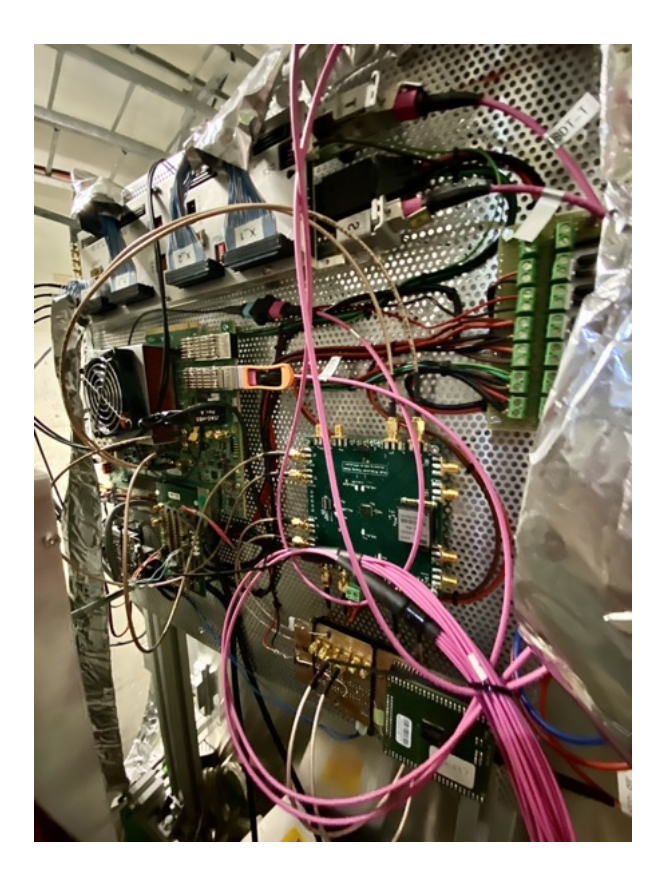


Figure 3.12: The installed electronics box, with no cover grid.

a pressure reducer <sup>1</sup>, a flowmeter and then into the copper pipe, that transports it to MiniDT Y, entering from a connection on the wall side of the detector. A link, made out of a plastic pipe, connects MiniDT Y (tunnel side connector) to MiniDT X (floor side connector), see Figure 3.15. Then, the return flux comes out from the top of MiniDT X and back to the gas bottle position, through a plastic pipe. At the end of this tube there is a bubbler, filled partially with paraffin oil (Figure 3.16), with a small opening to let the gas escape. The presence of bubbles in the bubbler checks for the correct functioning of the gas circuit and its tightness; their absence calls out to a gas leak, either in the pipes, their junctions or the detectors themselves.

The gas mixture flow can be regulated by a flowmeter, in Figure 3.17. The operative flux is  $\sim 2$  L/h, but the first days of the installation the MiniDTs were fluxed at  $\sim 10$  L/h to quikly get rid of air.

<sup>&</sup>lt;sup>1</sup>The pressure reducer role is to transform the variable pressure of the gas mixture, coming out of the gas bottle, into a costant and low pressure ( $\sim 0.1$  bar above the atmospheric pressure). This value is just enough to push the gas in the MiniDT circuit, avoiding too high pressure values that would damage the detectors, in the presence of a completely loose flowmeter.

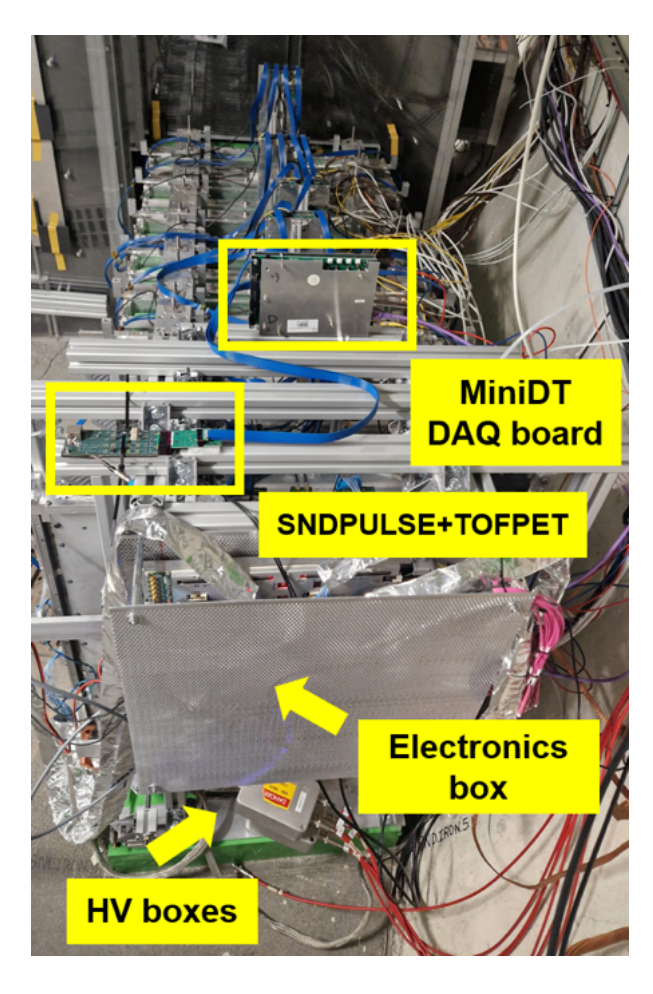


Figure 3.13: The installed electronics box, with the cover grid on. Outside of the box, the HV distribution boxes, the SNDPULSE, the TOFPET board and the MiniDT DAQ board (yellow labels).



Figure 3.14: The gas bottle for the MiniDT gas circuit, fixed to the UJ18 wall. The copper tube transports the gas mixture to the MiniDT Y, while the plastic tube is the return flux, that ends in the gas bubbler.



Figure 3.15: Circled in yellow, the gas link between the two MiniDTs: the gas mixture flows from the tunnel-side of MiniDT Y to the floor-side of MiniDT X.



Figure 3.16: The MiniDTs gas bubbler, filled partially with paraffin oil. It is connected to the gas return flux from the MiniDTs. If bubbles are present, the gas circuit is tight, with no major leaks.



Figure 3.17: The gas bottle flowmeter. It regulates the gas flux entity: the numeric scale is in L/h units.

# 3.3 Integration in the SND@LHC DAQ system

The MiniDTs integration in the SND@LHC online system is described in the following. MiniDTs monitoring, data taking procedures and control for HV/LV values are all part of the same readout system as the experiment, described in Section 1.3.

## 3.3.1 Integration in the SND@LHC ECS

The SND@LHC and MiniDT DAQ systems operate independently, with synchronization relying solely on the event timestamping, which is time-aligned by means of TTC signals. At the start of the run and during the initialization phase, all TTCrx modules receive the SoR signal that establishes a "global" timestamp reference. Data events are aligned using the timestamps, but there is no direct correlation between the event numbers of the two readout systems. Both data streams will be stored in local servers during the run, to be transferred only later on the storage area reserved to SND@LHC on CERN EOS storage system.

The ECS GUI was modified to account for the MiniDTs presence, monitoring hit and TPG rates and HV/LV power controls (for a detailed explanation see Section 3.3.2 below). The MiniDT ECS panel is shown in Figure 3.18.

Plane X Plane	Y Readout						
Status	Run	ning	Last U	lpdate	Sat 26 Ap	Configure	
Run Number	10	803 <b>T</b> pg	s X - Tot	52 -		15   0.888235	Hz
RunTime		□[] Tpg	s Y - Tot	- 55		1174677.0 58	Hz
Mon Time	30	. □Ч Hits		63523		373.6647	Hz
Total SOR		Erro	rs	0			
TTC Ready	• тт	C Unlock (	п	C Unlock T	•	Misaligned SOR	•
LV Channel	VMon	IMon	Voltage I0	Current Limit	Power	Status - Description	
mdt_bb	5.08 V	0.356 A	5.07 V	2.50 A	ON O	Beaglebone	
mdt_vcu	12.41 V	2.312 A	12.40 V	3.50 A	ON O	Daq Board VCU118	
mdt_obdt3	3.60 V	2.768 A	3.60 V	3.60 A	ON O	OBDT V1	
mdt_obdt5	5.15 V	0.403 A	5.15 V	2.50 A	ON O	OBDT V2	
mdt_ttc	6.00 V	0.043 A	6.00 V	2.50 A	ON	TTCrq Board	
mdt_fe	12.16 V	0.614 A	12.15 V	2.50 A	ON	CDC FE - PLL	D. All ON
							Pwr All ON

**Figure 3.18:** MiniDT panel in the SND@LHC ECS GUI. The panel allows hit and TPG rates monitoring and power controls for MiniDT HVs and LVs.

The MiniDTs routine at the start of run is structured as follows:

- The MiniDT readout script creates a folder, where the data will be saved, with the same run number as the SND@LHC run;
- The MiniDT electronics is configured and is in "wait for Start Of Run B-Go" mode;
- The MiniDT DAQ script is started but no data is flowing, the MiniDT monitoring is started as well;
- The ECS runs the start procedure, including the transmission of the SoR B-Go, which simoultaneously resets the timestamping counters in all systems. SND@LHC and the MiniDTs start the data taking, writing separate data streams. In the output folder, a MiniDT log file is produced as well. It contains the run start and stop timestamps and it reports possible readout problems, e.g. a warning when readout buffers reach > 50 % occupancy or a data loss error once they are full;
- Once the run is finished, stop data taking for both SND@LHC and MiniDTs.

The MiniDT data taking has a 20 ms polling interval to collect hits and TPGs, from the VCU118 FPGA buffers, through its Ethernet connection. All these operations are encoded in Python scripts on the MiniDT server and executed the SND@LHC ECS via SSH access on the server. An additional Python script reads firmware registers related to the status of the clock and the synchronisation logic, together with TPGs rate every 30 ms and writes them to in an output monitoring-{run\_number}.csv file. Another script, at the end of the run, plots their distribution and saves it in a remote folder. Between runs, the SND@LHC ECS may establish an SSH connection with the MiniDT BeagleBone Black, where other Python scripts are kept, for hardware-specific operations: one script, based on the OpenFPGAloader software [27], loads the firmware on the VCU118; another script controls the MiniDT FE thresholds configuration - the MiniDTs FE is linked to the I2C interface of the BeagleBone Black which is driven by built-in commands in its operating system.

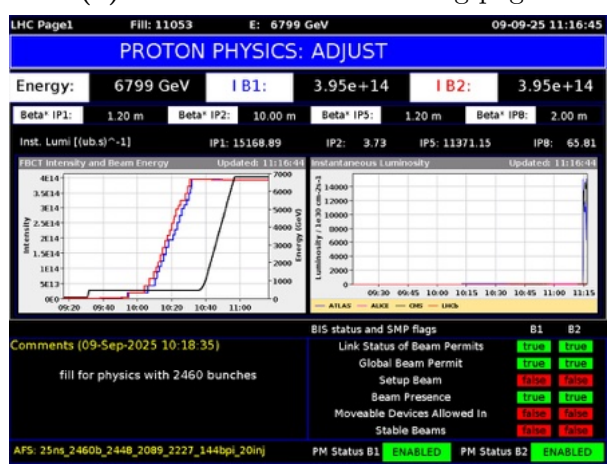
#### Online monitoring

The MiniDT monitoring logs, gathered by the SND@LHC ECS, are made public to the SND@LHC collaboration in real-time, on the experiment web page, together with the logs from all the other subparts of the detector. The MiniDT online monitoring page provide information on the SND@LHC run status (number, LHC machine and beam

mode, current integrated luminosity of the run), the hits and TPGs amount and rates since the start of the run, and the TTC signals status. Figure 3.19 and Figure 3.20 show the online monitoring during the adjust and stable beams status of the LHC machine, respectively, and the LHC Page 1 status in the same run.



(a) MiniDT online monitoring page

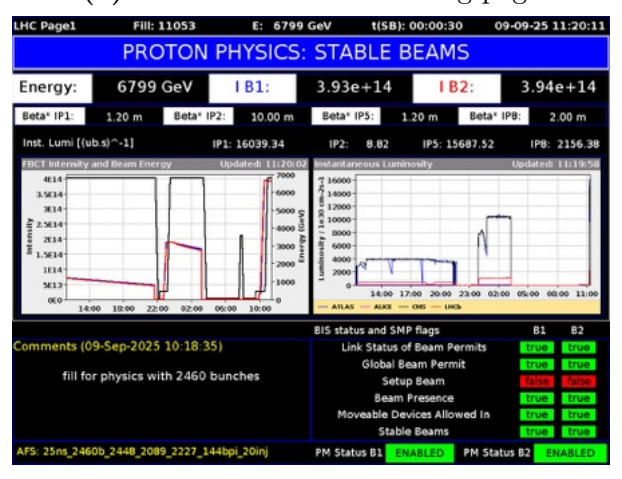


(b) LHC Page 1

Figure 3.19: The MiniDT online monitoring page during the LHC beam adjust (above), and the corresponding LHC page 1 (below), showing the LHC machine status.



(a) MiniDT online monitoring page



(b) LHC Page 1

**Figure 3.20:** The MiniDT online monitoring page during the LHC stable beams (above), and the corresponding LHC page 1 (below), showing the LHC machine status.

# 3.3.2 HV/LV control and Grafana online monitor

The MiniDTs HV/LV can be controlled by the ECS GUI. The HV/LV values are fixed, and the currents associated to the MiniDT cathodes and wires can be monitored in real time from the Grafana [33] online web page for MiniDTs, see Figure 3.21 for a snaspshot during a run with colliding bunches in LHC. In the same web page, the run status and

a monitor for TTCReady, TTCUnlock, TTCUnlockT signals, together with TPGs and hits rates are provided as well.



Figure 3.21: The Grafana [33] online web page for MiniDTs, during a run with colliding bunches in LHC. In the web page, a monitor comprehensive of the currents associated to the MiniDT cathodes and wires, the run status, TTCReady, TTCUnlock, TTCUnlockT signals, and TPGs and hits rates is provided.

# 4 | MiniDTs commissioning and performance in SND@LHC

This chapter describes the MiniDTs commissioning in the SND@LHC experiment, from the first days after the installation up to September 2025.

The chapter has the following structure: Section 4.1 presents rate measurements and tracking studies performed on the first data taken with MiniDTs in SND@LHC, in cosmic rays runs; Section 4.2 illustrates the data taking with the first 2025 LHC collisions, providing an extensive overview on MiniDTs rate and efficiency measurements and describing the activities during the LHC Technical Stop; Section 4.3 shows the MiniDTs integration in the SND@LHC analysis software, sndsw; finally, Section 4.4 describes a preliminary tracking method based on the Hough Transform, still under optimization, to obtain MiniDT reconstructed tracks.

# 4.1 Commissioning with cosmic rays

Up to the start of 2025 LHC collisions in April 2025, the MiniDT data taking consisted of cosmic rays data. These runs were crucial, to test the newly installed system and its synchronization with the rest of the SND@LHC experiment.

#### 4.1.1 MiniDTs standalone runs

The first runs with the newly installed setup consisted in standalone runs of MiniDTs. They were necessary to assess the correct functioning of the chambers and of their readout system, e.g. hit and TPG rates are perfect probes for gas issues such as chamber leaks - as described before, the presence of  $O_2$  coming from the outside within the gas mixture would quench the electrons signal. Moreover, they provided a baseline value for the noise rate, that comprises cosmic rays, electronic noise, etc...

Results obtained from a data taking run just two days after the installation are shown in the following figures. Figure 4.1 shows the hits rate for each MiniDT layer. MiniDT X is noisier than MiniDT Y, as expected from the previous tests described in Section 2.3, but their rates are approximately constant throughout the whole run. At this point, the chambers had been fluxed for approximately 2 days after almost three months with no HV and a few weeks with no gas. Figure 4.2 depicts the hits rate for each MiniDT cell, in agreement with the higher hits rate in MiniDT X that was mentioned above. To compute their rates, hits where assigned a "global" timestamp on the basis of the information their stream provides (see Section 2.2.3). The hit timestamp is computed as:

$$t_{hit} = n_{OC} \times T_{OC} + O \times T_O + BX \times T_{BX} + TDC \times \frac{25}{32}$$

$$(4.1.1)$$

where  $n_{OC}$  is the number of times the internal OC counter has reset,  $T_{OC} = 524288 \times 3564/(40.0789 \times 10^6) \sim 46.6$  s is the OC counter period, O is the hit orbit number,  $T_O = 3564/(40.0789 \times 10^6) \sim 88.9 \ \mu s$  is the orbit period, BX is the hit bunch crossing number within the LHC orbit structure,  $T_{BX} = 25$  ns is the single bunch slot, TDC is the hit fine TDC value, which is multiplied by the TDC resolution (32 bit, 25 / 32 ns LSB). Overall, the total hits rate from both detectors sums up to  $\sim 500\text{-}600 \text{ Hz}$ .

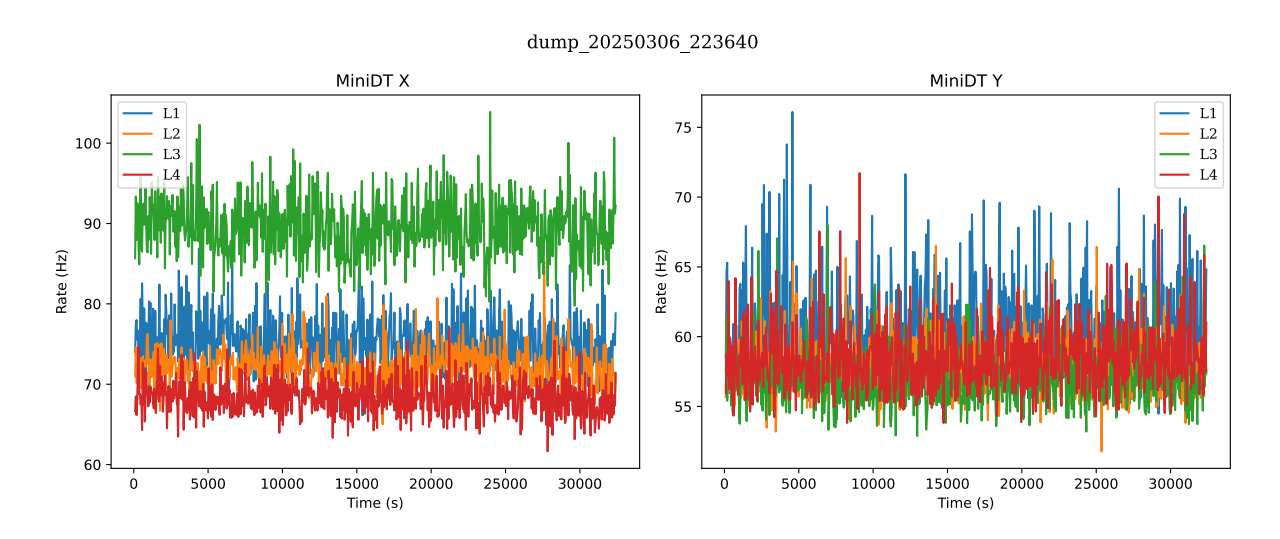


**Figure 4.1:** The hits rate in the four layers of both MiniDTs (on the left MiniDT X, on the right MiniDT Y), depicted in different colours. The hits are mainly due to noise, with a contribution from the small rate of cosmic ray muons reaching the LHC tunnel.

To perform a standalone calibration, the TPG streams were exploited to obtain the characteristic MiniDT timeboxes, already seen in Section 2.3. TPGs are necessary to

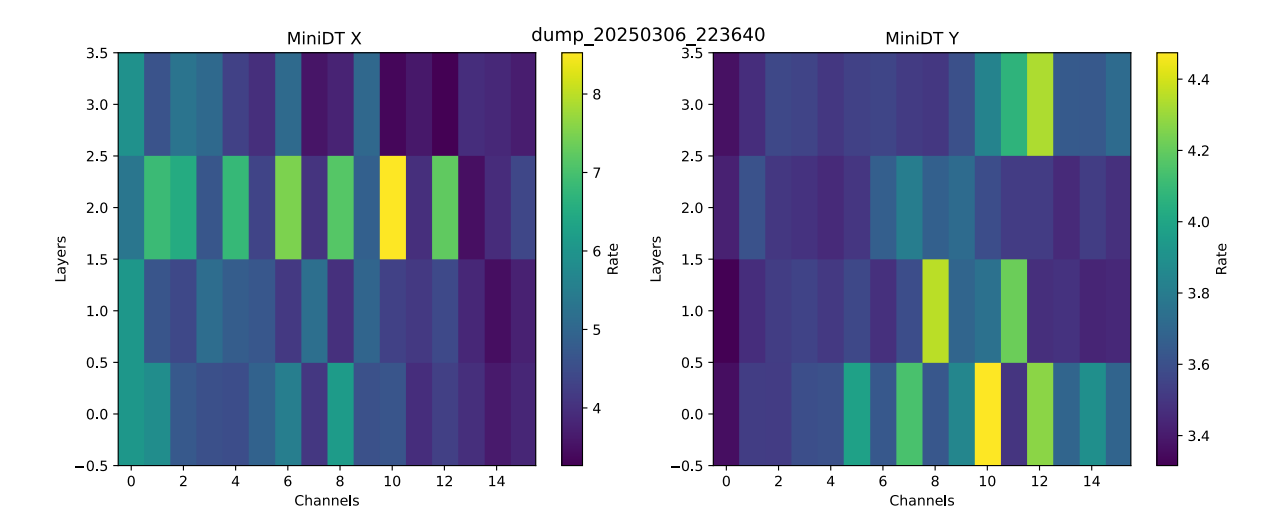


**Figure 4.2:** The hits rate in the 64 channels of both MiniDTs (on the left MiniDT X, on the right MiniDT Y), depicted in different colours. The hits are produced by cosmic rays. All channels are working correctly and no particularly noisy cells are identified.

identify actual muon tracks amongst the noise, that produce good quality TPGs, whose  $t_0$  can be used as reference, and associated hits: in this way, timeboxes can be produced. In Figure 4.3, the plots depict for each detector the time difference between the hit timestamps and the TPG timestamps in several runs. The TPGs "global" timestamp assignment is similar to the one for hits described above and computed as:

$$t_{TPG} = n_{OC} \times T_{OC} + O \times T_O + t_0 \times \frac{25}{32}$$
 (4.1.2)

where  $n_{OC}$ ,  $T_{OC}$ , O and  $T_O$  where defined above and  $t_0$  is the TPG time.

To obtain the timeboxes in Figure 4.3, the TPGs selection proceeded firstly with the requirement of one H-quality (4-hits) TPG in any of the two chambers and then for a matching TPG in the other chamber, in the [-75, +75] ns time window. This passage was necessary not only to be sure that an actual muon had crossed both MiniDTs, but to have a low-noise, good timing reference as well. The time window was chosen to be wide enough to find at least one match in the chambers, but narrow enough to keep a low mismatching rate. The time difference that is shown in the pictures is the one between the hits belonging to the TPG and the  $t_0$  of their H-quality TPG. The TPG  $t_0$  has the same function as the scintillation time signal in Section 2.3.1 and Section 2.3.2. The timebox have the expected shape, characterized by a peak region followed by the drift region, with an overall  $\sim 400$  ns width.

Below, in Figure 4.4, the event display of a cosmic ray in a simplified MiniDTs view,

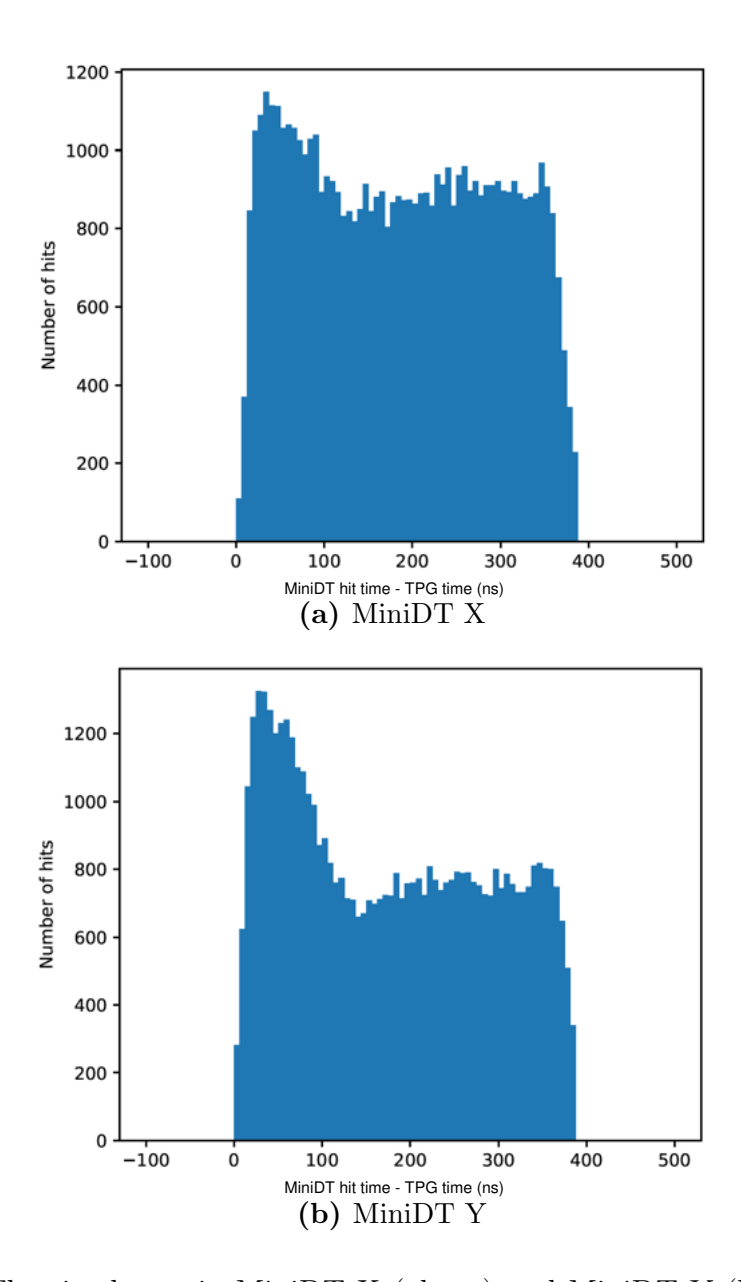


**Figure 4.3:** The timeboxes in MiniDT X (above) and MiniDT Y (below). On the x-axis, the time difference between the hits timestamps and the TPG time  $(t_0)$  they belong to.

with labels that signal the detectors placement in the SND@LHC experiment. The channels with one hit are represented by highlighted tubes. From the event topology, it can be affirmed that these are real muons crossing the detectors.

Run: dump\_20250306\_094734 Candidate: 3
MiniDTX: W6L1,W6L2,W6L3,W6L4
MiniDTY: W10L1,W10L2,W10L2,W9L3,W9L4

tunnel

wall

DS3

**Figure 4.4:** The passage of a cosmic ray in MiniDT X (right) and MiniDT Y (left). The highlited tubes are the channels with one hit. The yellow labels point out the MiniDTs placement and orientation in SND@LHC.

#### 4.1.2 MiniDTs-SND@LHC combined runs

Once the standalone calibration proved that the MiniDTs electronics and DAQ were working as expected, it was essential to check the consistency between MiniDT and SND@LHC events. Once again, cosmic rays runs were exploited.

At the start of each run, the MiniDT and SND@LHC DAQ systems are synchronised, by the procedure described in Section 3.3.1. To look for matching MiniDTs-SND@LHC events, after the assignment of global timestamps to MiniDT hits and TPGs, as described above, the presence of at least one H-quality TPG per chamber, within [-15, +15] ns from each other, was required. A narrow time interval can be used, thanks to the precise timing of the H-quality TPGs. The timestamp of the TPG belonging to MiniDT X was saved as the MiniDT reference timestamp. On the SND@LHC side, the event was selected only if it contained hits in both DS3 and DS4, since they are the muon tracking modules nearest to the MiniDT setup. Only those events where  $|t_{MiniDT} - t_{SND}| < 1\,\mu\text{s}$ , i.e. the absolute difference between the MiniDT timestamp and the SND@LHC timestamp was below  $1\,\mu\text{s}$  were saved. The time difference distribution is plotted in Figure 4.5. The plot clearly shows a strong and narrow peak, of about 70 ns width, centered on a specific

value, proving a consistent synchronisation between MiniDT and SND@LHC data in events generated by real muons crossing both detectors.

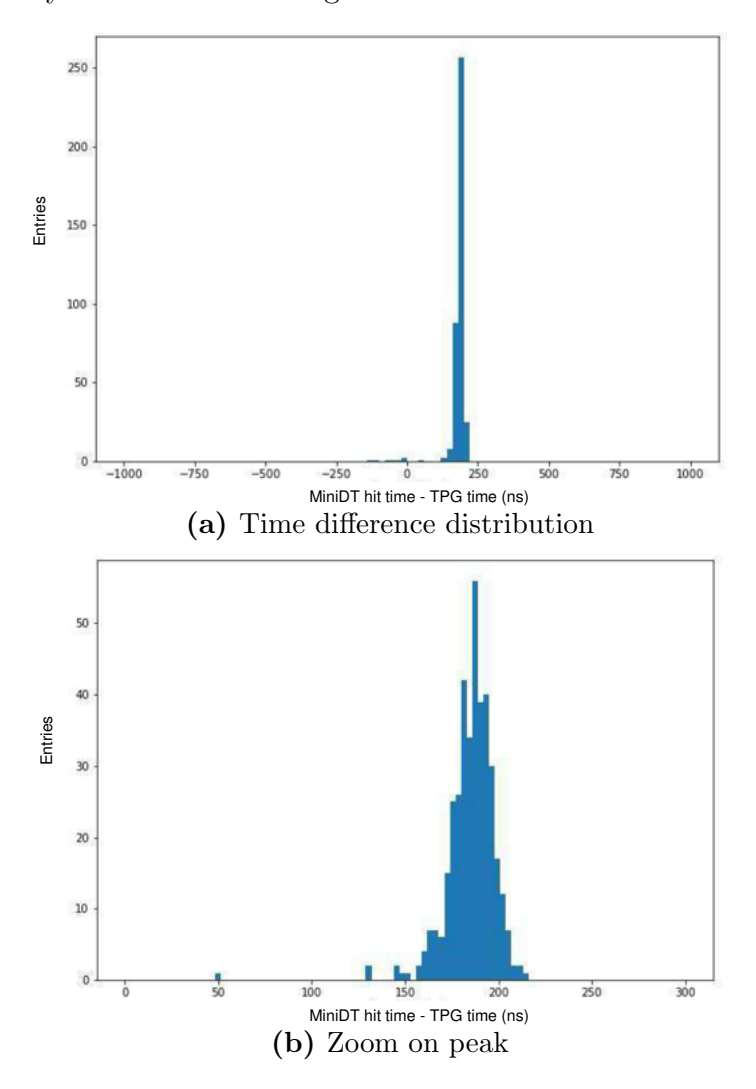
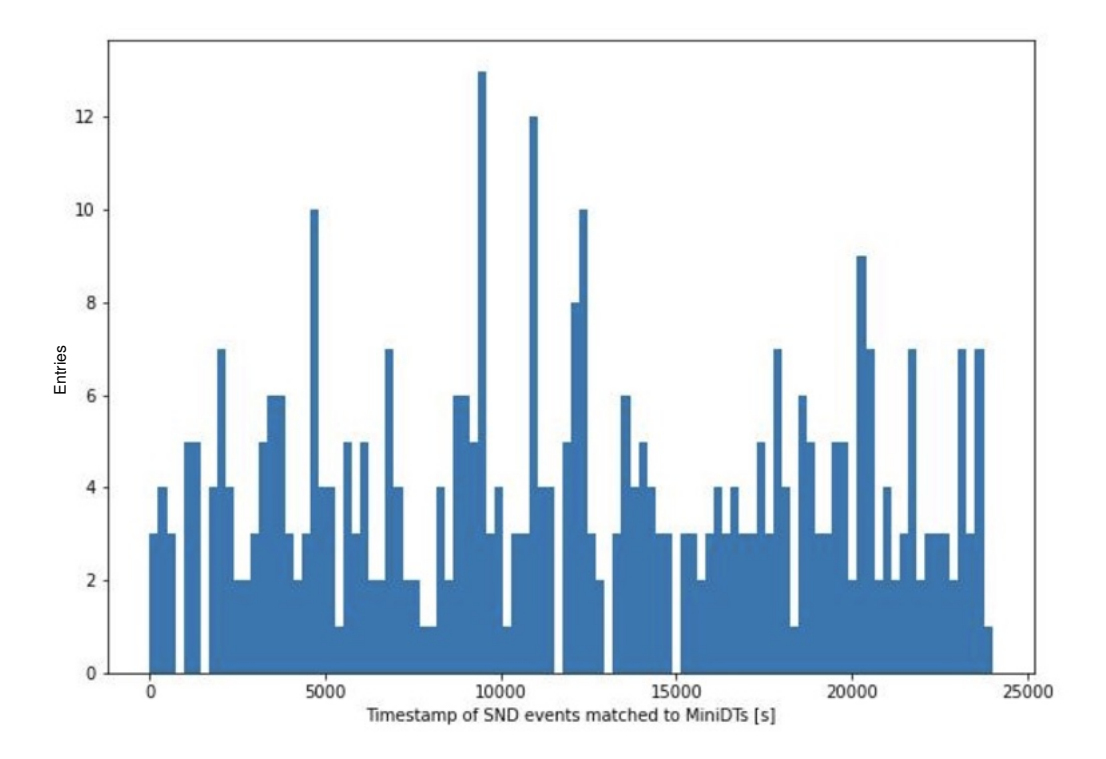


Figure 4.5: The time difference between MiniDT-SND@LHC matching events  $(|t_{MiniDT} - t_{SND}|)$  in cosmic rays runs. The selection of events is described in the text. Plotted here, the events that met the  $|t_{MiniDT} - t_{SND}| < 1 \,\mu$ s requirement (above) and a zoom view on the distribution's peak (below).

Figure 4.6 depicts the amount of matching MiniDTs events, as function of the SND@LHC events timestamp, throughout the whole run. The distribution covers the whole time range with no significative peaks or drops, showing that the probability of matching events does not change during data taking.

As a cross-check of the consistency of the previous MiniDTs-SND@LHC matching, a coarse spatial matching between MiniDT and DS events was performed. This study proceeded as follows:



**Figure 4.6:** The distribution of MiniDT events that meet the conditions described in the text, during cosmic rays runs. The distribution covers the whole time range with no significative peaks or drops, showing that the probability of matching events does not change during data taking.

- 1. Select MiniDT events with at least one H-quality TPG per chamber, within [-15, +15] ns from each other, and save the timestamp of the MiniDT X TPG;
- 2. Select hits within [-100, 500] ns around the TPG timestamp and plot their wire values distribution, as visible in Figure 4.7;
- 3. Perform MiniDT-SND@LHC event matching as above;
- 4. Plot again the MiniDT wire (cell) values distribution for hits that were matched, as visible in Figure 4.8;
- 5. Compute the normalized ratio of (1) and (2), plotted in Figure 4.9.

The resulting shape in Figure 4.9 seems to qualitatively agree with the geometrical overlap of the MiniDTs and the DS3-4 stations, as can be seen in Figure 3.1.

The SND@LHC tracks could not be exploited for these operations: since the data taking period had not started yet, there was no offline tool ready to process the data. For instance, the detector geometry had been modified by the MiniDT installation itselft, and the code had still to be changed to account for that.

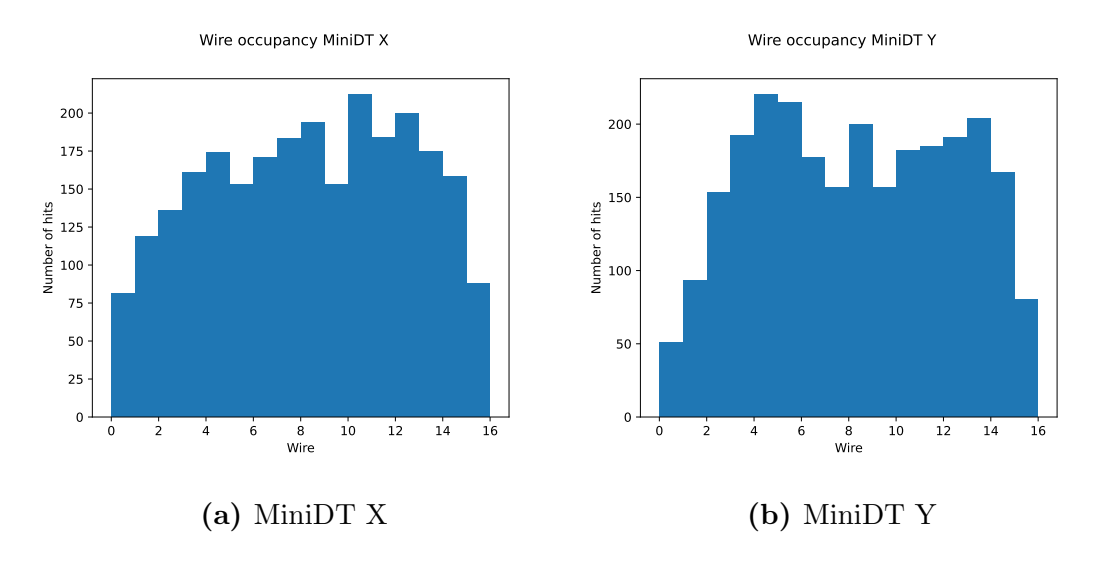


**Figure 4.7:** The distribution of wire values, for hits that are within [-100, 500] ns around the MiniDT X TPG timestamp, in events with at leasth one H-TPG in both chambers.

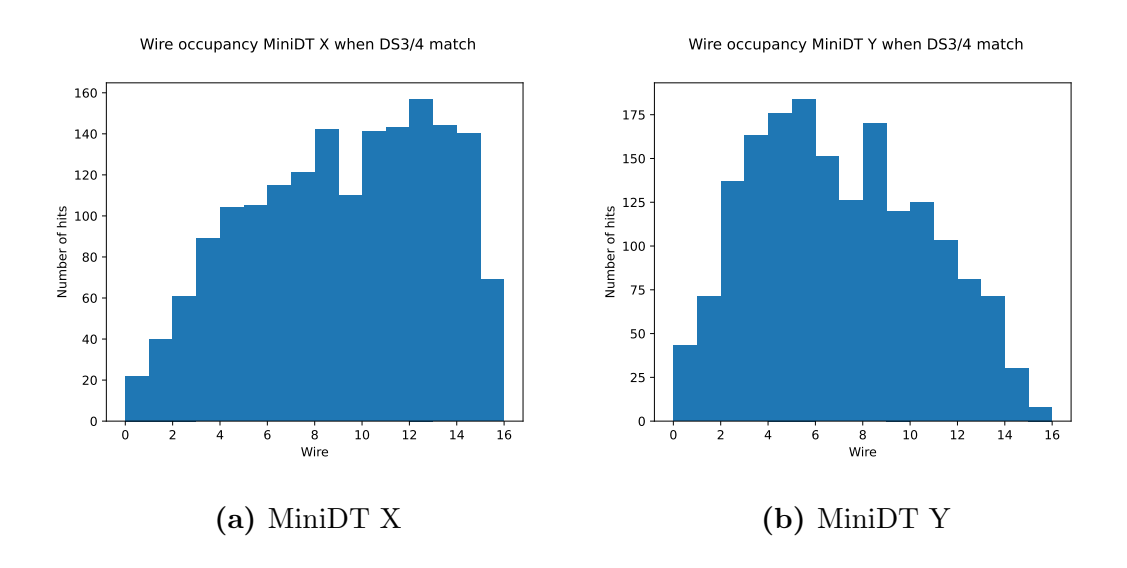


**Figure 4.8:** The distribution of wire values, for hits that are within [-100, 500] ns around the MiniDT X TPG timestamp, in events least one H-TPG in both chambers and hits in DS3-4.

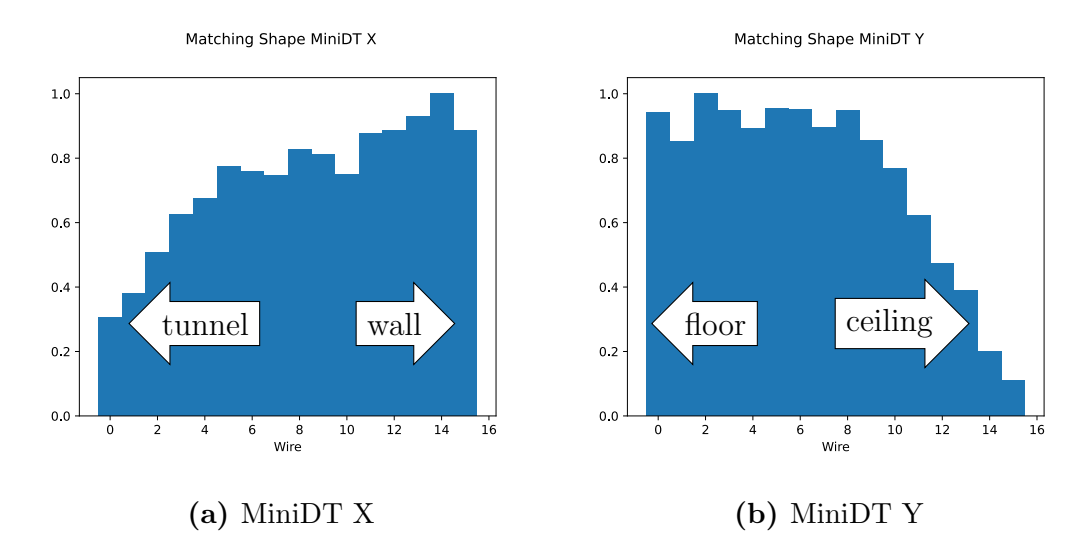


**Figure 4.9:** The ratio between the plots in Figure 4.7 and Figure 4.8 results in a shape that seems to qualitatively agree with the geometrical overlap of the MiniDTs and the DS3-4 stations, as can be seen in Figure 3.1.

## 4.1.3 Preliminary tracking studies

In the first stages of MiniDTs commissioning, some preliminar studies on MiniDT tracks reconstruction were performed. As a starting point, the most sensible choice was to perform these studies with the help of TPGs data.

The first operation was to select hits most likely belonging to the same muon track, and associate them to the TPG that generated from them in the firmware. Hits and TPGs were assigned timestamps as in Section 4.1.1, to allow temporal matching. It was required the presence of a TPG of any quality in either chamber to be matched to a H-quality in the other MiniDT, in the [-15, +15] ns range. Then, hits were selected within [-100, 500] ns around the timestamp of their TPG.

It must be noted that, to completely reconstruct a MiniDT hit in an arbitrary reference frame, it is necessary to apply Equation 4.1.3 and to know three fundamental quantities:

•  $T_{Ped}$ : a reference quantity that must be subtracted to the hit timestamp, to retrieve the correct drift time of the electrons in the cell. In these studies, each hit was subtracted  $T_{Ped} = t_0$  of the TPG of the other chamber, for an unbiased timing reference. For a complete integration of MiniDTs in SND@LHC events,  $T_{Ped}$  would derive from the SND@LHC event timestamp of the muon that generated the hits;

- $v_{drift}$ : a fixed value for the drift velocity of electrons in the cell. For these studies, it was set to  $v_{drift} = 53.5 \,\mu\text{m/s}$ ;
- Hit laterality: the hit reconstruction procedure has to solve the left-right ambiguity, *i.e.* a hit can be reconstructed either left or right of the anodic wire. This information can be deduced only once the hits belong to a reconstructed track. In these studies, the laterality was provided by TPGs, which compute it with the method described in [31].

The hits distance from the anode wire, remembering Equation 2.1.2 was computed as:

$$x = (T_{hit} - T_{ped}) \times v_{drift}, \qquad (4.1.3)$$

where  $T_{hit}$  is the MiniDT hit time. Then, this measurement was translated into a local frame of reference, whose origin was positioned in the chambers lower left angle of its cross section view. These coordinates were saved as points in a TGraph object of the **ROOT** framework and a linear fit was performed on them to find track parameters, yielding separate tracks for MiniDT X and MiniDT Y. An example event display in a MiniDT cross section view can be found in Figure 4.10, while all track quantities distributions are collected in Appendix B.



**Figure 4.10:** Event display of a cosmic ray MiniDT reconstructed track, in a cross section view of the chamber. In both MiniDTs, in a separate procedure for each chamber, the hits positions are reconstructed in a local frame of reference, whose origin is in the chamber lower left angle, as pointed by the xy axes in the plot. Then, a linear fit is performed on the hits to find the reconstructed track parameters.

# 4.2 Commissioning with LHC collisions

The MiniDT system has taken part in the 2025 LHC data taking since its start, in May 2025, collecting data that will be used in the SND@LHC physics analyses. This paragraph will show a collection of results on MiniDT rate monitoring, the fixes performed

on the MiniDT system during the LHC Technical Stop 1 (TS1), and the first efficiency measurements with MiniDT-SND@LHC combined data.

#### 4.2.1 First collisions and stable beams

As soon as the first collisions started, MiniDTs seamlessly sustained the increased rates. Figure 4.11 shows the hits from both MiniDTs as function of the BX number during a run of pp collisions on May 6th 2025, with 8 colliding bunches in LHC. The profile is characterized by eight peaks, corresponding to the colliding bunches. More importantly, when zooming in the peak of an isolated bunch, its shape distinctively follows the characteristic timebox one (see Figure 4.11, below) thus proving that the MiniDTs triggerless readout is synchronized to the LHC machine.

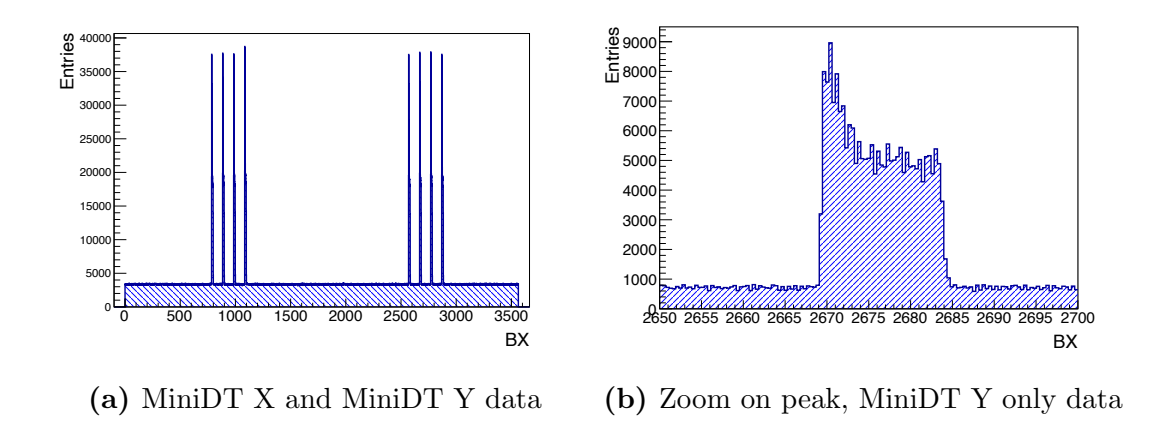


**Figure 4.11:** On the left, the hits of both MiniDTs as function of the BX number, during one of the first 2025 pp collisions runs (8 colliding bunches). The distribution profile shows eight peaks, corresponding to the colliding bunches. On the right, zoom on a peak (i.e. an isolated bunch) with MiniDT Y data only: the resulting shape is a timebox, as expected.

During each run, as anticipated in Section 3.3.1, a Python script monitors some firmware registers, TPG rates and their H-quality over L-quality ratio, and plots them at the end of the run: an example is depicted in Figure 4.12. The constant monitor of TPG rates is a probe for the MiniDTs correct working conditions, since their H / L ratio should be close to 0.6. In fact, as it is already visible in Figure 4.12, the H-quality TPG rate of MiniDT X is significantly lower than the one in MiniDT Y. This signaled the presence of a gas leak in the MiniDT system, that hugely affected the MiniDT X

performance. This issue was solved during LHC TS1, and more details can be found in Section 4.2.2. It should be noted that the TPGs rates, together with the hits rate and the MiniDTs cathodes currents, follow closely the instantaneous luminosity profile measured in ATLAS IP1. The number of muons that cross SND@LHC is proportional to it. The ATLAS luminosity measurement relies on multiple redundant luminosity detectors and algorithms [34] - the instantaneous luminosity is measured by monitoring the visible interaction rate per bunch crossing, since detector some working values, such as counting rates or electrical currents, are proportional to it and can be exploited. Luminosity measurements are public, thus making them available to the SND@LHC online system. In Figure 4.13, Figure 4.14 and Figure 4.15 the hits rate, cathodes currents and the ATLAS IP1 instantaneous luminosity, respectively, during the same run as Figure 4.12.

In fact, the hits and TPGs rates are correlated to the luminosity measured in ATLAS IP1. In Figure 4.16, a linear fit over the trend of the number of hits and TPGs in runs totaling different integrated luminosity after TS1 is plotted, showing a linear correlation. The linear fit output was that, for each nb<sup>-1</sup> of integrated luminosity,  $\sim 1.41 \times 10^{10}$  hits,  $\sim 2.68 \times 10^9$  MiniDT X TPGs,  $\sim 2.68 \times 10^9$  MiniDT Y TPGs are produced.

In Figure 4.17, a simple MiniDT hits "cross section" is depicted, simply defined as the amount of hits over nb. The distribution presents a flat profile, as expected. Here, as well, the shown results refer to runs after TS1.

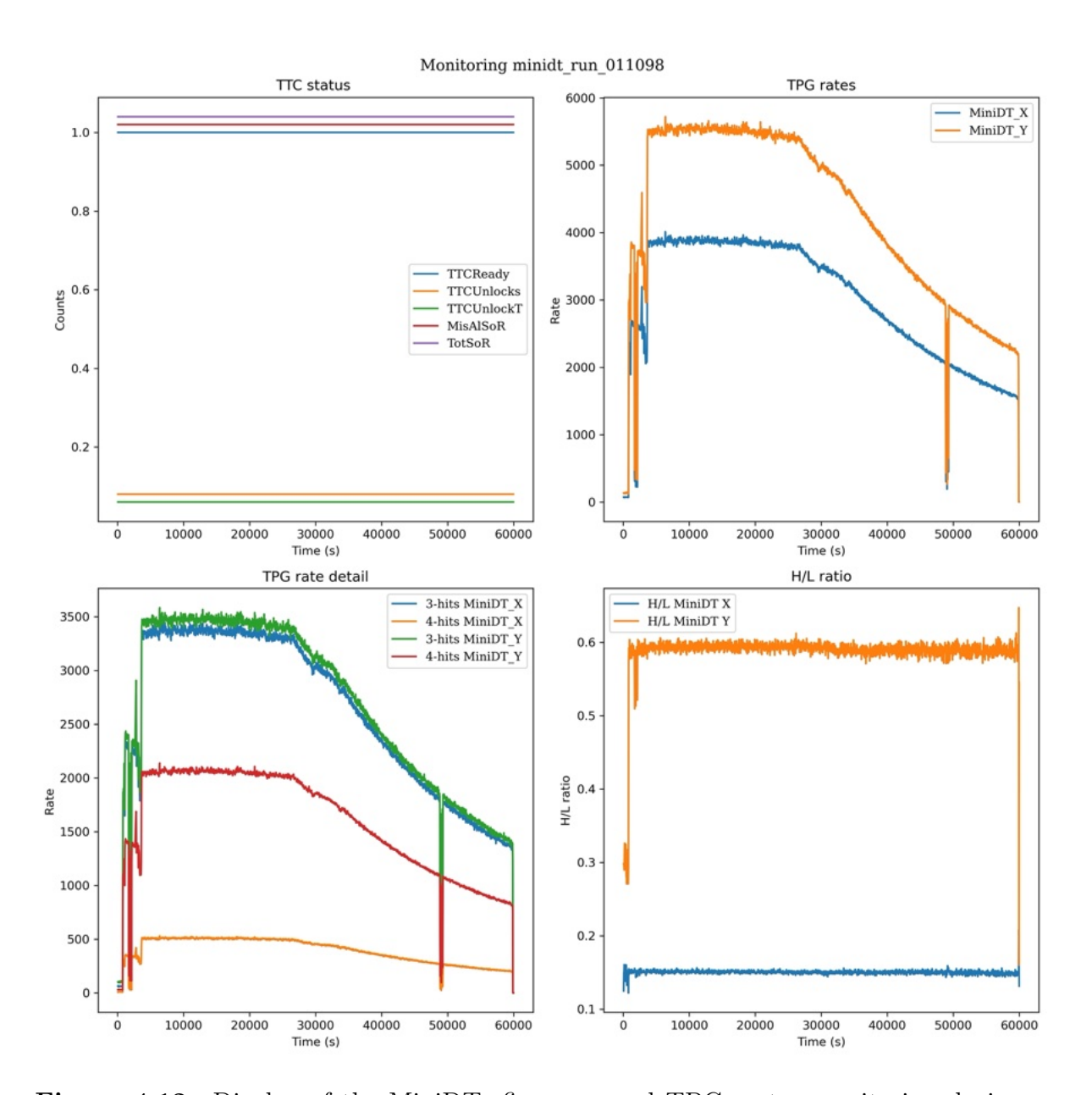


**Figure 4.12:** Display of the MiniDTs firmware and TPGs rates monitoring during a pp collisions run. The TPGs rates follow closely the ATLAS IP1 profile, visible in Figure 4.15. The great disparity between MiniDT X and MiniDT Y rates was due to a gas leak in the MiniDT system, solved during LHC TS1.

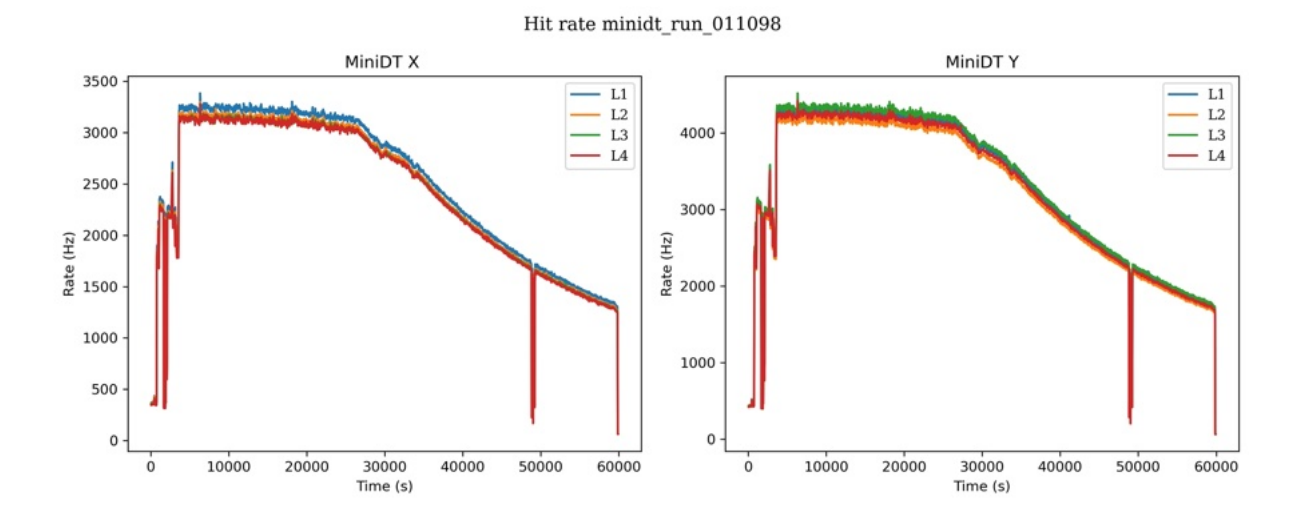


**Figure 4.13:** MiniDTs hits rates in each chamber layer, during a *pp* collisions run. The rates follow closely the ATLAS IP1 profile, visible in Figure 4.15. The disparity between MiniDT X (left) and MiniDT Y (right) rates was due to a gas leak in the MiniDT system, solved during LHC TS1.



**Figure 4.14:** MiniDTs cathodes currents during a *pp* collisions run, as visible in the Grafana online monitoring. Their currents follow closely the ATLAS IP1 profile, visible in Figure 4.15. The disparity between MiniDT X (green) and MiniDT Y (yellow) currents was due to a gas leak in the MiniDT system, solved during LHC TS1.

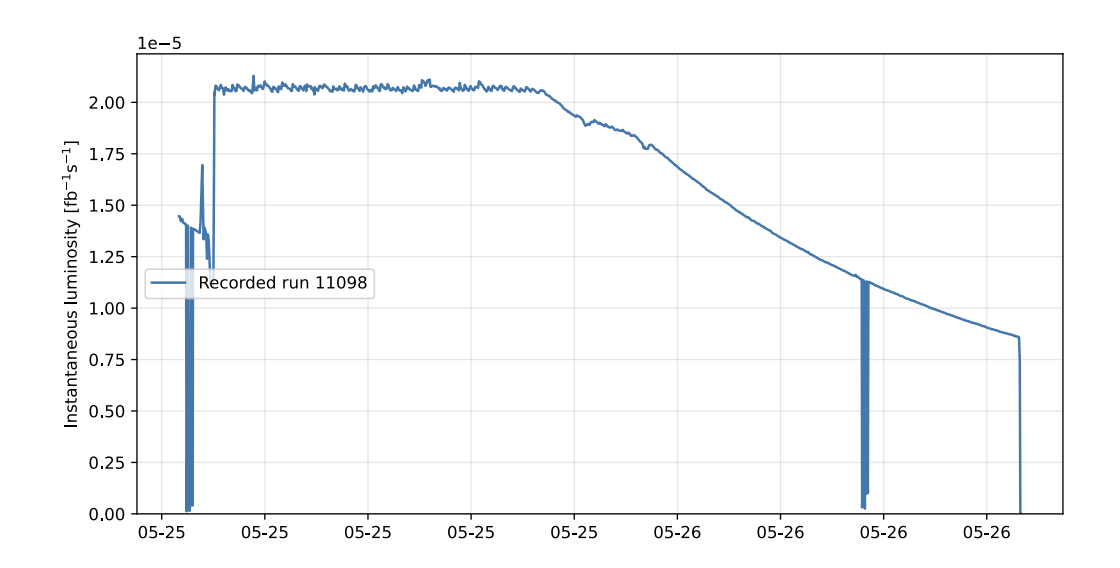


**Figure 4.15:** Instantaneous luminosity profile measured in ATLAS IP1, for the same run of data taking as Figure 4.12, Figure 4.13, Figure 4.14.

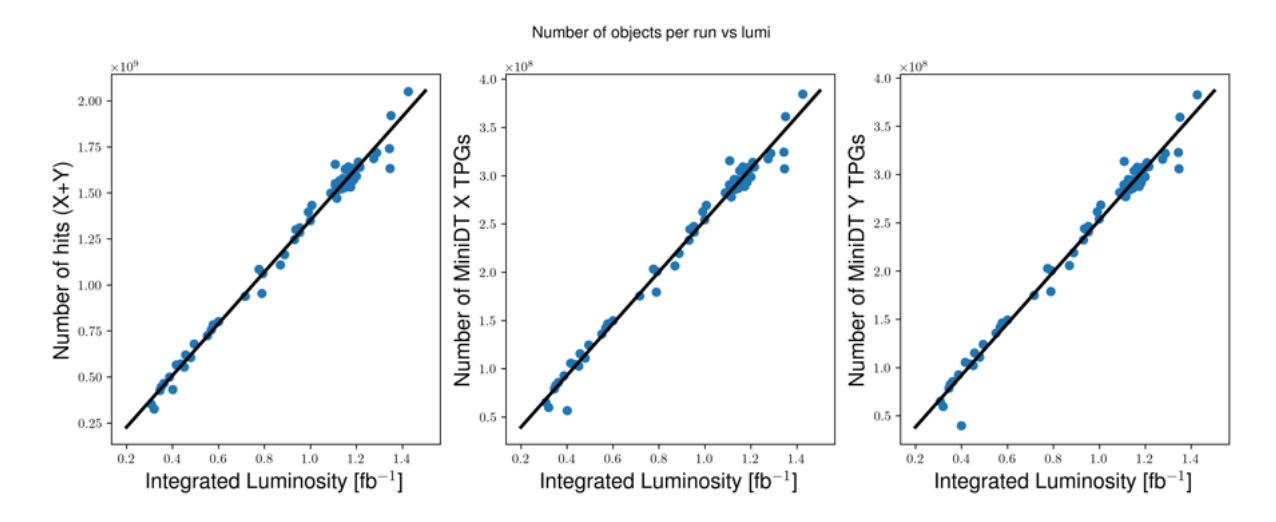


Figure 4.16: MiniDT hits and TPGs trend after TS1, over the ATLAS IP1 integrated luminosity, where almost all muons that cross SND@LHC are produced. The fit (black line) over the data points (blue dots) shows a linear correlation for all distributions.

#### MiniDT hit cross section vs time

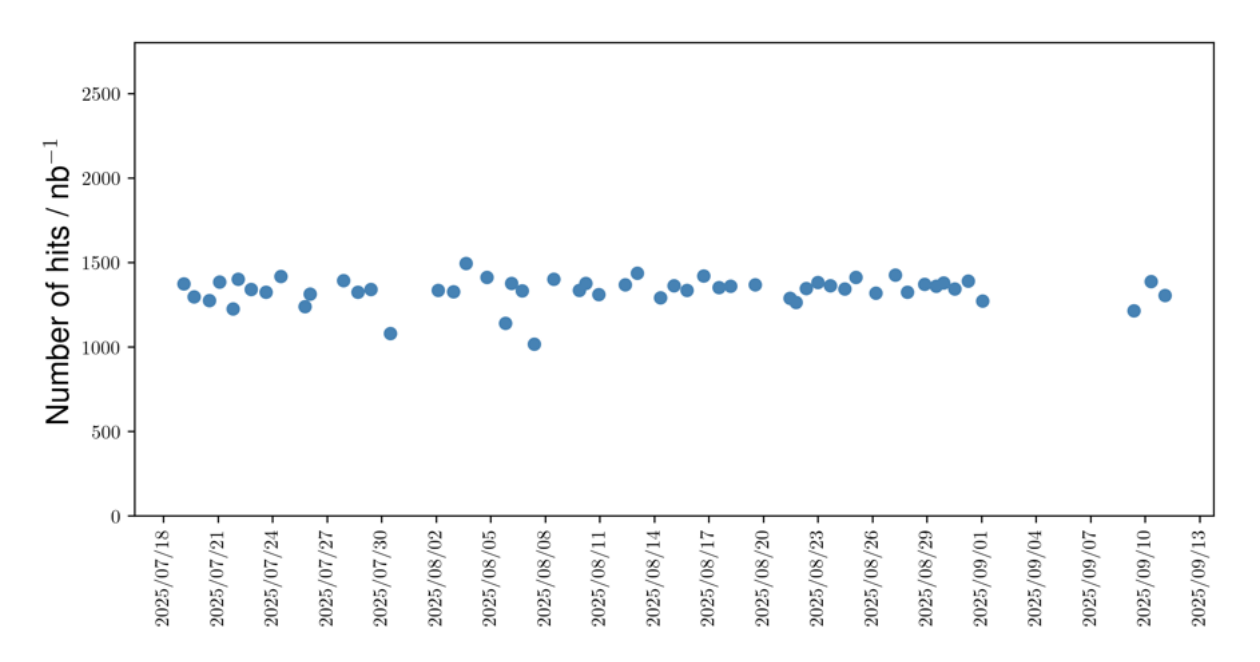


Figure 4.17: The MiniDT hits cross section after TS1, simply defined as the amount of hits over nb. The distribution shows a flat profile, as expected.

#### 4.2.2 Gas issues

The monitoring of hits and TPGs rates was essential in signaling a major gas leak in the MiniDTs system, more precisely in one of the chambers itself. In fact, by looking at Figure 4.18, it is evident a slow but steady decrease in the H-quality TPGs rate of MiniDT X, while the MiniDT Y values are approximately constant. The slow rate of decrease could not be associated to a hardware issue, concerning the HVs or LVs: therefore, the most natural explanation for such a slow process was that it was originated by a gas leak. Unfortunately, the problem was not addressed immediately, both due to the impossibility to access the TI18 tunnel shortly after the MiniDTs installation during LHC activity and due to the MiniDTs integration tests, that took place in the days corresponding to the blank spot in the graph. On April 29th 2025 a short access was granted, for a quick inspection of the gas system and the chambers. The time available was not enough to better diagnose the problem, but the gas flux was increased to 6 L/h, hoping that this was sufficient to compensate for the possible leak. The change was not enough to recover the same rate as MiniDT Y, but just to stop the loss for a brief period.

The leak entity was so important that it required another intervention on site, that happened during the LHC TS1, described below.

#### Fixes during the LHC Technical Stop 1

During LHC Technical Stop 1, from June 23rd to June 27th 2025, it was possible to access the MiniDTs system long enough to perform the necessary tests and fixes.

To fix the gas leak, it was crucial to localize it in one of the two chambers. Firstly, it was checked that the pipe conveying the gas mixture to the chambers was tight. Then, each chamber was fluxed individually, using the bubbler as probe for the gas circuit tightness. This led to the identification of MiniDT Y as the faulty chamber: in fact, the leak was on the chamber FE side, in the slit between the LVFE box and the aluminium cover and, being the Ar/CO<sub>2</sub> heavier than air, MiniDT Y was always completely full of gas, but its outlet pressure was not enough to keep MiniDT X full. To find the leaking spot in MiniDT Y, an electronic CO<sub>2</sub> detector was used, visible in Figure 4.19, where the LVFE box of MiniDT X can be seen as well. Even though the MiniDTs were perfectly gas-tight at the time of the installation, an accidental hit might have caused the LVFE board to slightly detach from the aluminium profile, therefore causing a major leak.

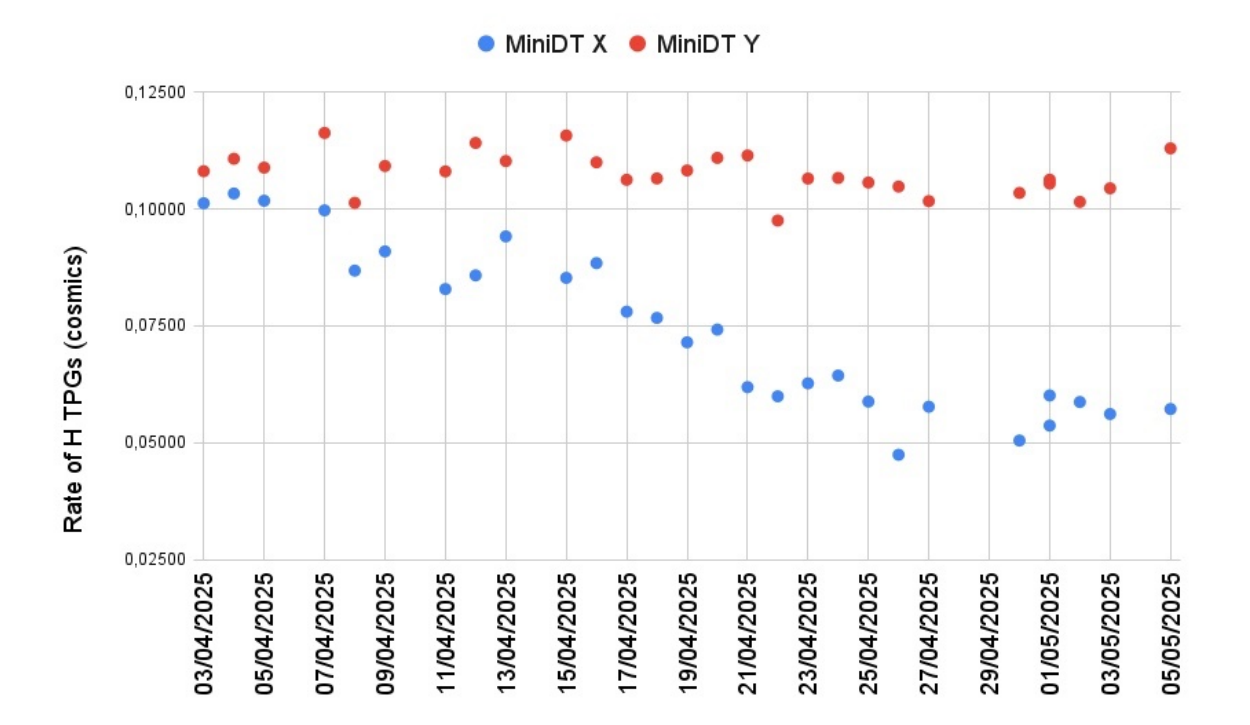


**Figure 4.18:** The H-quality TPGs rate in MiniDT X (blue) and MiniDT Y (red). The slow but steady decrease in the MiniDT X values signaled that the most probable issue in the MiniDT system was a gas leak. The blank spot in the graph is due to to the MiniDTs integration tests, that took place in those days.

The quickest and most effective solution was to replace the entire MiniDT Y with a spare one, that was brought on site from the Legnaro laboratories. In Figure 4.20, the extracted MiniDTs before substitution, being stripped of the grounding braids and slow control services, to move them to the spare chamber.

The new MiniDT system gas tightness was confirmed by the bubbler. In the same days, the gas bottle was replaced as well.

## 4.2.3 MiniDTs efficiency

Despite the gas issues, it was possible to perform some preliminary measurements on the MiniDTs efficiency with SND@LHC data, even before the MiniDT Y substitution. This procedure exploited both DS reconstructed tracks and MiniDT hits: the goal was to exploit the extrapolation of DS tracks to probe the MiniDTs for the presence of hits in individual layers. The figure summarising the chamber efficiency was chosen to be the presence of at least three different layers with hits, as this is the minimum amount of



Figure 4.19: The  $CO_2$  detector, used to find the gas leak on MiniDT Y. The black box, visible next to the detector, is the MiniDT Y LVFE box, the one that caused the leak in the MiniDTs system.

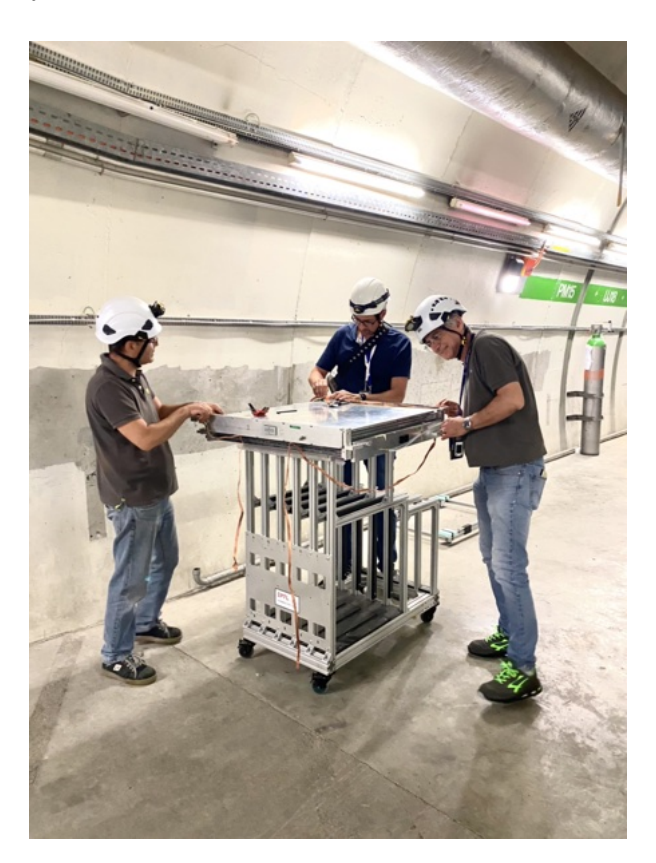


Figure 4.20: The extracted MiniDTs before the MiniDT Y substitution, being stripped of the grounding braids and slow control services, to move them to the spare chamber.

information that enables a good standalone track segment reconstruction in the chamber. In this paragraph, a study performed with data taken before the LHC TS 1 is presented.

First of all, the selection on SND@LHC events required the presence of exactly one muon reconstructed track in the DS stations, with  $\chi^2/dof \leq 5$ , and that each horizontal and vertical plane in DS 1-2-3 stations had at least one hit. The track was extrapolated to the MiniDTs nominal midplane and its xy position was filled in a 2D histogram, see Figure 4.21. The SND@LHC detector planes are not perfectly aligned to the nominal xy plane used for track extrapolation, causing some diagonal structures to appear.

Then, it was necessary to perform the SND@LHC-MiniDT events temporal matching. Using the same global timestamp assignment as Section 4.1.1, only the MiniDT hits in the [-200, 1000] ns window around the SND@LHC event timestamp were selected. The resulting distributions of MiniDT hits timestamps follows the timebox shape, as visible in Figure 4.22 - the disparity between MiniDT X and MiniDT Y timeboxes was still due to the gas leak. Given the timeboxes edges, a further selection on MiniDT hits was performed, taking only those in the [150, 650] ns window around the SND@LHC event timestamp.

Finally, the efficiency for a single MiniDT was defined as:

$$\varepsilon_N = \frac{(\text{DS track in } xy \text{ bin}) \land (\geq 3 \text{ MiniDT layers with at least one hit})}{(\text{DS track in } xy \text{ bin})}. \tag{4.2.1}$$

This definition does not require any spatial matching between the DS extrapolated tracks and the hits position within the MiniDT, however, given the small noise rate, the contribution of accidental coincidences should be negligible. Figure 4.24 shows the efficiency 2D histograms of both MiniDTs. The blue profile in the plots retraces the DS-MiniDT partial overlap, already mentioned in Section 3.1.1. Since these plots were obtained with data before the LHC TS 1, the MiniDT X efficiency is only  $\sim 70$  %, due to the gas leak. Instead, the MiniDT Y efficiency is > 95 %, agreeing with the CMS DT performance, see [35]. The modulation of values on the whole plot is due to the presence of the MiniDT I-beams that constitute the cell edges, causing some inefficiency.

The global trend of MiniDTs efficiency is summarised in Table 4.1 and depicted in Figure 4.23. As said before, the MiniDT X efficiency is lower than expected, up until TS1, when MiniDT Y was substituted. A first attempt at some efficiency recovery was performed during May 2025, by decreasing the FE digitisation thresholds from 100 mV to 50 mV. This operation yielded an increase in efficiency for both MiniDTs: MiniDT X went from  $\sim 45\%$  to  $\sim 70\%$ , while MiniDT Y went from  $\sim 93\%$  to  $\sim 97\%$ . The MiniDT

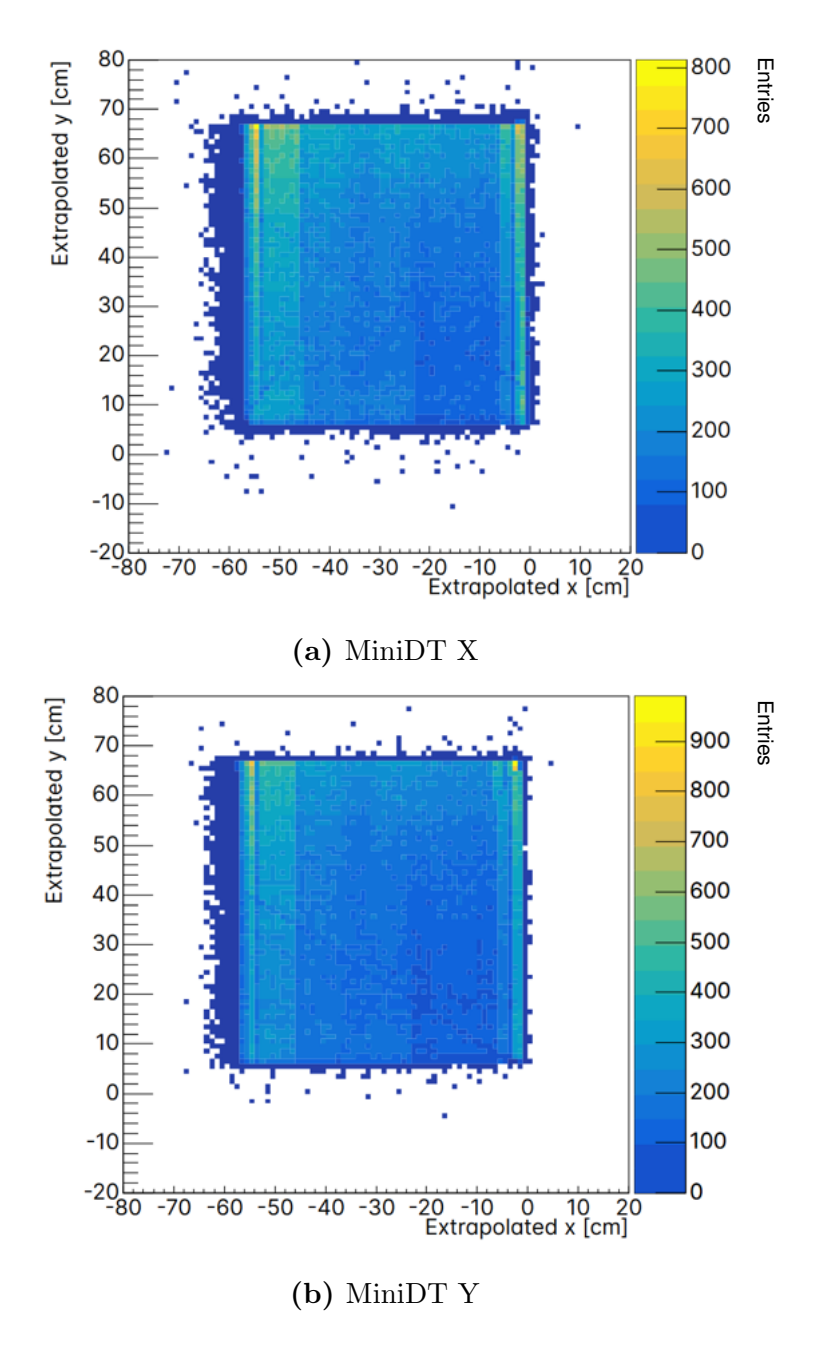


Figure 4.21: 2D histograms of xy position vaues for a DS reconstructed track extrapolated to the MiniDT X (above) and MiniDT Y (below) midplanes. The tracks have  $\chi^2/dof \leq 5$  and at least one hit in each horizontal and vertical plane in all DS stations, with the exception DS4.

efficiency, after the MiniDT Y substitution, can be seen in Figure 4.25.

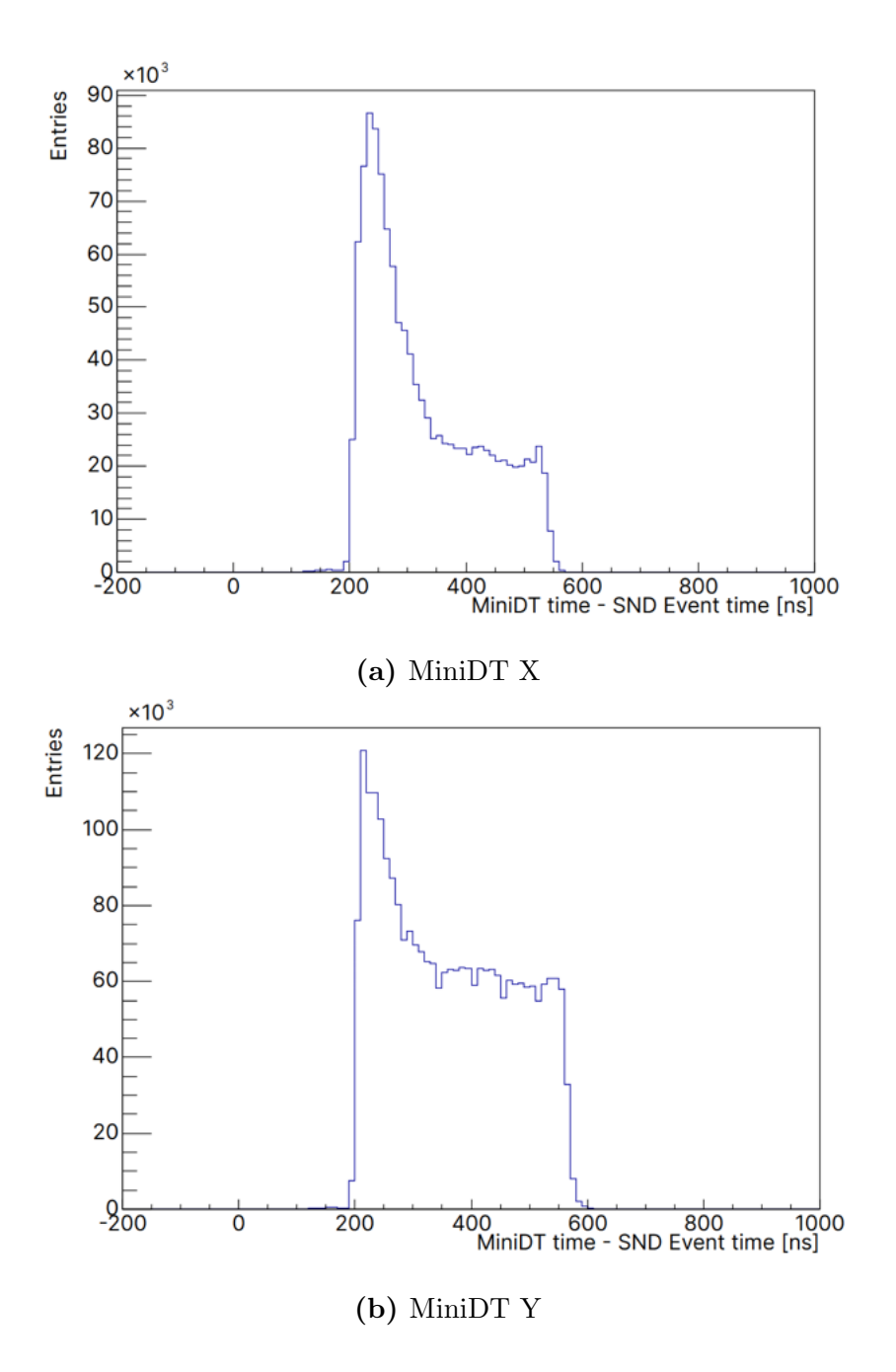
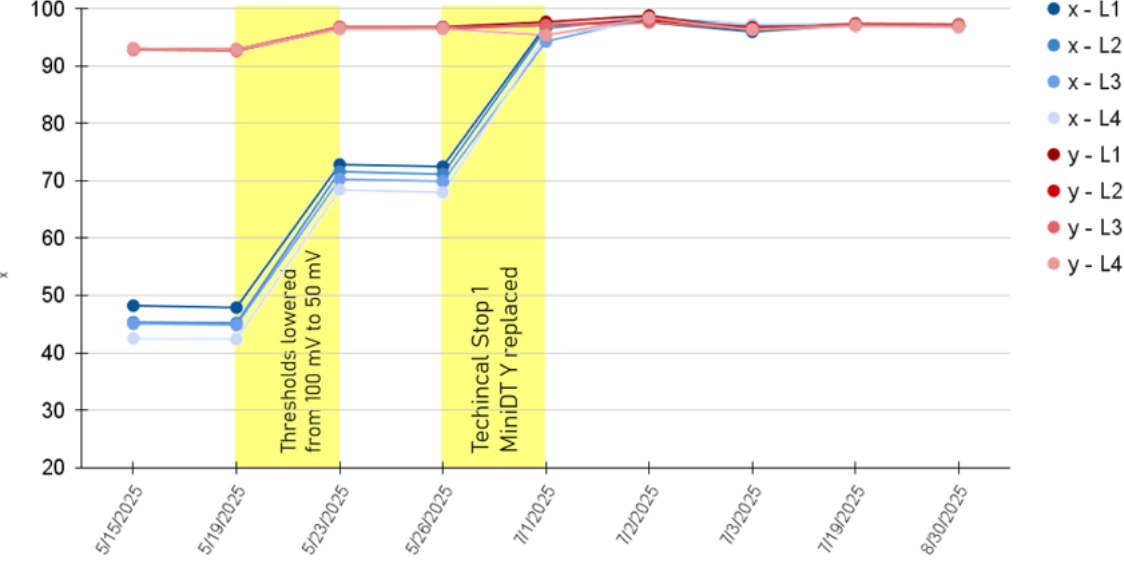


Figure 4.22: Distribution of MiniDT hits whose timestamps fall into the [-200, 1000] ns window around the SND@LHC event timestamp. The resulting shape is a timebox, that fits in the [150, 650] ns window around the SND@LHC event timestamp. The disparity between MiniDT X and MiniDT Y timeboxes is due to the gas leak in the MiniDT system.

Run date	X				у			
	L1	L2	L3	L4	L1	L2	L3	L4
15/5/2025	48.22	45.33	45.07	42.50	93.08	92.88	92.91	93.11
19/5/2025	47.88	45.21	44.86	42.39	92.90	92.69	92.94	92.82
23/5/2025	72.82	71.59	70.26	68.43	96.85	96.55	96.79	96.52
26/5/2025	72.47	71.15	69.89	67.94	96.84	96.55	96.75	96.54
1/7/2025	97.14	96.57	94.29	95.43	97.70	97.13	97.13	95.40
2/7/2025	97.63	98.42	98.42	97.63	98.81	98.02	97.63	98.42
3/7/2025	95.99	97.22	97.07	97.38	96.31	96.77	96.47	96.31
19/7/2025	97.15	97.27	97.06	97.12	97.42	97.14	97.25	97
30/8/2025	96.94	97.15	96.8	97.01	97.26	96.96	97.11	96.84

**Table 4.1:** Values of MiniDT layers efficiency in several pp collisions runs. The high-lighetd rows point out the changes in MiniDTs efficiency, after the FE thresholds lowering (since May 23rd 2025 in the table dates) and the substitution of MiniDT Y (since July 1st in the table dates).





**Figure 4.23:** MiniDT layers efficiency in several *pp* collisions runs. The changes in MiniDT X efficiency are visible after the FE thresholds lowering (during May 2025) and the substitution of MiniDT Y (after the TS 1 in June).

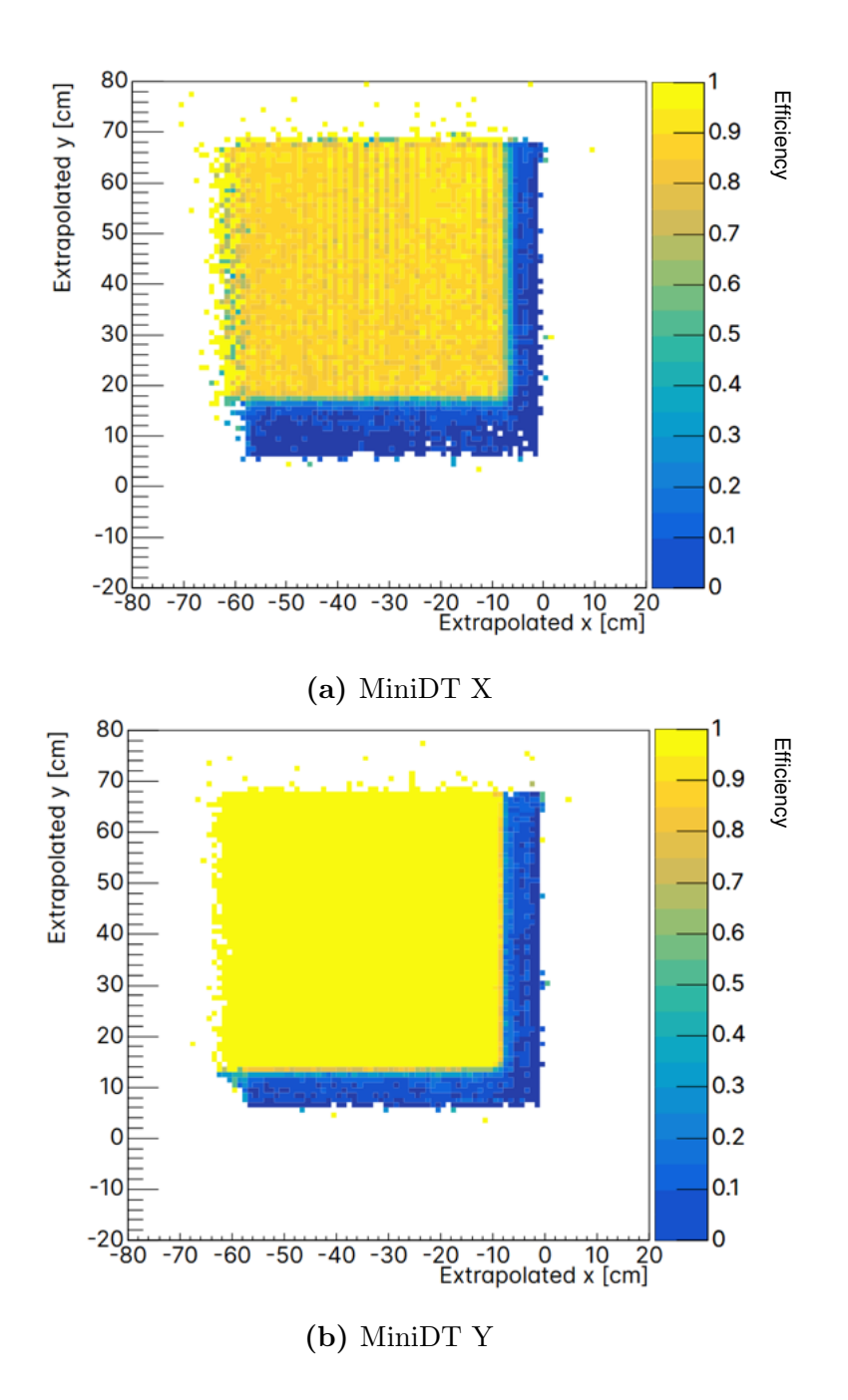
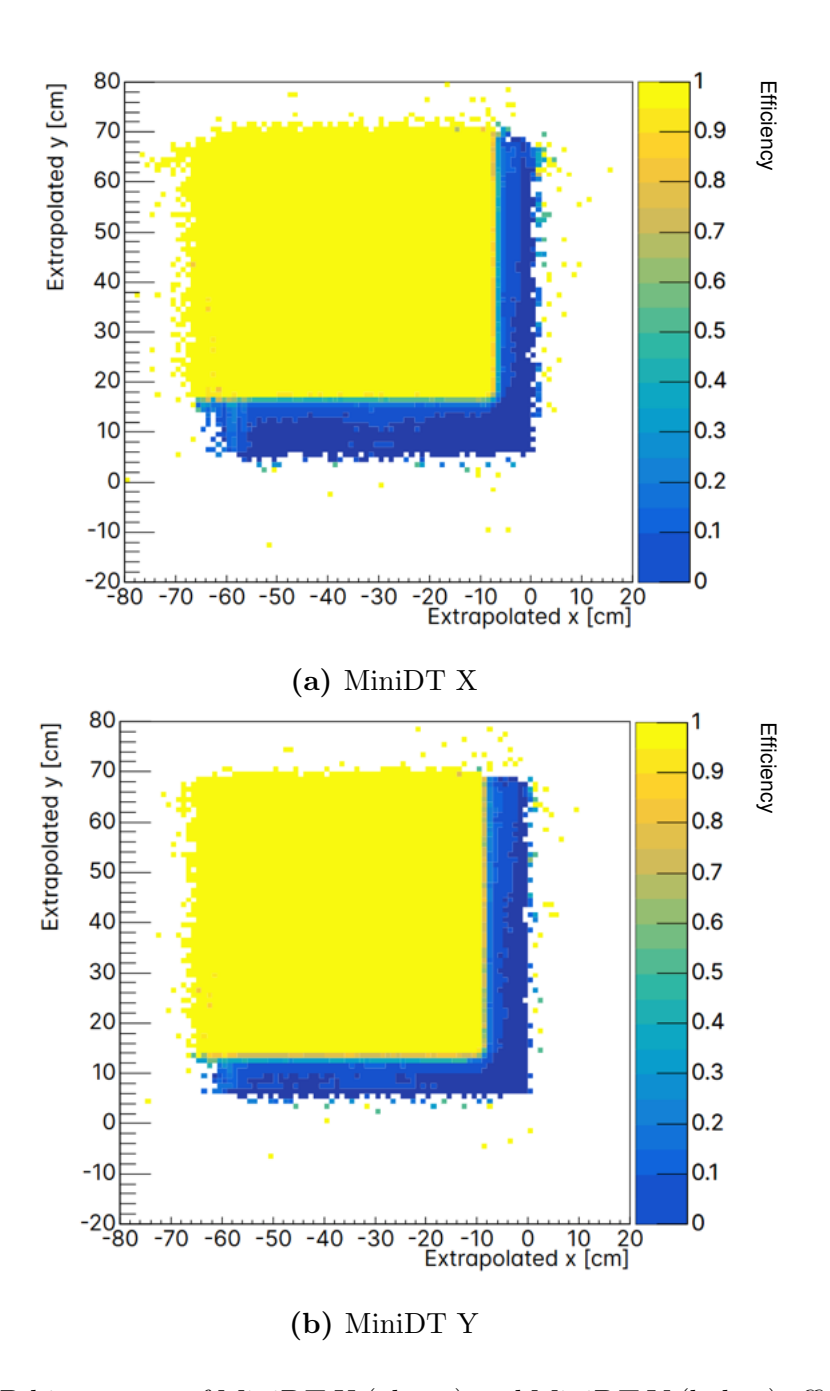


Figure 4.24: 2D histograms of MiniDT X (above) and MiniDT Y (below) efficiency. MiniDT hits in a [150, 650] ns window around the SND@LHC event timestamp were selected. Details on the efficiency computation can be found in the text. Since these plots were obtained with a run before the LHC TS 1, MiniDT X is not as efficient MiniDT Y, due to the gas leak in the MiniDT system.



**Figure 4.25:** 2D histograms of MiniDT X (above) and MiniDT Y (below) efficiency after the Technical Stop and the MiniDT Y substitution. Details on the efficiency computation can be found in the text. These plots were obtained with a run post-LHC TS 1 - MiniDT X is as efficient MiniDT Y, thanks to the MiniDT Y substitution.

# 4.3 MiniDTs offline integration in sndsw

The integration of MiniDTs in sndsw, the SND@LHC official software tool, presented in Section 1.4 is a necessary step to make their data available to the entire SND@LHC collaboration for Physics analyses.

The parts that were mostly involved in the MiniDTs integration are /shiplhc, /sndFairTasks and /geometry.

## 4.3.1 Classes for MiniDTs geometry and hits

The MiniDTs integration in sndsw required the definition of classes, for the Drift Tube detector, point and hit. An additional class was defined for the MiniDT raw data conversion, since the MiniDT readout is separate from the rest of SND@LHC and, as described in Section 1.4.1, the raw data conversion is an essential task performed centrally by the SND@LHC computing team. These classes are still under implementation, therefore they are present only as a beta version on the miniDT\_in\_SND branch in [11], where some features are not published yet.

The Drift Tube class is declared in the /shiplhc/DriftTube.h header file and defined in /shiplhc/DriftTube.cxx. It inherits from the FairDetector [12] class, and it contains members method to define the geometry and for MC simulations. The MiniDT geometry parameters, *i.e.* the detector materials and sizes, are defined in the geometry/media.geo and geometry/sndLHC\_TI18geom\_config.py files.

The Drift Tube hit class is declared in the /shiplhc/DriftTubeHit.h header file and defined in /shiplhc/DriftTubeHit.cxx. It inherits from the Sndlhchit class [11], and it contains members method to define the hit's position and timestamp.

An additional class for the Drif Tube point, declared in the /shiplhc/DriftTubePoint. h header file and defined in /shiplhc/DriftTubePoint.cxx is used in Monte Carlo simulations.

Finally, a dedicated FairTask [12] is defined for the MiniDT data conversion, to make MiniDT hits format compatible with the sndsw standard. Its class is declared in the sndFairtasks/ConvDriftTubeRawData.h header file and defined in sndFairtasks/ConvDriftTubeRawData.cxx. The /shiplhc/run\_DTconv.py macro calls the ConvDriftTubeRawData object and runs the conversion itself. The procedure will be thouroughly explained in the next section.

The main goal of the MiniDT integration in sndsw is to provide its users of MiniDT converted hits, at the stage of converted data in Figure 1.11, that can be exploited for track reconstruction and physics analysis.

## 4.3.2 MiniDT-SND@LHC offline event matching

The main problem in MiniDT-SND@LHC event matching is the great disparity between the SND@LHC online event builder, which groups together detector hits that are within 25 ns, and the MiniDT maximum drift time, that amounts to 400 ns, as anticipated in Section 2.3.3. The method to perform MiniDT-SND@LHC event matching proceeds through an offline procedure with sndsw, using the /shiplhc/run\_DTconv.py macro. To do so, in the ConvDriftTubeRawData task, the first step consists of the parallel scrolling of SND@LHC (converted) data files and MiniDT data files. For this scope, the MiniDT data will have already undergone a preliminary conversion from binary to ROOT files: each of them contains a single TTree, where each entry corresponds to a MiniDT hit with an assigned timestamp (as in Section 4.1.1) and all information enclosed in the hit binary data format (Section 2.2.3). For each SND@LHC event, all hits that are within [-200, 1000] ns of the SND@LHC timestamp are assigned to that event and stored in an output TTree in a new ROOT file with the same event numbering as the SND@LHC data. In this way, the synchronisation between the two separate streams of data is ensured.

To check the correctness of the procedure, it was tested on  $\sim 10^5$  events of a SND@LHC run. By plotting the time difference between the MiniDT hits and the SND@LHC they have been assigned to, the resulting shape is the one of a timebox, as expected, visible in Figure 4.26. The tail of events at the left of the distribution is populated by some spurious events, due to the loose timing window for the event matching, necessary not to reject any useful hit. The timeboxes do not appear as neat as the ones in Figure 4.22, since here MiniDT hits are searched in all SND@LHC events, without any selection based on muon tracking, thus adding a contribution of accidental coincidences between MiniDT hits and SND@LHC events that do not contain any muon.

### 4.4 MiniDTs track reconstruction

In this chapter, Section 4.1.3 has already presented a tracking reconstruction method with MiniDT hits. Nevertheless, that method cannot scale up enough to meet the

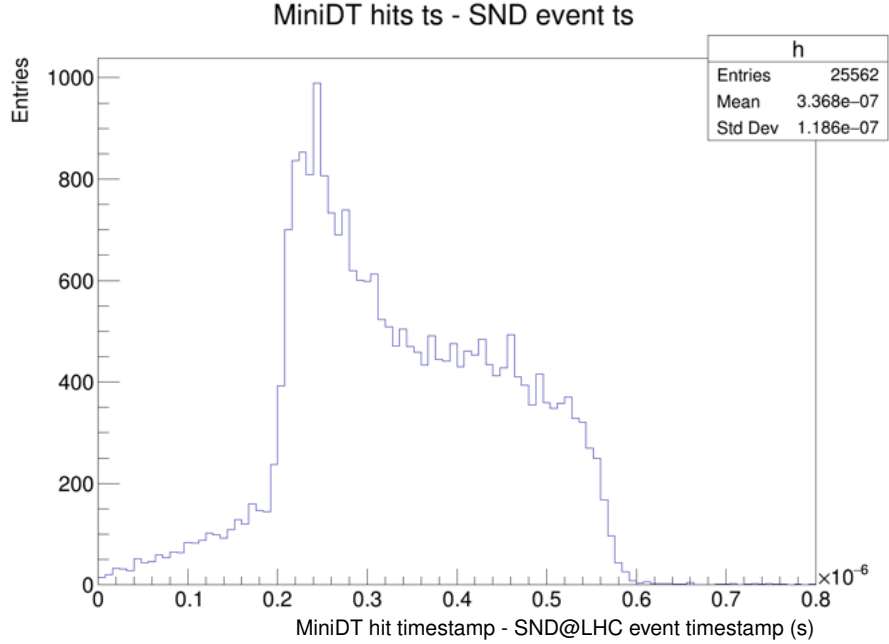


Figure 4.26: Hits timebox resulting from MiniDT-SND@LHC offline event matching with sndsw performed on  $\sim 10^5$  events of a SND@LHC run. The selected MiniDT hits are within [-200, 1000] ns of the SND@LHC event timestamp. The timeboxes do not appear as neat as the ones in Figure 4.22, since MiniDT hits are searched in each SND@LHC event.

requirements of muon tracking throughout a whole SND@LHC run, mainly due to its employment of TPGs, which will not become part of the definitive data. In fact, TPGs are a useful tool for monitoring and the first stages of the MiniDT tracking method implementation, but their production is driven by a firmware designed for the CMS DTs. This firmware cannot be edited to meet the MiniDT setup requirements, both concerning the reference frame of tracks and calibration constants. Therefore, to achieve the best performance available, a suited tracking method has to be developed for the MiniDT case, both to compute MiniDT standalone tracks, and combined tracking with the rest of SND@LHC.

As discussed in Section 4.1.3, the TPGs are a useful tool to resolve the hit left-right ambiguity. Therefore, a suited track reconstruction method for MiniDTs should do the same: due to the ambiguity, during the reconstruction phase each real track is usually accompanied by several fake companions.

To solve the hits left-right ambiguity, it was chosen to exploit a Hough Transformbased method, described below. The specific formulation used in this context is the one in [36], that was formulated for a Level 1 Trigger application in a CMS DT-like setup. It must be noted that the Hough Transform method main goal is only to select the correct laterality for each hit and not to provide the final reconstructed track, which requires a further fitting step.

## 4.4.1 The Hough Transform for Drift Tubes detectors

The Hough Transform (HT) is a pattern recognition technique, patented in 1962 [37], originally proposed for charged track reconstruction in pictures taken at bubble chambers [36]. Being a rather demanding algorithm, it was discarded soon, but it has been then successfully applied for decades, in the field of computer vision, for the automated recognition of shapes and features.

Coming back to the application in DT chambers, the study case is the implementation of the HT for straight track detection. The effectiveness of HT algorithms and their robustness against spurious hits, ambiguities and noise in offline track reconstruction are known features [38].

The HT is based on the search for accumulations in the space of the parameters  $\mathbf{p}$  used to describe a shape  $\mathcal{C}$  [36]. Measured points  $\{\mathbf{x}_i\}$  are transformed into a bundle of curves in the parameter space, according to the shape equation  $\mathcal{C}(\mathbf{x}, \mathbf{p}) = 0$ . Their intersection in the parameter space identifies the parameter set  $\mathbf{p}^*$ , which describes the only curve passing through the measured points in the coordinate space. The core of digital HT is an array of counters associated to a grid in the parameter space, whose granularity is tuned according to the desired efficiency and resolution. The cell in the grid with the highest number of counts (called "votes" in computer vision literature) is chosen as the one defining the best parameter set.

As the CMS DT setup in [36], the MiniDTs geometrical layout naturally points to the choice of the straight line description in a cartesian reference frame instead than normal parameters defined by Duda and Hart [39], helping to reduce the complexity of the HT, since the recurrent computation of inverse trigonometric functions, which are otherwise mandatory, is avoided.

#### The Hough Transform parameters for MiniDT tracks

As in Section 4.1.3, a local frame of reference was defined, its origin being in the MiniDT lower left angle of its cross section view, visible in Figure 4.27.

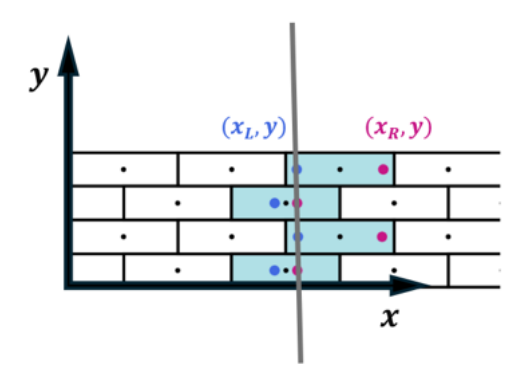


**Figure 4.27:** The local frame of reference defined for the MiniDT tracking with a Hough Transform-based method, as signaled by the *xy* axes on a cross section view of the chamber. Visible in the event display, the hits with the two possible lateralities and the muon track that generated them.

Figure 4.27 shows the cartesian convention adopted in this study. For each measured point  $(x_i, y_i)$  the coordinate  $y_i$  is fixed by the detector layer. Furthermore, each hit has to possible set of coordinates,  $(x_{i,L}, y_i)$  and  $(x_{i,R}, y_i)$ , due to left-right ambiguity. The track vector is then defined by the slope  $m = \tan \phi$ , i.e. the deviation from the normal axis to the MiniDT layers, and the intercept c = x(y = 0) (see Figure 4.28) [36]:

$$x = -m \cdot y + c. \tag{4.4.1}$$

The straight line through the *i*-th measured point meets the condition:

$$x_i = -m \cdot y_i + c \,, \tag{4.4.2}$$

which can be inverted, so that, for each measured point, we can write the equation of a straight line in the parameter space

$$c = x_i + m \cdot y_i. \tag{4.4.3}$$

The aligned points, belonging to the real track, are mapped into lines converging on the parameters fitting the alignment, while non aligned points are mapped into non-converging lines: left-right ambiguities in Drift Tubes are naturally resolved by the method. Ghost track candidates arising from ambiguities can be filtered by means of quality requirements, *i.e.* a minimum number of votes in the parameter space, as they generally feature fewer entries in the corresponding (m,c) HT histogram bin.

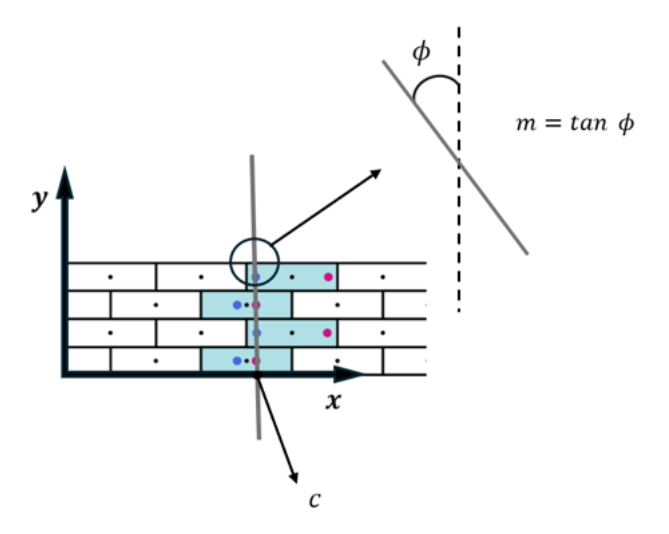


Figure 4.28: Definition of the m and c parameters for the Hough Transform-based method.  $m = \tan \phi$  where  $\phi$  is measured with respect to the normal direction to the MiniDT layers, and the intercept c is measured on a reference plane parallel to the MiniDT layers.

The HT histogram is therefore a  $n_m \times n_c$  matrix of counters mapping all the lines corresponding to transformed measured points. The square brackets [p] indicate the histogram bin size for the track parameter p. The required histogram size is driven by the range of the parameters to be detected and by the required resolution. An excessively small bin size [m, c], does not allow to find accumulations since the device resolution makes data too scattered, while a too large bin size results in a more difficult and less precise evaluation of the track parameters. In the MiniDT case, the poor amount of input data can even turn into an accumulation which goes undetected if the votes corresponding to the parameters  $\mathbf{p}^*$  are shared by neighboring bins.

## 4.4.2 MiniDTs track reconstruction steps

The Hough Transform-based method for MiniDTs is still under optimization, but its steps are roughly assessed.

This tracking method is implemented in a Python script, that takes as an input the **ROOT** file containing the TTree of MiniDT converted data, see Section 4.3. Recalling that a TTree entry corresponds to a SND@LHC event, with each of them the tracking script performs the following steps:

- MiniDT hits are assigned to "macro-cells", which group 12 tubes together, 3 adjecent tubes for each layer as in Figure 4.29. This procedure is analogous to the one used in [36]. Macro-cells are partly superimposed to each other, so that each tube is then assigned to either 1 or 2 macro-cells in odd or even layers, respectively. The macro-cell size and aspect ratio allow to limit the number of input data to a manageable number for each HT [36]. The macro-cell shape is chosen to accept track segments with angles up to φ ≈ ±70° about the ŷ direction. The partial superimposition of macro-cells ensures that any track segment with |φ| < 70° is fully contained within at least one of them. For the purpose of evaluating the size of the HT histogram in this tracking study, the slope m was limited to the [-2, 2] range, i.e. |φ| < 60°;</p>
- The HT histogram is defined as a [1000  $\times$  1000] matrix. c values are bound in a 100 cm range, while m values to the [-2, 2] range, resulting in a 1 mm and a  $\sim$  1 mrad resolution, respectively. All hits belonging to a specific macro-cell are used twice (once per laterality) to compute Equation 4.4.3, whose m, c values "vote" the corresponding bin in the histogram. If the histogram maximum is above three, i.e. it was voted by at least three different hits, its  $m_{max}$ ,  $c_{max}$  values are used to compute a temporary reconstructed track. An example of the accumulation region is shown in Figure 4.30. The hits laterality that are closer to the HT reconstructed track are the correct ones;
- Perform a linear fit on the selected MiniDT hits, whose laterality has been chosen. An example fit is shown in Figure 4.31.

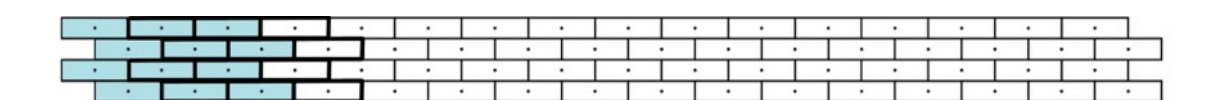


Figure 4.29: Definition of the macro-cells used to group hits together for the HT. Each macro-cell groups 12 tubes together (3 adjacent tubes per layer). The picture shows partial superimposition between consecutive macro-cells 1 (light blue) and 2 (thick contour lines).

Following what was said at the start of this paragraph, the Hough Transform-based method presented here is still under optimization, and some changes must be implemented. For instance, as was studied in [36], moving the x-axis in the local frame of

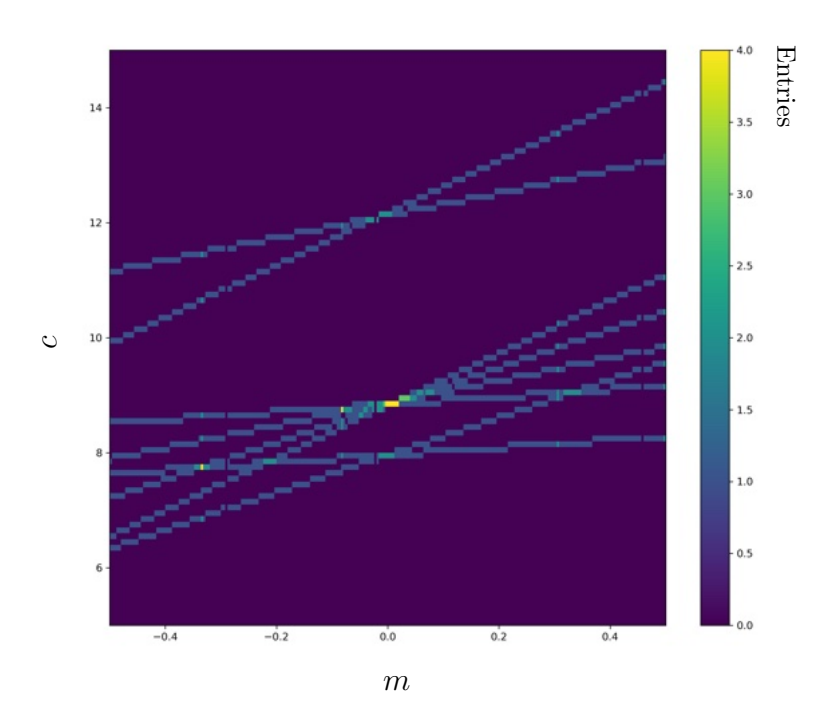


Figure 4.30: Depiction of the accumulation region in the Hough Transform histogram. The aligned hits, belonging to the real track, are mapped into lines converging on the parameters fitting the alignment, while non aligned hit are mapped into non-converging lines. The accumulation region contains the most voted bins, which correspond to the most probable m, c parameters for the MiniDT reconstructed track.

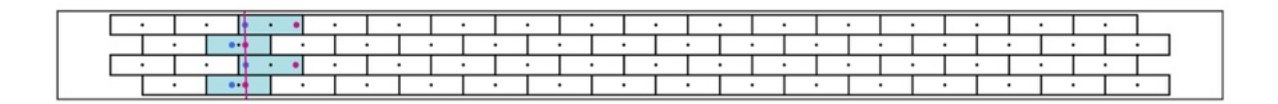


Figure 4.31: Example of a MiniDT reconstructed track, in a cross section view of the chamber. The pink line shows a linear fit performed on the selected hits, whose correct laterality was chosen with a preliminary track, computed with the m, c parameters of the HT histogram maximum.

reference from the MiniDT lower edge to the MiniDT midplane, thus making the track intercept computation more refined - this point will be in the middle of hits, which will be easier to compute than the present extrapolation to the MiniDT lower bound. Moreover, the macro-cell structure could be defined with a layout that is more symmetric about the  $\hat{y}$  direction, e.g. an alternating of two and three cells in different layers. Another change could interest the m values range itself, since  $|\phi| < 60^{\circ}$  could be a too wide

angular opening for the MiniDT tracking purposes in SND@LHC. Finally, the number of bins in the HT histogram must be optimized: the bins must be large enough to allow an efficient and well-defined accumulation region, and at the same time narrow enough to ensure the correct laterality selection for hits.

#### Conclusions and future outlook

This thesis work is focused on the the SND@LHC muon detectors upgrade with MiniDTs.

The MiniDTs detectors, small size replicas of CMS Drift Tubes, were repaired and then tested with cosmic rays before the installation, both at INFN Legnaro Laboratory and at CERN. A read out system was set up exploiting electronics for the CMS DT Phase-2 Upgrade, developed by CIEMAT (Madrid, Spain) and the INFN groups in Bologna and Padova.

All steps needed to perform the installation of the detectors, which took place in March 2025, and the operations for the detectors integration in the online and monitoring systems of SND@LHC, are described. The commissioning period, starting from the first data with cosmic rays up to the 2025 LHC data taking with colliding beams, required the development of several tools to monitor rates, data quality and efficiency. A gas leak in the MiniDT system was discovered by monitoring the quality of track segments generated by the chambers in the weeks following the installation, and it was fixed during the LHC Technical Stop 1 in June 2025.

The MiniDTs were integrated in the SND@LHC offline software, sndsw, as well. In this way, common SND@LHC-MiniDT events can be built offline, and the MiniDT data conversion to a SND@LHC-like format was implemented.

The MiniDT efficiency was measured exploiting the muon tracking based on the existing SND@LHC muon system, yielding a hit efficiency of  $\sim 97$  %, in agreement with the typical values reported by CMS DT Detector Performance Group.

A preliminary tracking method for MiniDT hits was also developed, using a Hough Transform-based algorithm, in order to provide a tool for MiniDT standalone tracks reconstruction.

The next steps will focus on the optimization of the tracking algorithm, both working on standalone tracks and to combine the information from the SND@LHC muon system and from MiniDTs, understanding in depth the alignment between the newly installed detectors and the rest of SND@LHC. It will be necessary, finally, to measure the MiniDT offline tracking performance. The final goal is to make MiniDT hits and tracks available to the whole SND@LHC collaboration for physics analysis.

### Aknowledgements

Sembra passato un secondo da quando, un anno fa, la fortuna ha voluto che capitassi in un progetto così unico, equiparabile ad un turbinio di conoscenze, insegnamenti ed esperienze sempre nuovi. Eppure, siamo già giunti ai ringraziamenti.

Innanzitutto, vorrei ringraziare il mio Relatore, Professor Luigi Guiducci, per aver creduto in un progetto così impegnativo, essere stato una grande guida, un ottimo compagno di sessioni di laboratorio (addolcite da una fetta di torta) e per essere stato sempre presente, anche da lontano, non solo con ottimi consigli, ma soprattutto con una parola di incoraggiamento e una per sdrammatizzare. Grazie per trasmettere, ogni giorno, l'entusiasmo per un lavoro che, nonostante le difficoltà, non smette mai di meravigliare.

Voglio ringraziare la Dottoressa Giulia Paggi, anche lei sostenitrice e ideatrice del progetto, per la sua disponibilità, professionalità, precisione e per la sua accoglienza nei miei mesi al CERN. In particolar modo, grazie per i pomeriggi al 40 passati a ridere, talvolta tra le lacrime, per capire come far funzionare tutto, grazie per le pause con il tè e per le rilassantissime via cordate alla CortiGrimpe, che andranno al più presto replicate.

Grazie al Dottor Gaetano Marco Dallavalle, al Dottor Federico Cindolo, al Dottor Antonio Crupano, al Professor Carlo Battilana, al Dottor Daniele Fasanella, alla Dottoressa Lisa Borgonovi e ai gruppi di SND@LHC e CMS Bologna, per il loro apporto fondamentale al progetto, e per il loro enorme sostegno. Non vedo l'ora di poter continuare a collaborare con voi.

Grazie al Dottor Franco Gonella, al Dottor Antonio Bergnoli del gruppo CMS di Padova - LNL, e al Dottor Domenico Dattola del gruppo CMS di Torino, senza i quali le MiniDT non sarebbero mai arrivate nel tunnel TI18.

Grazie al gruppo CMS di CIEMAT (Madrid), specialmente alla Dottoressa Cristina Fernandez Bedoya e al Dottor Alvaro Navarro Tobar, per il loro imprescindibile contributo all'elettronica delle MiniDT.

Grazie a tutti i membri di SND@LHC, in particolare a Simona Ilieva Ilieva, per il

grandissimo aiuto con **sndsw**, e al nostro Run Coordinator, Gerardo Vasquez, per la sua estrema disponibilità, velocità e precisione nel risolvere i nostri (non pochi) problemi.

Ringrazio Edoardo, Matilda, Lucrezia e il gruppo dei "teorici", Federico, Matteo e Damiano, per aver riempito questi due anni di magistrale di risate e pomeriggi al cinema, dopo i quali ogni esame sembrava più fattibile.

Grazie a Davide, Alessandro e a tutti coloro che si sono uniti almeno una volta alle partite di badmintom B&B sul prato del CERN. Grazie per gli splendidi e indimenticabili mesi oltralpe.

Grazie a Maria Costanza, Adele, Francesco, Federica, Samuel, Veronica e a tutta la Gang RisRistretta, per le innumerevoli avventure e gli aperitivi sin dalla triennale in pandemia, ma soprattutto per avermi fatto trovare a Bologna una nuova casa.

Grazie ad Elisa e Matilda: nessuna parola può davvero dimostrare la mia riconoscenza nei vostri confronti. Grazie per tutti i pomeriggi di studio, le serate, semplicemente tutto il tempo che posso condividere con voi, dagli anni delle temibili verifiche di matematica in classe ad ora. Aggiungo solo: l'oracolo non sbaglia (quasi) mai.

Grazie a Leonardo, per avermi insegnato che, di cinquanta metri in cinquanta metri, ogni montagna può essere scalata. E se il dislivello si fa in due, diventa tutto più leggero.

Infine, ringrazio i miei genitori e mia nonna. Senza di voi non sarei metà della persona che sono ora. Grazie per aver creduto nei miei sogni quando la motivazione veniva a mancare, e aver sopportato anche i momenti più pesanti. Forse, un giorno, farò anche da elettricista.

#### **Bibliography**

- G. Acampora et al. "SND@LHC: the scattering and neutrino detector at the LHC".
   In: Journal of Instrumentation 19.05 (May 2024), P05067. ISSN: 1748-0221. DOI: 10.1088/1748-0221/19/05/p05067.
- [2] R. Albanese et al. "Observation of Collider Muon Neutrinos with the SND@LHC Experiment". In: Phys. Rev. Lett. 131 (3 July 2023), p. 031802. DOI: 10.1103/ PhysRevLett.131.031802.
- [3] LHC Collaboration. Observation of collider neutrinos without final state muons with the SND@LHC experiment. 2024.
- [4] Giovanni De Lellis, Pasquale Migliozzi, and Pietro Santorelli. "Charm physics with neutrinos". In: *Physics Reports* 399.5 (2004), pp. 227–320. ISSN: 0370-1573. DOI: https://doi.org/10.1016/j.physrep.2004.07.005.
- [5] Tanju Gleisberg et al. "SHERPA 1., a proof-of-concept version". In: Journal of High Energy Physics 2004.02 (Mar. 2004), p. 056. DOI: 10.1088/1126-6708/ 2004/02/056.
- [6] Alexey Boyarsky et al. "Searches for new physics at SND@LHC". In: Journal of High Energy Physics 2022.3 (Mar. 2022). ISSN: 1029-8479. DOI: 10.1007/ jhep03(2022)006.
- [7] Maximilien Brice. "Photos of the new detector of SND@LHC Experiment". In: (2022). General Photo.
- [8] N Beni et al. "Physics potential of an experiment using LHC neutrinos". In: Journal of Physics G: Nuclear and Particle Physics 46.11 (Oct. 2019), p. 115008. DOI: 10.1088/1361-6471/ab3f7c.
- [9] D. Abbaneo et al. "Installation and performance of the 3rd Veto plane at the SND@LHC detector". In: Journal of Instrumentation 20.07 (July 2025), P07011. DOI: 10.1088/1748-0221/20/07/P07011.

- [10] S. et al. Baron. The TTC Website.
- [11] The SND@LHC Collaboration. sndsw. https://github.com/SND-LHC/sndsw.
- [12] M Al-Turany et al. "The FairRoot framework". In: Journal of Physics: Conference Series 396.2 (Dec. 2012), p. 022001. DOI: 10.1088/1742-6596/396/2/022001.
- [13] LHC Collaboration. Measurement of the muon flux at the SND@LHC experiment. 2023.
- [14] Ettore Zaffaroni. Results from SND@LHC. Tech. rep. 2023.
- [15] S. Chatrchyan et al. "The CMS Experiment at the CERN LHC". In: *JINST* 3 (2008), S08004. DOI: 10.1088/1748-0221/3/08/S08004.
- [16] J. G. Layter. *The CMS muon project*. Technical design report. CMS. Geneva: CERN, 1997.
- [17] Giulia Paggi. "Construction and test of a cosmic ray telescope based on CMS Drift Tube chambers and data acquisition prototypes of the Phase-2 upgrade". MA thesis.
- [18] C. F. Bedoya et al. "OBDT-theta, a multi-channel TDC and readout board for the CMS muon drift tubes in HL-LHC". In: Frontiers in Detector Science and Technology Volume 3 - 2025 (2025). ISSN: 2813-8031. DOI: 10.3389/fdest.2025. 1517241.
- [19] I. Redondo and on behalf of the CMS collaboration. "Upgrade of the CMS Drift Tube electronics for the High Luminosity LHC". In: *Journal of Instrumentation* 20.01 (Jan. 2025), p. C01011. DOI: 10.1088/1748-0221/20/01/C01011.
- [20] N. Guettouche et al. "The lpGBT production testing system". In: Journal of Instrumentation 17.03 (Mar. 2022), p. C03040. DOI: 10.1088/1748-0221/17/03/C03040.
- [21] Versatile Link+ Technical Specification: Versatile Link+ Transceiver (VTRx+).
- [22] Jeroen Hegeman et al. "The CMS Timing and Control Distribution System". In: 2015 IEEE Nuclear Science Symposium and Medical Imaging Conference (NSS/MIC). 2015, pp. 1–3. DOI: 10.1109/NSSMIC.2015.7581984.
- [23] VCU118 Evaluation Board: User Guide.
- [24] AMD Virtex UltraScale+ FPGA.

- [25] BeagleBone Black: System Reference Manual.
- [26] Digilent JTAG HS3 Reference Manual.
- [27] G. et al. Goavec-Merou. openFPGALoader: Universal utility for programming FP-GAs.
- [28] Ernest Murer Paulo Moreira. TTCrx and QPLL Mezzanine Card (TTCrq).
- [29] A. Marchioro J. Christiansen and P. Moreira. TTCrx, AN ASIC FOR TIMING, TRIGGER AND CONTROL DISTRIBUTION IN LHC EXPERIMENTS.
- [30] Eduardo Mendes. HPTC: High-Precision Timing Clock.
- [31] G. Abbiendi et al. "The Analytical Method algorithm for trigger primitives generation at the LHC Drift Tubes detector". In: Nuclear Instruments and Methods in Physics Research Section A: Accelerators, Spectrometers, Detectors and Associated Equipment 1049 (2023), p. 168103. ISSN: 0168-9002. DOI: https://doi.org/10.1016/j.nima.2023.168103.
- [32] B G Taylor. "Timing distribution at the LHC". In: (2002). DOI: 10.5170/CERN-2002-003.63.
- [33] *Grafana*. https://grafana.com/.
- [34] G. Aad et al. "Luminosity determination in pp collisions at  $\sqrt{s} = 13$  TeV using the ATLAS detector at the LHC". In: The European Physical Journal C 83.10 (Oct. 2023). ISSN: 1434-6052. DOI: 10.1140/epjc/s10052-023-11747-w.
- [35] CMS Collaboration. "Monitoring of CMS Drift Tube efficiency trends". In: (2024).
- [36] Nicola Pozzobon, Fabio Montecassiano, and Pierluigi Zotto. "A novel approach to Hough Transform for implementation in fast triggers". In: *Nuclear Instruments and Methods in Physics Research Section A: Accelerators, Spectrometers, Detectors and Associated Equipment* 834 (2016), pp. 81–97. ISSN: 0168-9002. DOI: https://doi.org/10.1016/j.nima.2016.07.020.
- [37] P V.C. Hough. METHOD AND MEANS FOR RECOGNIZING COMPLEX PAT-TERNS. US Patent. Dec. 1962.
- [38] J. Illingworth and J. Kittler. "A survey of the hough transform". In: Computer Vision, Graphics, and Image Processing 44.1 (1988), pp. 87–116. ISSN: 0734-189X. DOI: https://doi.org/10.1016/S0734-189X(88)80033-1.

[39] Richard O. Duda and Peter E. Hart. "Use of the Hough transformation to detect lines and curves in pictures". In: *Commun. ACM* 15.1 (Jan. 1972), pp. 11–15. ISSN: 0001-0782. DOI: 10.1145/361237.361242.

# A | MiniDTs LV and HV connections in TI18



Figure A.1: The SND@LHC CAEN mainframe with the MiniDT HV power booster.



**Figure A.2:** The MiniDT power booster, with the CAEN A7030DN module for the cathodes (-1200 V) and a CAEN A1833P for the strips and anodes (+1800 V, +3600 V) respectively) and the corresponding HV cables.

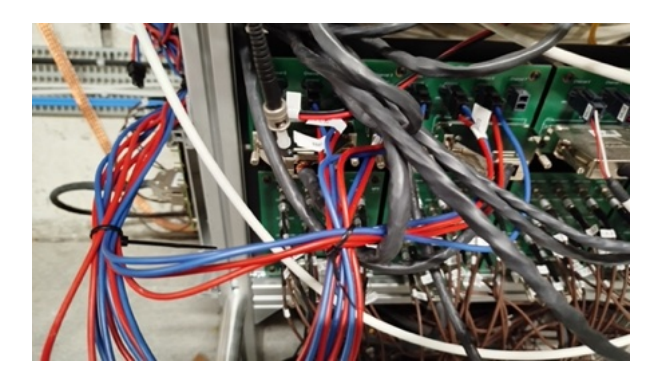
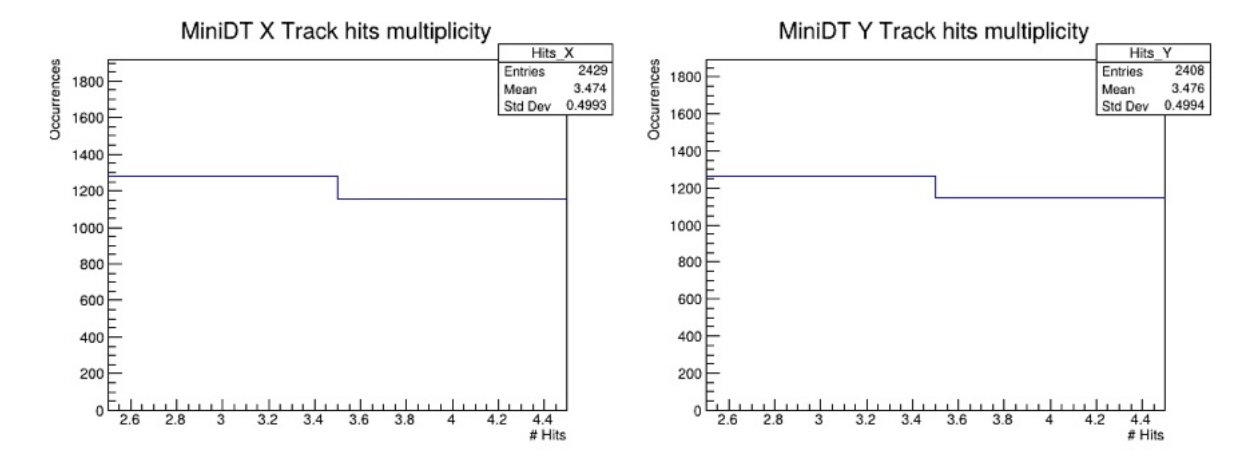


Figure A.3: The MiniDT LV patch panel.

## B | MiniDTs preliminary studies on tracking with cosmic rays

The following plots refer to the tracking performed with MiniDT hits from cosmic rays, presented in Section 4.1.3. The hits coordinates are computed in a local frame of reference, whose origin is in the chamber's lower left angle. The tracks are fitted with the  $y = [p_0] + [p_1]x$  linear function, where  $[p_0]$  is the track intercept at x = 0 and  $[p_1]$  is the track slope. In the following plots, "XIntercept" refers to the track horizontal intercept, between the 2nd and the 3rd layers of the MiniDT.



**Figure B.1:** The distribution of the number of hits in MiniDT reconstructed tracks, whose amount can be either 3 or 4.

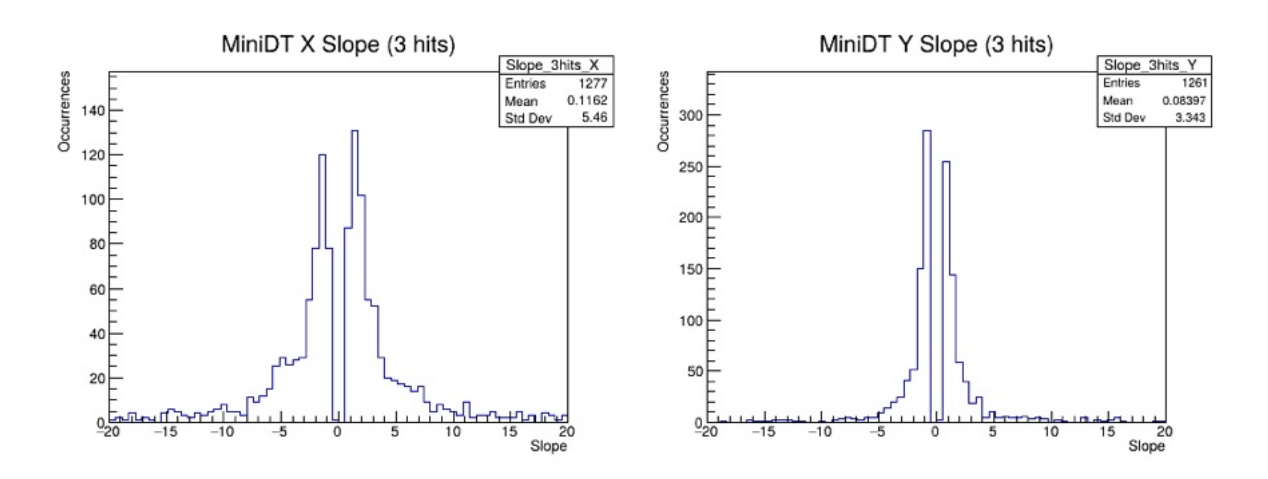


Figure B.2: Distribution of track slopes in MiniDT reconstructed 3-hits only tracks.

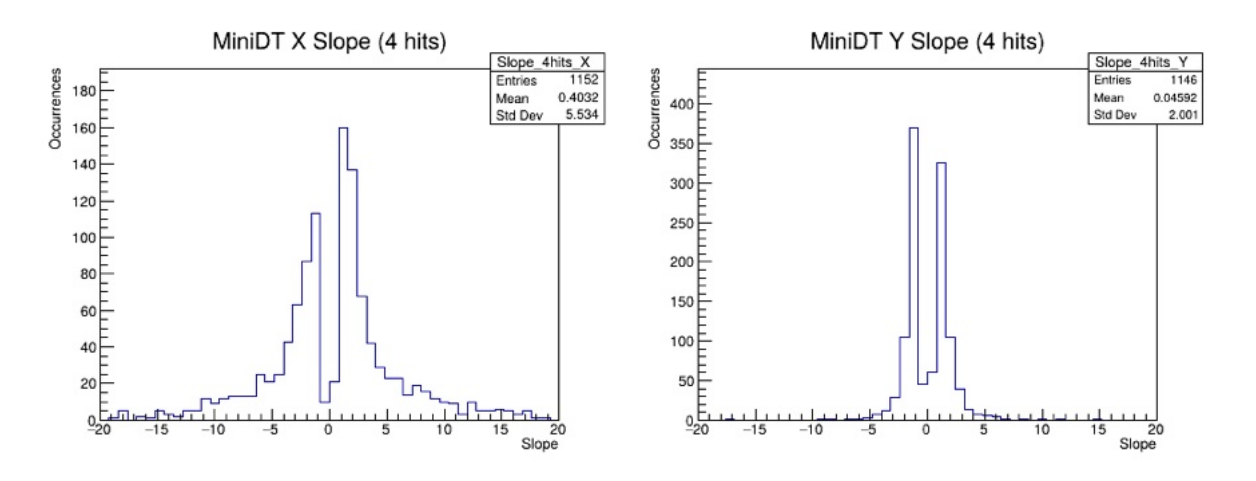


Figure B.3: Distribution of track slopes in MiniDT reconstructed 4-hits only tracks.

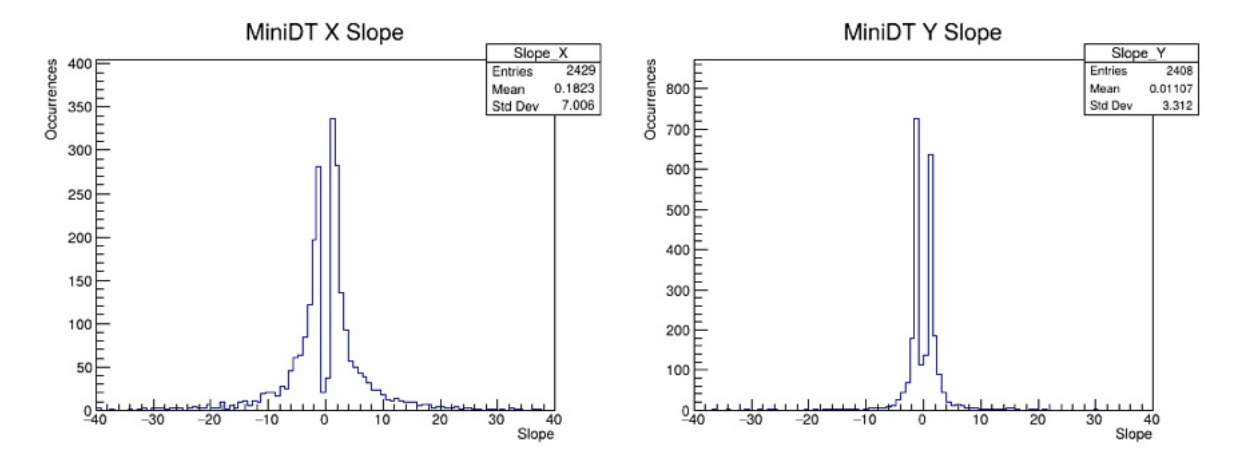
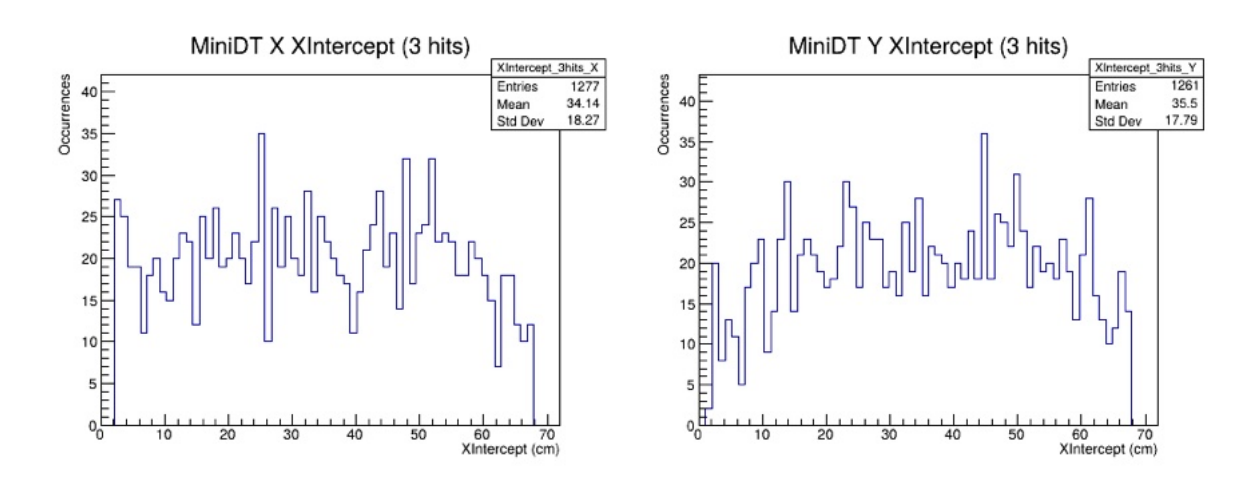
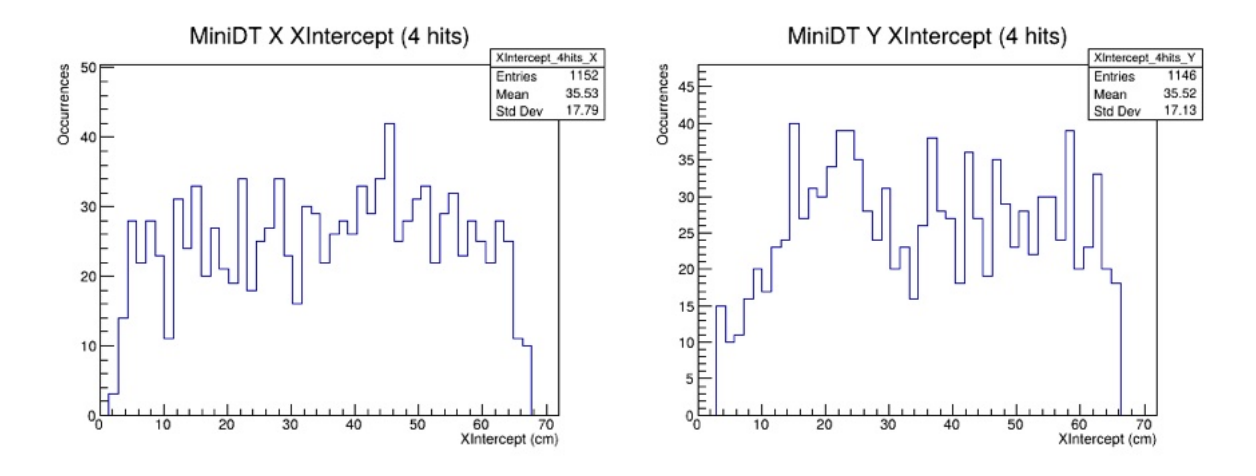


Figure B.4: Distribution of track slopes in all MiniDT reconstructed tracks.



**Figure B.5:** Distribution of track horizontal intercepts in MiniDT reconstructed 3-hits only tracks.



**Figure B.6:** Distribution of track horizontal intercepts in MiniDT reconstructed 4-hits only tracks.

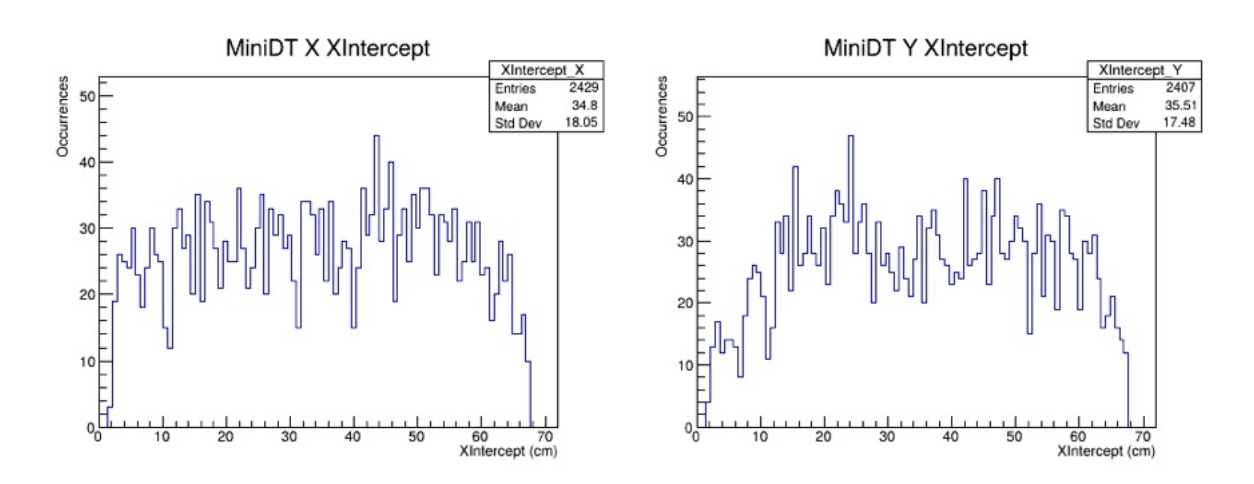


**Figure B.7:** Distribution of track horizontal intercepts in all MiniDT reconstructed tracks.

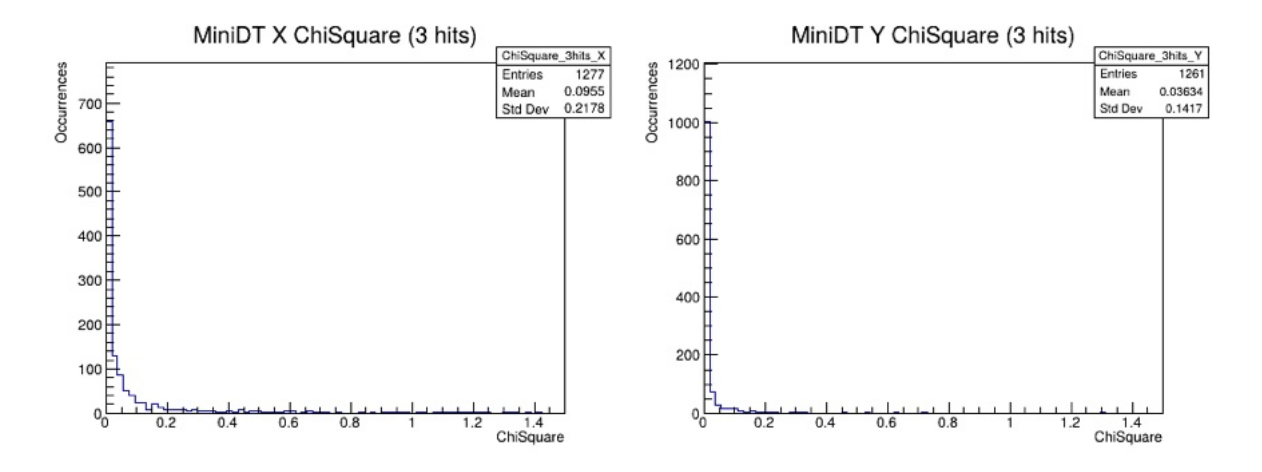


**Figure B.8:** Distribution of track Chi-Square in MiniDT reconstructed 3-hits only tracks.

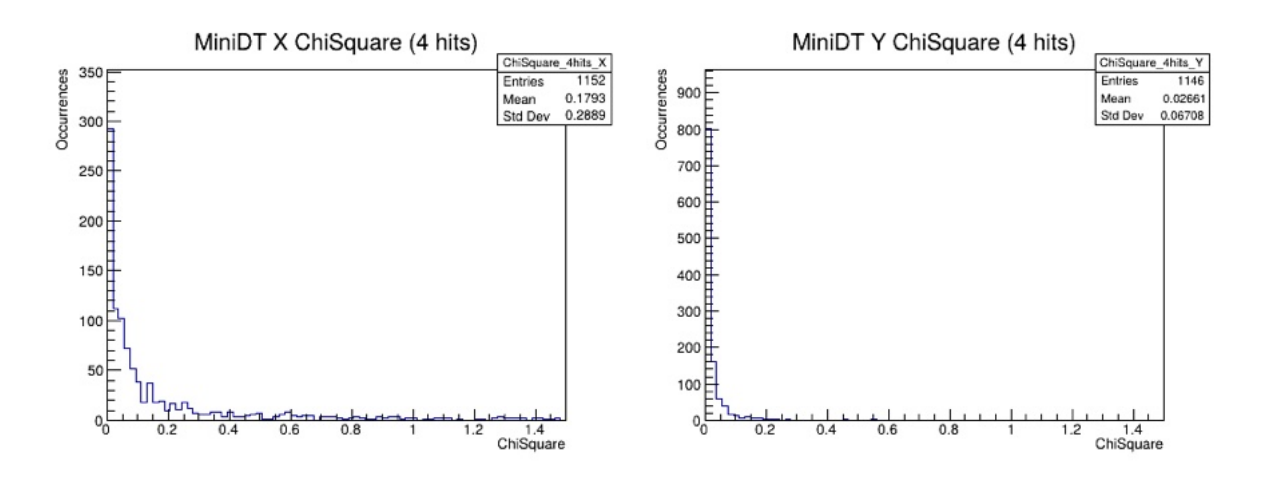


**Figure B.9:** Distribution of track Chi-Square in MiniDT reconstructed 4-hits only tracks.

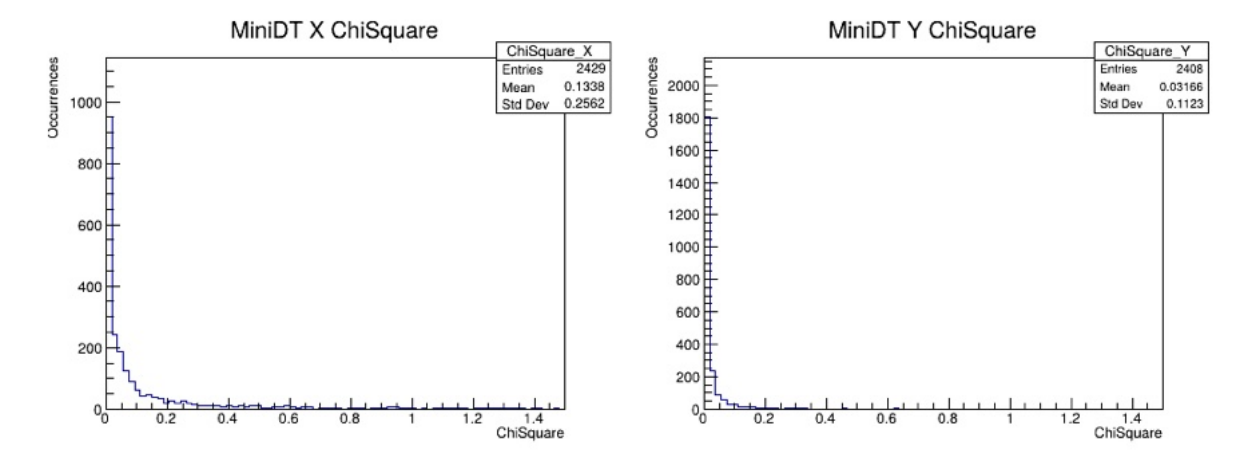


Figure B.10: Distribution of track Chi-Square in all MiniDT reconstructed tracks.